

AD-A116 692

AIR FORCE INST OF TECH WRIGHT-PATTERSON AFB OH
A THREE DIMENSIONAL MODEL OF THE PLASMA FLOW AND MAGNETIC FIELD--ETC(U)
MAR 82 T F TASCIONE
AFIT/NR/82-160

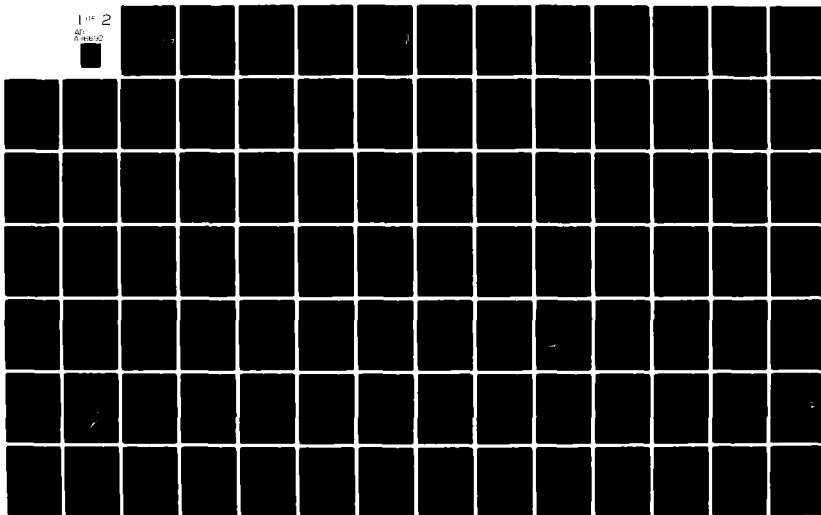
F/G 20/9

UNCLASSIFIED

NL

1 OF 2

AD
PENDING



AD A116692

DTIC FILE COPY

UNCLASS
SECURITY CLASSIFICATION OF THIS PAGE (When Data Entered)

①

REPORT DOCUMENTATION PAGE		READ INSTRUCTIONS BEFORE COMPLETING FORM
1. REPORT NUMBER AFIT/NR/82-16D	2. GOVT ACCESSION NO. AD-A116692	3. RECIPIENT'S CATALOG NUMBER 692
4. TITLE (and Subtitle) A Three Dimensional Model of the Plasma Flow and Magnetic Fields in the Dayside Ionosphere of Venus		5. TYPE OF REPORT & PERIOD COVERED THESIS/DISSERTATION
7. AUTHOR(s) Thomas F. Tascione		6. PERFORMING ORG. REPORT NUMBER
9. PERFORMING ORGANIZATION NAME AND ADDRESS AFIT STUDENT AT: Rice University		8. CONTRACT OR GRANT NUMBER(s)
11. CONTROLLING OFFICE NAME AND ADDRESS AFIT/NR WPAFB OH 45433		10. PROGRAM ELEMENT, PROJECT, TASK AREA & WORK UNIT NUMBERS
12. REPORT DATE March 1982		13. NUMBER OF PAGES 162
14. MONITORING AGENCY NAME & ADDRESS (if different from Controlling Office)		15. SECURITY CLASS. (of this report) UNCLASS
16. DISTRIBUTION STATEMENT (of this Report) APPROVED FOR PUBLIC RELEASE; DISTRIBUTION UNLIMITED		15a. DECLASSIFICATION/DOWNGRADING SCHEDULE
17. DISTRIBUTION STATEMENT (of the abstract entered in Block 20, if different from Report)		
18. SUPPLEMENTARY NOTES APPROVED FOR PUBLIC RELEASE: IAW AFR 190-17 22 JUN 1982 LYNN E. WOLAVER Dean for Research and Professional Development AFIT, Wright-Patterson AFB OH		
19. KEY WORDS (Continue on reverse side if necessary and identify by block number)		
20. ABSTRACT (Continue on reverse side if necessary and identify by block number) ATTACHED		

DTIC
ELECTE
JUL 9 1982
S H D

DD FORM 1473 1 JAN 73 EDITION OF 1 NOV 65 IS OBSOLETE

UNCLASS

SECURITY CLASSIFICATION OF THIS PAGE (When Data Entered)

82 07 07 051

ABSTRACT

A THREE DIMENSIONAL MODEL OF THE PLASMA FLOW AND MAGNETIC FIELDS IN THE DAYSIDE IONOSPHERE OF VENUS

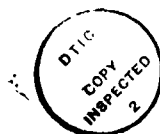
by

Thomas F. Tascione

Today, the earth's intrinsic magnetic field prevents the streaming solar wind plasma from directly interacting with the terrestrial atmosphere. Periodically the geomagnetic field reverses direction, and during the transition period, the earth's magnetic barrier is thought to disappear. In the past, studies about the atmospheric-solar wind interaction dynamics were hindered by a scarcity of observational data. However, since December 1978, the Pioneer-Venus Orbiter has been providing daily observations of the atmospheric dynamics produced by the direct solar wind interaction with the atmosphere of Venus (the only planet known to lack an intrinsic magnetic field). This thesis develops the first three dimensional magnetohydrodynamic (MHD) theory of this interaction.

Within the ionosphere of Venus analytic solutions to the MHD equations are possible because of a favorable geometry between the induced ionospheric magnetic fields and

the ionospheric plasma motions. It is shown that variations in the solar wind speed and interplanetary magnetic vector direction cause variations in the dayside ionospheric plasma flows and the induced magnetic field configuration, and that these changes can account for the variety of magnetic structures observed by Pioneer-Venus. Portions of the Venus ionosphere are shown to be susceptible to the Kelvin-Helmholtz shear instability. The unusual shape of the computed region of stability is shown to be an important key to understanding the highly variable Pioneer-Venus observations. Model calculations are compared to observations for a number of selected orbits, and the model is shown to match the observations in fine detail.



Accession For	
NTIS GRA&I	<input checked="checked" type="checkbox"/>
DTIC TAB	<input type="checkbox"/>
Unannounced	<input type="checkbox"/>
Justification	
By	
Distribution/	
Availability Codes	
Avail and/or	
Dist	
A	

AFIT RESEARCH ASSESSMENT

The purpose of this questionnaire is to ascertain the value and/or contribution of research accomplished by students or faculty of the Air Force Institute of Technology (AFIT). It would be greatly appreciated if you would complete the following questionnaire and return it to:

AFIT/NR
Wright-Patterson AFB OH 45433

RESEARCH TITLE: A Three Dimensional Model of the Plasma Flow and Magnetic Fields in the Dayside Ionosphere of Venus

AUTHOR: Thomas F. Tascione

RESEARCH ASSESSMENT QUESTIONS:

1. Did this research contribute to a current Air Force project?
☐ a. YES ☐ b. NO
2. Do you believe this research topic is significant enough that it would have been researched (or contracted) by your organization or another agency if AFIT had not?
☐ a. YES ☐ b. NO
3. The benefits of AFIT research can often be expressed by the equivalent value that your agency achieved/received by virtue of AFIT performing the research. Can you estimate what this research would have cost if it had been accomplished under contract or if it had been done in-house in terms of manpower and/or dollars?
☐ a. MAN-YEARS ☐ b. \$
4. Often it is not possible to attach equivalent dollar values to research, although the results of the research may, in fact, be important. Whether or not you were able to establish an equivalent value for this research (3. above), what is your estimate of its significance?
☐ a. HIGHLY SIGNIFICANT ☐ b. SIGNIFICANT ☐ c. SLIGHTLY SIGNIFICANT ☐ d. OF NO SIGNIFICANCE
5. AFIT welcomes any further comments you may have on the above questions, or any additional details concerning the current application, future potential, or other value of this research. Please use the bottom part of this questionnaire for your statement(s).

NAME	GRADE	POSITION
ORGANIZATION	LOCATION	

STATEMENT(s):

FOLD DOWN ON OUTSIDE - SEAL WITH TAPE

AFIT/NR
WRIGHT-PATTERSON AFB OH 45433
OFFICIAL BUSINESS
PENALTY FOR PRIVATE USE. \$300



NO POSTAGE
NECESSARY
IF MAILED
IN THE
UNITED STATES

BUSINESS REPLY MAIL

FIRST CLASS PERMIT NO. 73236 WASHINGTON D.C.

POSTAGE WILL BE PAID BY ADDRESSEE

AFIT/ DAA

Wright-Patterson AFB OH 45433



FOLD IN

RICE UNIVERSITY

A THREE DIMENSIONAL MODEL OF THE PLASMA FLOW
AND MAGNETIC FIELDS IN THE DAYSIDE
IONOSPHERE OF VENUS

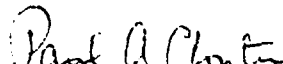
by


THOMAS F. TASCIONE


A THESIS SUBMITTED
IN PARTIAL FULFILLMENT OF THE
REQUIREMENTS FOR THE DEGREE

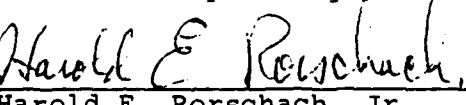
DOCTOR OF PHILOSOPHY

APPROVED, THESIS COMMITTEE:


Paul A. Cloutier, Professor
Space Physics and Astronomy


Robert C. Haymes, Professor
Space Physics and Astronomy


Patricia H. Reiff
Associate Research Scientist
Center for Space Physics


Harold E. Rorschach, Jr.
Professor of Physics

HOUSTON, TEXAS

March, 1982

ABSTRACT

A THREE DIMENSIONAL MODEL OF THE PLASMA FLOW AND MAGNETIC FIELDS IN THE DAYSIDE IONOSPHERE OF VENUS

by

Thomas F. Tascione

Today, the earth's intrinsic magnetic field prevents the streaming solar wind plasma from directly interacting with the terrestrial atmosphere. Periodically the geomagnetic field reverses direction, and during the transition period, the earth's magnetic barrier is thought to disappear. In the past, studies about the atmospheric-solar wind interaction dynamics were hindered by a scarcity of observational data. However, since December 1978, the Pioneer-Venus Orbiter has been providing daily observations of the atmospheric dynamics produced by the direct solar wind interaction with the atmosphere of Venus (the only planet known to lack an intrinsic magnetic field). This thesis develops the first three dimensional magnetohydrodynamic (MHD) theory of this interaction.

Within the ionosphere of Venus analytic solutions to the MHD equations are possible because of a favorable geometry between the induced ionospheric magnetic fields and

the ionospheric plasma motions. It is shown that variations in the solar wind speed and interplanetary magnetic vector direction cause variations in the dayside ionospheric plasma flows and the induced magnetic field configuration, and that these changes can account for the variety of magnetic structures observed by Pioneer-Venus. Portions of the Venus ionosphere are shown to be susceptible to the Kelvin-Helmholtz shear instability. The unusual shape of the computed region of stability is shown to be an important key to understanding the highly variable Pioneer-Venus observations. Model calculations are compared to observations for a number of selected orbits, and the model is shown to match the observations in fine detail.

ACKNOWLEDGMENTS

I would like to thank my thesis director, Dr. Paul A. Cloutier, for proposing this topic and for his astute suggestions during the course of this research. Under his guidance, I have gained insights into physics which not only helped me in this project but will continue to help me in the years to come. I'm indebted to G.-H. Voigt for allowing me to use his magnetic field line tracing program. I would also like to thank Drs. R. A. Wolf and R. E. Daniell for many useful discussions and comments, and to Drs. R. C. Haymes, P. H. Reiff, and H. E. Rorscharch for serving on my committee. In addition, I want to thank H. A. Taylor for providing the Pioneer-Venus ion data and C. T. Russell for supplying the Pioneer-Venus magnetometer data. A special thanks to Air Weather Service for giving me the opportunity to complete this research. Finally, I wish to thank my wife and children for their support, encouragement and understanding during this project.

This research was supported by NASA contract NAS 5-23338.

TABLE OF CONTENTS

ii

Acknowledgments	i
Table of contents	ii
List of Figures	iv
1. Introduction	1
2. Model Theory	
2.1. Horizontal MHD Equations	7
2.2. Plasma Flow Asymmetry	12
2.3. Magnetic Field Equations	20
2.4. Magnetic Field Asymmetry	27
2.5. Instability Criterion	35
2.6. Summary	42
3. Numerical Model	
3.1. Model Components	45
3.2. Model Application-General Characteristics	53
3.3. Analysis of Orbit 170	61
3.4. Analysis of Orbit 176	70
3.5. Analysis of Orbit 177	77
3.6. Analysis of Orbit 188	84
3.7. Analysis of Orbit 189	92
3.8. Analysis of Orbit 175	100
4. Discussion	
4.1. Comparison of Orbits	114
4.2. Comparison with the 2-D Electrodynamic Model	117
4.3. Problem Areas	123
5. Conclusion	124

Appendix: Analytic Equations for the Three
Dimensional Flow/Field Model.

A.1. Magnetic Field Equations	126
A.2. Determination of Constants	137
A.3. Contours of Constant Magnetic Field Strength	148
References	152

LIST OF FIGURES

iv

Figure	Title	Page
2-1	Coordinate system	11
2-2	Velocity profiles	16
2-3	Magnetic prime meridian current system	32
2-4	Flux-rope schematic	37
3-1	Model regions and radial flow- lines	46
3-2	Distortion of the IMF resulting from interaction with the plan- etary ionosphere	47
3-3	Ionosphere and ionosheath flow- lines	50
3-4	Idealized stable region	55
3-5	Orbit 170 - horizontal projection of the magnetic field parameters	63
3-6	Orbit 170 - orbital plane cross- section	65
3-7	Orbit 170 - comparison of model with observations	67
3-8	Orbit 176 - horizontal projection of the magnetic field parameters	71
3-9	Orbit 176 - orbital plane cross- section	73

3-10	Orbit 176 - comparison of model with observations	75
3-11	Orbit 177 - horizontal projection of the magnetic field parameters	78
3-12	Orbit 177 - orbital plane cross- section	80
3-13	Orbit 177 - comparison of model with observations	82
3-14	Orbit 188 - horizontal projection of the magnetic field parameters	86
3-15	Orbit 188 - orbital plane cross- section	88
3-16	Orbit 188 - comparison of model with observations	90
3-17	Orbit 189 - horizontal projection of the magnetic field parameters	94
3-18	Orbit 189 - orbital plane cross- section	96
3-19	Orbit 189 - comparison of model with observations	98
3-20	Orbit 175 - horizontal projection of the magnetic parameters	104
3-21	Orbit 175/2 - horizontal projection	106
3-22	Orbit 175/3 - horizontal projection	108
3-23	Orbit 175 - orbital plane cross- section	110

3-24	Orbit 175 - comparison of model with observations	112
4-1	Comparison of horizontal magnetic field strength contours	119
4-2	Comparison of Pioneer Venus observations with the two dimensional electrodynamic model	121
A-1	Surface coordinates for field line geo- metry calculations	140
A-2	Cross-section near the magnetic equator showing the relation between the sur- face variables and the projection plane variables.	141

1. INTRODUCTION.

Today, the earth's intrinsic magnetic field prevents the streaming solar wind plasma from directly interacting with terrestrial atmosphere. Fossilized rocks show that the geomagnetic field reverses direction at intervals as short as 50,000 years (Haymes, 1971). During the field transition period, the geomagnetic field is thought to weaken enough to allow the solar wind to directly interact with the atmosphere. In the past, studies about the nature of this interaction were hindered by the lack of observational data. However, evidence of such an interaction is presently available on Venus, the earth's sister planet. Venus is the only planet whose ionosphere is known to directly interact with the solar wind. Since December 1978, the PIONEER VENUS ORBITER (PV) has been providing the most comprehensive set of observations ever obtained of an extraterrestrial planetary ionosphere-atmosphere system. Once every 24 hours, the orbiter collects data within the solar wind interaction region; the highly inclined orbit (105°) requires about 243 days to precess through all local times (Colin, 1979). The purpose of this thesis is to develop a three dimensional model of the ionospheric dynamics resulting from this solar wind/Venus ionosphere interaction.

Since Venus lacks an intrinsic magnetic field (Russell et al., 1980b), the ionosphere deflects the incident solar wind by thermal pressure and by magnetic pressure produced

by ionospheric currents. In an earlier series of papers (Cloutier et al., 1969; Michel, 1971; Cloutier and Daniell, 1973; Cloutier et al., 1974; Cloutier, 1976) it was shown that a planetary atmosphere that is optically thick at ionizing wavelengths should deflect most of the solar wind plasma around the ionosphere forming a detached bow shock. The planetary atmosphere acts as a hard obstacle absorbing, at most, a few percent of the incident solar wind flux (Daniell and Cloutier, 1977; Cloutier and Daniell, 1979). PV observations have confirmed these theoretical predictions.

Observations reported by Wolfe et al. (1979) and Mihalov et al. (1980) confirm the existence of a strong detached bow shock. The average nose radius for the bow shock is about $1.38 - 1.46 R_V$ (radius of Venus) with frequent daily variations in excess of $.16 R_V$ (Slavin et al., 1980; Theis et al., 1981). However, Smirnov et al. (1980) report a nose radius of $1.27 R_V$. There are two reasons for the reported range in bow shock locations. First, most shock crossings are observed at large solar zenith angles (SZA), which makes extrapolation to the nose value difficult. Second, different procedures were used to find average bow shock shapes which best fit the PV observations (Smirnov et al., 1980). The large daily variation of the bow shock is consistent with the theory that only a few percent of the solar wind flux is absorbed (Gombosi et al.,

1980 and Mihalov et al., 1980). On the downstream side of the bowshock is the ionosheath region where the shocked solar wind plasma is diverted around the ionosphere of Venus. In the ionosheath region, the magnetic field drapes around the planet and the peak magnetic field strength occurs in a region where the flow stagnates (Elphic et al., 1980; Vaisberg et al., 1980). In the stagnation region the plasma density is low because of plasma losses along the magnetic field lines (Zwan and Wolf, 1976).

The boundary between the hot, tenuous ionosheath plasma and the cool, dense ionospheric plasma is called the ionopause. Generally, the dayside ionopause is easily identified by a relatively abrupt cutoff of the thermal ions (Taylor et al., 1979a). However, the ionopause altitude exhibits large daily variations; the ionopause height is usually confined below 400 km near the subsolar point and can extend beyond 1000 km near the terminator (Taylor et al., 1979b, 1980, 1981). The ionopause boundary occurs at the altitude where the ionospheric thermal pressure approximately balances the magnetic pressure just outside the ionopause. Since the magnetic pressure just above the ionopause is approximately equal to the solar wind dynamic pressure, the ionopause height variability is a consequence of the variability of the solar wind ram pressure (Brace et al., 1979a, 1980; Knudsen et al., 1979a; Taylor et al., 1979; Elphic et al., 1980; Spenner et al., 1980).

In the two dimensional ionospheric model of Cloutier and Daniell (Daniell and Cloutier, 1977; Cloutier and Daniell 1979), the solar wind interaction drives rapid horizontal convection within the ionosphere of Venus. The convection is driven by pressure gradients and electric fields induced in the ionosphere by the flowing magnetized solar wind plasma; these electric fields produce electric currents within the ionosphere which connect across the ionopause into the ionosheath region. The average volume distribution of ionospheric currents was determined by minimizing the volume Joule heating by a variational technique. This model was recently modified to include the effects: a) plasma depletion at the stagnation point, b) development of Kelvin-Helmholtz shear type instabilities, and c) variations in the solar wind dynamic pressure and the interplanetary magnetic field (Cloutier et al., 1981). This revised model matched PV magnetic field strength observations very well near the prime meridian plane and showed that the observed bundles of twisted magnetic fields or "flux ropes" (Russell et al., 1979a, 1979b; Elphic et al., 1980) were produced by the Kelvin-Helmholtz velocity shear instability. The model also showed that changes in the interplanetary magnetic field (IMF) orientation and the solar wind dynamic pressure could have dramatic effects on the ionospheric current distribution which explained the daily variability in the PV magnetometer measurements. However, this model was still

two dimensional and had limited applicability at longitudes far from the noon meridian. Furthermore, the model could not match the full PV magnetic vector observations in detail. Therefore, the next logical step was to develop a three dimensional model of the dayside ionospheric dynamics of Venus.

The most straightforward three dimensional model is one which solves the complete set of vector magnetohydrodynamic (MHD) equations. In practice it is very difficult to solve these formidable coupled second order differential equations in all but the simplest geometry. In fact, such a method is impossible for Venus because very few of the necessary boundary conditions are known. Similarly, this lack of known boundary conditions makes a three-dimensional variational method impractical since there is no way to determine the electric field variation with longitude without first solving the MHD equations. Fortunately, two pieces of observational information help simplify the problem enough so that analytic solutions for the dayside ionospheric magnetic fields can be found. The key observations are that both the magnetic fields (Luhmann et al., 1980, 1981a) and plasma flow (Knudsen et al., 1980, 1981) are nearly horizontal at large solar zenith angles. It will be shown that if both the flow and fields are horizontal (but not necessarily parallel to each other), the MHD equations simplify and decouple, and can be solved in a straightforward manner. It

will also be shown that the plasma depletion mechanism operating about the stagnation point introduces an asymmetry in the flow geometry, and that this asymmetry is carried into the ionosphere. Since the ionospheric conductivity is relatively high, the ionospheric magnetic fields are coupled with the plasma flow and therefore, an asymmetry also exists in the magnetic field geometry. The above theory is developed for the dayside ionosphere of Venus in Chapter 2; in Chapter 3, the horizontal flow/field model calculations are compared to PV observations. The thesis concludes with a discussion of the model and areas of possible model improvements.

2. MODEL THEORY

2.1 Horizontal MHD Equations

The general equations describing the steady-state, three-dimensional dynamics of the Venus ionosphere are:

$$\nabla \cdot \rho \chi = Q - L \quad (2.1.1)$$

$$\rho \chi \cdot \nabla \chi = -\nabla P + \rho g + J \times B \quad (2.1.2)$$

plus Maxwell's equations

$$\nabla \cdot E = \rho_c / \epsilon_0 \quad (2.1.3a)$$

$$\nabla \cdot B = 0 \quad (2.1.3b)$$

$$\nabla \times E = 0 \quad (2.1.3c)$$

$$\nabla \times B = \mu_0 J \quad (2.1.3d)$$

where Q and L are the ion production and loss rates respectively; ρ_c is the free charge density; ρ is the plasma mass density; χ is the plasma flow velocity; E , B and J are the electric field, magnetic field and current density; P is the thermal plasma pressure; g is the acceleration of gravity; and ϵ_0 and μ_0 are the dielectric constant and magnetic permeability of free space. The angle between χ and B can

be expressed as

$$\theta = \cos^{-1} \left(\frac{\vec{y} \cdot \vec{B}}{|\vec{y}| |\vec{B}|} \right) \quad (2.1.4)$$

The following analysis implicitly assumes a tangential interplanetary magnetic field (IMF).

The inertial coordinate system is shown in Figure 2-1. The Z axis is always aligned into the direction of the solar wind (anti-solar wind), the Y axis is aligned parallel to the IMF direction and, therefore, the X axis is always perpendicular to the IMF direction. The coordinate system origin is at the center of Venus. In terms of spherical geometry, m is the polar angle and ψ is the azimuthal angle. As seen in Figure 2-1, surface distances are measured in terms of angular displacements of m and ψ ; also shown are the surface unit vectors. The plasma flow streamlines are lines parallel to \hat{m} . That is, the model assumes that the plasma flows radially (parallel to surface) away from the plasma flow origin.

The assumption that the flow lines radiate from the sub-flow origin is based upon the bulk ion flow observations of Knudsen et al. (1980). They report that, with few exceptions, the flow is parallel to the antisolar direction and generally increases in magnitude with altitude. These observations covered a period of nearly two years. It will be shown that due to the high ionospheric conductivities,

the fields are closely coupled with the plasma flow and therefore, the coordinate system (tied to field) shown in Figure 2-1 rotates with changes of the IMF orientation. Over a two year period, the IMF varies regularly between being oriented parallel to the ecliptic plane to being perpendicular to this plane. Since the orbit is fixed relative to the ecliptic plane, these IMF orientation changes mean that the Pioneer-Venus Orbiter has probably taken measurements at every azimuthal angle, ψ . Therefore, the assumption of radial flowlines at all ψ (strictly antisolar) is a very good first approximation.

In terms of these curvilinear surface coordinates, the horizontal velocity and magnetic fields are

$$\underline{v} (r, m, \psi) = v (r, m, \psi) \hat{m} \quad (2.1.5)$$

$$\underline{B} (r, m, \psi) = B_m(r, m, \psi) \hat{m} + B_\psi (r, m, \psi) \hat{\psi} \quad (2.1.6)$$

where both \underline{v} and \underline{B} are functions of height (r) and position (m, ψ). The horizontal plasma acceleration can be written (Oates, 1974) as

$$\underline{v} \cdot \nabla \underline{v} = \frac{v}{r} \frac{\partial v}{\partial m} \hat{m} - \frac{v^2}{r} \hat{r} \quad (2.1.7)$$

Substituting (2.1.5) into (2.1.1), the continuity equation becomes

$$\frac{\rho}{r} \frac{\partial v}{\partial m} + \frac{v}{r} \frac{\partial \rho}{\partial m} = Q - L \quad (2.1.8)$$

Using equation (2.1.7), the components of the equation of motion become

$$\frac{\rho v^2}{r} = \frac{\partial P}{\partial r} + \rho g + \frac{1}{\mu_0} \left(\frac{\partial}{\partial r} \left(\frac{B^2}{2} \right) + \frac{B^2}{r} \right) \quad (2.1.9)$$

$$\rho \frac{v}{r} \frac{\partial v}{\partial m} = - \frac{1}{r} \frac{\partial P}{\partial m} - \frac{B_\psi}{\mu_0} \left[\frac{1}{r} \frac{\partial B_\psi}{\partial m} - \frac{1}{r \sin m} \frac{\partial B_m}{\partial \psi} + \frac{B_\psi}{r \tan m} \right] \quad (2.1.10)$$

$$0 = - \frac{1}{r \sin m} \frac{\partial P}{\partial \psi} - \frac{B_m}{\mu_0} \left[\frac{1}{r \sin m} \frac{\partial B_m}{\partial \psi} - \frac{1}{r} \frac{\partial B_\psi}{\partial m} - \frac{B_\psi}{r \tan m} \right] \quad (2.1.11)$$

where Ampere's law (2.1.3d) was used to substitute the magnetic field for the current density. One additional equation is obtained by substituting (2.1.6) into Gauss's Law (2.1.3b):

$$\frac{1}{r} \frac{\partial}{\partial m} B_m + \frac{B_m}{r \tan m} + \frac{1}{r \sin m} \frac{\partial B_\psi}{\partial \psi} = 0 \quad (2.1.12)$$

Equation (2.1.8) through (2.1.12) form the mathematical framework for the horizontal flow/field model.

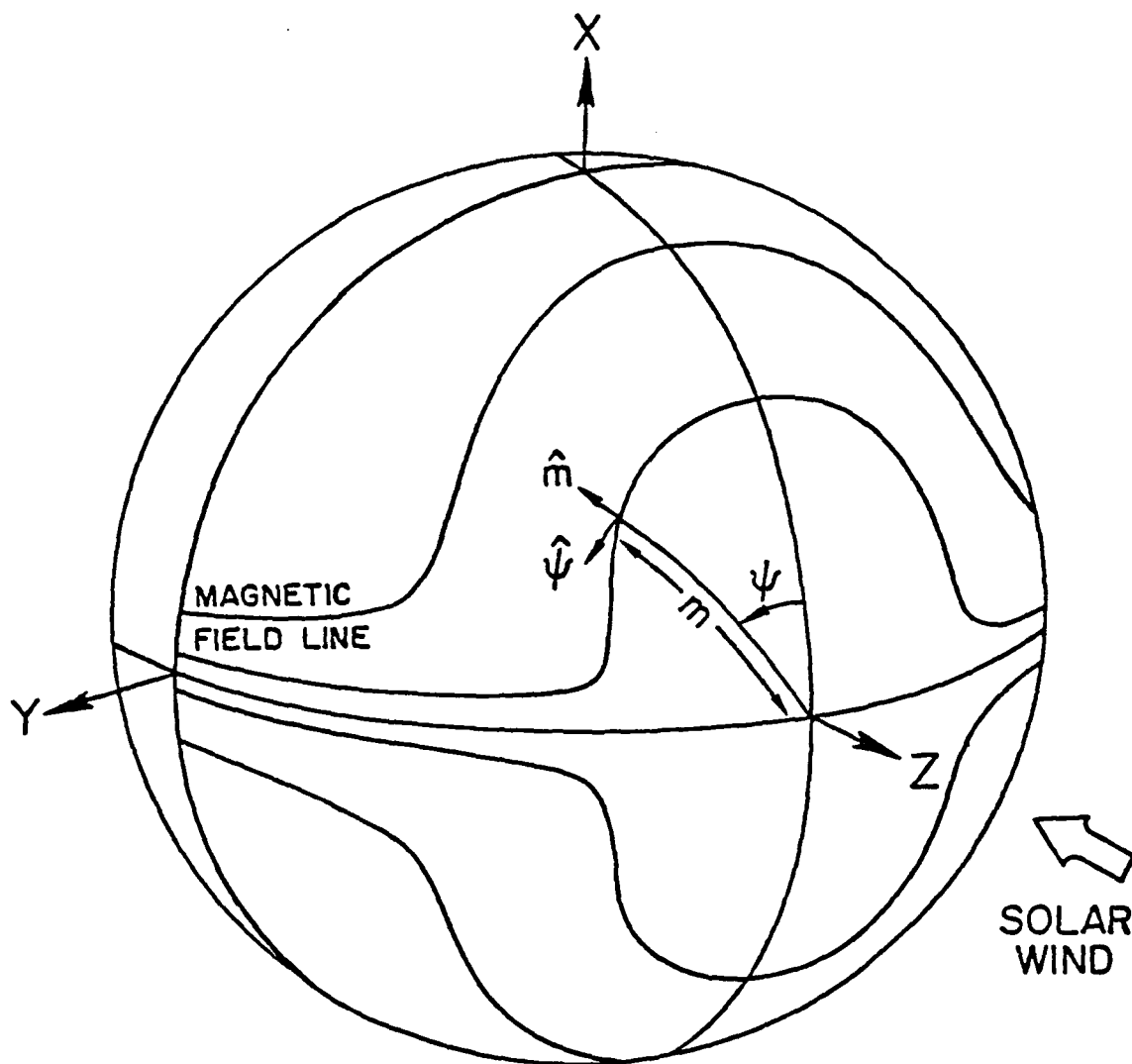


Figure 2-1. Coordinate system. The coordinates are aligned so that the Z axis is in the anti-sunward direction, the X axis is perpendicular to the IMF direction and the Y axis is parallel to the IMF. Also shown are the polar angle m , the azimuthal angle ψ , and the surface unit vectors \hat{m} and $\hat{\psi}$.

2.2 Plasma Flow Asymmetry

It's easiest to analyze the plasma flow at the prime meridian terminator and equatorial plane terminator because of published electron density and temperature data near these locations (Kliore et al., 1979; Brace et al., 1979; Miller et al., 1980; Theis et al., 1980). In the following analysis, the flow direction is referenced with respect to the external IMF direction. That is, parallel and perpendicular labels refer to directions parallel and perpendicular to the IMF orientation. In Figure 2-1, the IMF is assumed to be in the ecliptic plane and, therefore, v_{\parallel} is within the equatorial plane of Venus and v_{\perp} is along the noon meridian. We have also assumed that within the ionosphere, the magnetic field lines remain closely coupled (long diffusion time--see Section 2.4) with the plasma flow. Figure 2-1 qualitatively shows the field lines being carried along by the ionospheric plasma flow.

In the equatorial plane, for horizontal flow and fields: $\underline{v} = v_{\parallel} \hat{m}$ and $\underline{B} = B_m \hat{m}$. That is, within the equatorial plane the magnetic field is aligned parallel to the flow. Under steady state conditions, the continuity and momentum equations become:

$$\rho \frac{\partial v_{\parallel}}{\partial m} + \frac{v_{\parallel}}{r} \frac{\partial \rho}{\partial m} = Q - L \quad (2.2.1)$$

$$\rho \frac{v_{\parallel}^2}{r} = \frac{\partial P}{\partial r} + \rho g + \frac{1}{\mu_0} \left(\frac{\partial}{\partial r} \left(\frac{B_m^2}{2} \right) + \frac{B_m^2}{r} \right) \quad (2.2.2)$$

$$\rho \frac{v_{\parallel}}{r} \frac{\partial v_{\parallel}}{\partial m} = - \frac{1}{r} \frac{\partial P}{\partial m} \quad (2.2.3)$$

$$0 = - \frac{1}{r \sin m} \frac{\partial P}{\partial \phi} - \frac{1}{\mu_0 r \sin m} \frac{\partial}{\partial \phi} \left(\frac{B_m^2}{2} \right) \quad (2.2.4)$$

The plasma mass density is

$$\rho = n_i m_i + n_e m_e \approx n_e m_i \quad (2.2.5)$$

where we have assumed the ionosphere is quasi-neutral ($n_e \approx n_i$). As written, (2.2.5) is for one ion species, but it can be easily generalized to any number of ion species. Substituting (2.2.3) into (2.2.1), we find

$$- \frac{1}{v_{\parallel} r} \frac{\partial P}{\partial m} + \frac{v_{\parallel}}{r} \frac{\partial \rho}{\partial m} = Q - L \quad (2.2.6)$$

Equation (2.2.6) is just a quadratic equation in v_{\parallel} which has the solution

$$v_{\parallel} = \frac{(Q - L) + [(Q - L)^2 + \frac{4}{r^2} \frac{\partial P}{\partial m} \frac{\partial \rho}{\partial m}]^{1/2}}{\frac{2}{r} \frac{\partial \rho}{\partial m}} \quad (2.2.7)$$

where the gradients are evaluated near the parallel plane terminator. All the terms on the right hand side of (2.2.7) are derivable from observations.

The velocity along the noon meridian (v_{\perp}) is derivable in a similar way, with: $B = B_{\phi} \hat{\phi}$ and $\chi = v_{\perp} \hat{m}$. That is,

along the perpendicular direction (see Figure 2-1), B is always perpendicular to v . The resulting equation is

$$v_{\perp} = \frac{(Q-L) + \left[(Q-L)^2 + \frac{4}{r^2} \frac{\partial \rho}{\partial m} \left[\frac{\partial P}{\partial m} + \frac{1}{\mu_0} \frac{\partial}{\partial m} \left(\frac{B_{\psi}^2}{2} \right) \right] \right]^{1/2}}{\frac{2}{r} \frac{\partial \rho}{\partial m}} \quad (2.2.8)$$

where the gradients are evaluated near the perpendicular plane terminator. The 'least-energy' calculation of Cloutier and Daniell (1979) shows that along the perpendicular direction, the magnetic gradients at the terminator are very small and, therefore, they contribute very little to the magnitude of v_{\perp} . In both equations (2.2.7) and (2.2.8), the plasma is assumed to be a simple ideal gas where

$$P = n_e k (T_e + T_i) \quad (2.2.9)$$

and near the terminator $T_e \approx 2 T_i$ (Bauer et al., 1979; Brace et al., 1979a; Knudsen et al., 1979; Miller et al., 1980).

The parallel density gradients are obtained from the average electron density data reported by Brace et al. (1979b) and Theis et al. (1980). Since the IMF is usually near the ecliptic plane (Ness, 1965; Brandt, 1970; Haymes, 1971; Hundhausen, 1978), and since the PV orbiter penetrates the Venus ionosphere near the planetary equator (Colin,

1980), then the average observed electron densities should be representative of the density gradients parallel to the IMF. Indirect evidence (Coffey, 1979; King, 1979; Mihalov et al., 1980; Slavin et al., 1980) supports the assumption that the IMF was nearly parallel to the ecliptic plane during the polar ionosphere occultation experiment of Kliore et al. (1979). Therefore, the polar occultation measurements provide the necessary data for estimating the density gradients along the perpendicular direction. At the terminator, the production rate is approximately zero ($Q \approx 0$) and the loss process is assumed to be rate limited by charge exchange reactions (Nagy et al., 1979, 1980). The analysis is for a single ion species, O^+ , which predominates at high altitudes (Taylor et al., 1979a, 1979b, 1980) and the reaction rates are from Bauer et al. (1979) and Nagy et al. (1980). Neutral densities are available from Nieman et al. (1979a, 1979b, 1980) and von Zahn et al. (1979, 1980). Substitution of the above information into equations (2.2.7) and (2.2.8) results in the estimates of v_{\perp} and v_{\parallel} shown in Figure 2-2. The range of values for v_{\perp} and v_{\parallel} are due to chemistry and density gradient uncertainties.

The results shown in Figure 2-2 appear, at first, to be intuitively incorrect. One might guess that flow perpendicular to the magnetic field should be restrained by field tension and, therefore, v_{\perp} should be smaller than v_{\parallel} . In fact, the opposite occurs: the magnetic field enhances the

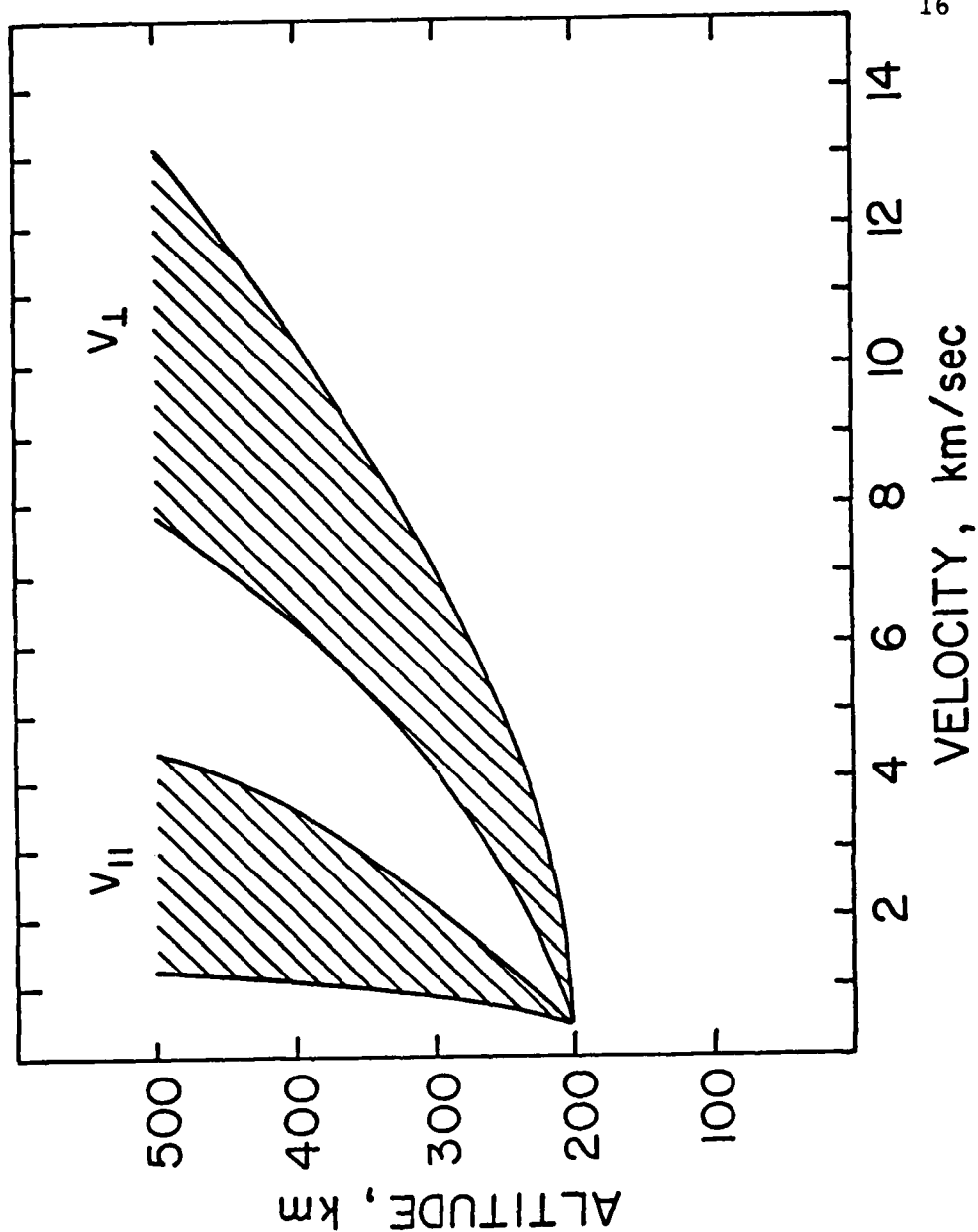


Figure 2-2. Velocity profiles. The range of values for the parallel (v_{\parallel}) and perpendicular (v_{\perp}) velocities are due to the uncertainties in the ionospheric chemistry and density measurements. The velocity calculation is arbitrarily terminated at 200 km because below this altitude chemistry dominates over dynamics.

perpendicular flow velocity. This result is consistent with the conclusions of the plasma depletion study of Zwan and Wolf (1976). They found that as a flux tube passes through the magnetosheath (or ionosheath for Venus), it experiences a loss of plasma and an accompanying increase in magnetic pressure in order to maintain pressure balance with the ambient environment. Zwan and Wolf showed that the plasma depletion mechanism is not axisymmetric and the resulting velocity asymmetry ($v_{\perp} > v_{\parallel}$) increases in proportion to the amount of plasma depletion (see Table 2-1).

Table 2-1 lists the plasma depletion factor ($\rho^*(t^*)/\rho^*(0)$) and the velocity asymmetry ratio (v_{\perp}/v_{\parallel}) as a function of the dimensionless parameter t^* which is a measure of how long a flux tube resides near the ionopause. Longer resident times allow for more plasma depletion and, therefore, larger asymmetries. Physically, the velocity asymmetry is due to the fact that the complete pressure gradient (gas and fields) is available to accelerate the plasma perpendicular to the fields, whereas only the smaller gas gradient is available to accelerate the plasma along the field lines. That is, in the depletion layer, the gas pressure is less than (or equal to) the magnetic pressure.

Another important feature of Figure 2-2 is that, within the ionosphere, the computed velocity asymmetry is most pronounced at high altitudes. The maximum asymmetry occurs around the stagnation region because this is the area where

the highly asymmetric ionosheath plasma flow enters the ionosphere. At lower altitudes, the velocity asymmetry is reduced due to frequent collisions with the ambient, thermal ionospheric ions. The magnitudes of the plasma flow velocities shown in Figure 2-2 are consistent with the PV observations of Knudsen et al. (1980, 1981).

Thus far, the only assumption about the ionospheric plasma flow is that the streamlines are radial lines centered at the plasma flow origin. Knudsen et al. (1981) indicate that the plasma pressure gradient is the principal accelerating mechanism well below the ionopause. Unfortunately, the lack of detailed azimuthal density observations makes it impossible to accurately compute the plasma acceleration as a function of solar zenith angle. Therefore, we will also assume that the flow velocity remains constant along any given streamline. Physically, this assumption isn't too bad. Using the electron data of Brace et al., one can compute the approximate pressure gradients along the parallel direction; by the time the dayside plasma reaches the terminator, these pressure gradients have increased the initial entry plasma velocity (~ 2 km/sec) by only about 20%.

TABLE 2-1.⁺

PLASMA DEPLETION FACTOR

t^*	$\rho^*(t^*)/\rho^*(0)$	v_{\perp}/v_{\parallel}
0	1.0	1.0
.2	.84	1.28
.41	.66	1.72
.61	.48	2.38
.82	.35	3.22
1.02	.27	4.35
1.22	.17	6.25

(⁺ from R. A. Wolf, private communication, 1980).

2.3 Magnetic Field Equations

The horizontal flow/field assumption, combined with the assumption that the plasma streams radially away from the sub-flow region, produces the separation of the magnetic field terms from the plasma velocity in the equations of motion (2.1.9-2.1.11). That is, equation (2.1.11) used with Gauss's Law (2.1.12) completely describes the magnetic field configuration and these coupled inhomogeneous differential equations depend only on the azimuthal pressure gradient ($\frac{\partial P}{\partial \psi}$). The solution to these differential equations is complicated, but straightforward, as shown in Appendix 1. The resulting magnetic field equations are:

$$\frac{B_m}{B_0} = B_{m_0} + \frac{(a_2 - a_1 \cos m) \sin \phi}{\sin^2 m} \quad (2.3.1a)$$

$$B_{m_0} = \frac{a_0(\phi - \sin \phi)}{\sin m} \quad (2.3.1b)$$

$$\frac{B_\phi}{B_0} = \frac{(a_1 - a_2 \cos m) \cos \phi}{\sin^2 m} \quad (2.3.2)$$

where B_0 is the maximum magnetic field strength (stagnation point) and the integration constants a_0 , a_1 , and a_2 will be discussed later. The variable B_{m_0} is due to the effects of

the azimuthal pressure gradient. Near the perpendicular direction ($\psi = 0$), the field lines are nearly parallel to each other (see Figure 2-1) and since the plasma is free to move parallel to the magnetic field, (which will naturally minimize any azimuthal pressure gradient) then

$$\lim_{\psi \rightarrow 0} \frac{\partial P}{\partial \psi} = 0 \quad (2.3.3)$$

We also know that

$$\lim_{\psi \rightarrow 0} B_m = 0 \quad (2.3.4)$$

since along the perpendicular direction, the magnetic field is entirely parallel to $\hat{\psi}$. Substituting (2.3.1a) and (2.3.2) into (2.1.11) shows that

$$\frac{\partial B_{m0}}{\partial \psi} = \frac{\partial P}{\partial \psi} \quad (2.3.5)$$

which implies

$$\lim_{\psi \rightarrow 0} \frac{\partial B_{m0}}{\partial \psi} = 0 \quad (2.3.6)$$

The form of B_{m0} given in equation (2.3.1b) satisfies both the constraints of equation (2.3.6) and Gauss's Law (2.1.12). A more complete derivation of (2.3.1b) is given in Appendix 1. Therefore, equation (2.3.1b) parameterizes

the effects of the azimuthal pressure gradient on the magnetic field geometry without requiring detailed measurements of these gradients. In fact, such detailed measurements do not exist because the reported ionospheric densities are averaged by SZA without regards for daily variations of the magnetic field orientation. From day to day, Pioneer Venus samples the ionosphere at various azimuthal angles due to the IMF orientation changes. However, information about the azimuthal variability is lost in the averaging process.

Evaluation of the constants in equations (2.3.1) and (2.3.2) is complicated because all the necessary boundary conditions are not known. Fortunately, the constants a_1 and a_2 can be evaluated by a geometric argument and a_0 can be found from physical constraints imposed by observations. The following discussion will only highlight the arguments used to evaluate these constants; the detailed analysis is in Appendix 2.

In Section 2.2, it was shown that a velocity asymmetry exists within the ionosphere of Venus: $v_{\perp} > v_{\parallel}$. The simplest flow geometry is one in which the spatial velocity distribution is elliptical. That is,

$$v(r, m, \psi) = \frac{v_{\perp}(r, m) v_{\parallel}(r, m)}{[v_{\parallel}^2 \cos^2 \psi + v_{\perp}^2 \sin^2 \psi]^{1/2}} \quad (2.3.7)$$

where v is the flow speed at a given azimuthal angle, ψ . Since along the perpendicular direction the ionospheric

magnetic fields are closely coupled with plasma flow (long diffusion time--see section 2.4), then for small ψ , the field line shape must also be elliptical. At larger values of ψ , the field line shape changes because at $\psi = \pi/2$, the ionospheric field must be parallel to the IMF direction (see Figure 2-1).

Earlier, the angle θ was defined to be the angle between y and B . Therefore, at any point along a plasma streamline, the magnetic field can be defined as

$$B(m, \psi) = B(m, \psi) \cos \theta \hat{m} + B(m, \psi) \sin \theta \hat{\psi} \quad (2.3.8)$$

where $B(m, \psi)$ is the total field strength at the point (m, ψ) . Substituting (2.3.8) into the third equation of motion (2.1.11) yields

$$\frac{\partial}{\partial m} (\ln B) + \frac{1}{\tan m} = - \frac{1}{\sin m} \frac{\partial \theta}{\partial \psi} \quad (2.3.9)$$

where azimuthal pressure gradients have been ignored because ψ is assumed to be small (see Appendix 1). The geometric constraint that the field lines be nearly elliptical (see equation (A.2.19)) requires that

$$\frac{\partial \theta}{\partial \psi} = - \cos m \left(1 - \frac{a^2}{b^2} \right) \quad (2.3.10a)$$

where

$$a = r \sin \left(\frac{v_{\perp} t}{r} \right) \quad (2.3.10b)$$

$$b = r \sin \left(\frac{v_{\parallel} t}{r} \right) \quad (2.3.10c)$$

and

$$\frac{a}{b} \equiv \text{asymmetry factor} \quad (2.3.10d)$$

Substituting (2.3.10a--2.3.10d) into (2.3.9) and integrating gives

$$\ln \left(\frac{B}{B_i} \right) = - \frac{1}{2} \int_{m_i}^m \frac{\sin(2m)}{\sin^2 \left(\frac{b}{a} m \right)} dm \quad (2.3.11)$$

Equation (2.3.11) is valid in the limit that ψ goes to zero and the integral is solvable for a variety of asymmetry factors (see Table A1-1). Furthermore, using equation (2.3.2), the left hand side of (2.3.11) becomes

$$\ln \left(\frac{B}{B_i} \right) = \ln \left[\frac{(a_1 - a_2 \cos m) \sin^2 m_i}{(a_1 - a_2 \cos m_i) \sin^2 m} \right] \quad (2.3.12)$$

Combining (2.3.12) with (2.3.11), the constants a_1 and a_2 can be solved relative to some assumed initial value of B . Therefore, the two unknowns, a_1 and a_2 , have been replaced by a single unknown, B_i , which is a model input.

In order to solve for the constant a_0 , one needs to determine how the field strength varies with solar zenith

angle along the parallel direction. Vaisberg et al. (1980a, 1980b) report that the best fit to the SZA variation of the observed ionopause field strength is

$$\frac{B(\text{SZA})}{B_0} \approx \cos^2 \chi \quad (2.3.13)$$

where B_0 is the nose value (stagnation point) for B and χ is the angle between the ionopause and the solar wind direction at a given SZA. However, equation (2.3.13) cannot be used directly because the PV observations used in the Vaisberg analysis were taken over a period of weeks as the orbit precessed toward the terminator. During this time, there is no way to establish the location of the sub-flow point and the magnetic field orientation. Therefore, equation (2.3.13) is of limited value. This equation does show, however, that the field strength near the terminator can be very large and it also proves to be useful guide in the determination of the constant a_0 .

The constant a_0 is evaluated by an iterative technique described in Appendix 2. The iteration method consists of estimating an initial value of B along the parallel direction and then computing (using a_1 and a_2) both the magnetic field lines and field strengths everywhere in the ionosphere. The value of a_0 is adjusted until the magnetic longitude variation of the magnetic field strength approximates the behavior of equation (2.3.13). By varying the

inputs, a library of different ionospheric flow/field configurations is generated. Since the constant a_0 represents the effects of the density gradients on the ionospheric field geometry, then by selecting various combinations of a_0 , a_1 and a_2 we are effectively showing how the ionospheric magnetic fields change in response to changing ionospheric conditions.

In the proceeding discussion, the terms 'parallel' and 'perpendicular' described the ionospheric field geometry relative to the IMF orientation. Given the field geometry described in this section, some additional terminology is in order. The parallel direction is the "magnetic equator" of the ionospheric magnetic fields and the perpendicular direction is the "magnetic prime meridian." This terminology will be used in the remainder of this thesis.

2.4 Magnetic Field Asymmetry

In this section, we will show that the magnetic diffusion time is long compared to the transport time for the flow to carry the field lines across the surface of Venus. Therefore, the field lines are closely coupled with the flow and for small ψ , the magnetic field geometry will be nearly elliptical. The first step is to determine the diffusion time along the magnetic prime meridian.

We define a coordinate system which is unique to this section where the Z axis is always parallel to the magnetic fields. In order to simplify the analysis, we will assume that the field lines are nearly straight and that the plasma pressure gradients are weak. Under these conditions, the generalized Ohm's Law (Spitzer, 1963) becomes

$$\underline{J} = \underline{g} \cdot (\underline{E} + \underline{v} \times \underline{B}) \quad (2.4.1)$$

where

$$\underline{\sigma} = \begin{pmatrix} \sigma_1 & \sigma_2 & 0 \\ -\sigma_2 & \sigma_1 & 0 \\ 0 & 0 & \sigma_0 \end{pmatrix} \quad (2.4.2)$$

σ_1 is the Pedersen conductivity, σ_2 is the Hall conductivity, and σ_0 is the parallel or zero conductivity. Inverting (2.4.1) and solving for the electric field,

$$\vec{E} = \vec{g}^{-1} \cdot \vec{J} - \vec{v} \times \vec{B} \quad (2.4.3)$$

where

$$\vec{g}^{-1} = \begin{pmatrix} \frac{\sigma_1}{(\sigma_1^2 + \sigma_2^2)} & \frac{-\sigma_2}{(\sigma_1^2 + \sigma_2^2)} & 0 \\ \frac{\sigma_2}{(\sigma_1^2 + \sigma_2^2)} & \frac{\sigma_1}{(\sigma_1^2 + \sigma_2^2)} & 0 \\ 0 & 0 & \frac{1}{\sigma_0} \end{pmatrix} \quad (2.4.4)$$

Next, substituting (2.4.3) into Faraday's Law gives

$$\nabla \times [\vec{g}^{-1} \cdot (\frac{\nabla \times \vec{B}}{\mu_0})] - \nabla \times (\vec{v} \times \vec{B}) = - \frac{\partial \vec{B}}{\partial t} \quad (2.4.5)$$

where Ampere's Law (2.1.3d) was used to substitute for the current density, \vec{J} . Since \vec{B} is aligned along the z axis, equation (2.4.5) becomes

$$\frac{1}{\mu_0} \frac{\sigma_1}{\sigma_1^2 + \sigma_2^2} \left[\frac{\partial^2 B}{\partial y^2} + \frac{\partial^2 B}{\partial x^2} \right] \hat{k} - \nabla \times (\vec{v} \times \vec{B}) = - \frac{\partial B}{\partial t} \hat{k} \quad (2.4.6)$$

For a fluid at rest, (2.4.6) reduces to the diffusion equation

$$\frac{1}{\mu_0 \sigma_3} \left[\frac{\partial^2 B}{\partial y^2} + \frac{\partial^2 B}{\partial x^2} \right] = - \frac{\partial B}{\partial t} \quad (2.4.7)$$

where

$$\sigma_3 = \sigma_1 + \frac{\sigma_2^2}{\sigma_1} \quad (2.4.8)$$

and σ_3 is the Cowling conductivity. That is, an initial configuration of magnetic field will decay in a diffusion time

$$\tau = \mu_0 \sigma_3 L^2 \quad (2.4.9)$$

The Pedersen and Hall conductivities for Venus were computed by Daniell (1976); these conductivities and the associated diffusion times are listed in Table 2-2. The diffusion distance (L) is 6000 km or approximately the radius of Venus. Using a plasma flow velocity of approximately 2 km/sec, the travel time across 6000 km is less than one hour, compared to a high altitude diffusion time of more than 100 hours. Therefore, the magnetic fields are closely coupled with the ionospheric plasma flow. Since the plasma flow geometry for small ϕ is elliptical, then the magnetic field geometry near the magnetic prime meridian must also be approximately elliptical. However, the field asymmetry does

not completely reflect the flow asymmetry because the field asymmetry does not change with altitude.

The calculations of Cloutier et al. (1981) show that at high altitudes, the contours of constant magnetic field strength are nearly vertical lines along the magnetic prime meridian. This behavior is shown in Figure 2-3; the field strength contours are labeled as a fraction of the total field strength (i.e. 0.5, 0.4, etc.). The contours are nearly vertical because, as seen from Table 2-2, the diffusion time decreases with increasing altitude so that the field can slip faster through the plasma at high altitudes. The 'least energy' calculations of Cloutier and Daniell (1979) show that the slippage rate is such that the field strength remains relatively constant with altitude, even though the plasma flow velocity increases with altitude.

Along the magnetic equator, an exact calculation of the scalar conductivity requires detailed information about both the electron temperature and density. Fortunately, such a calculation is unnecessary because the horizontal flow-field assumption allows one to solve the generalized Ohm's Law along the magnetic equator. The details of this calculation are shown in Appendix 3. The final result of the analysis (A.3.10) is

$$\frac{B(h_2)}{B(h_1)} \approx 1 \quad (2.4.10)$$

TABLE 2.2. CONDUCTIVITY AND DIFFUSION TIME

<u>alt (km)</u>	<u>σ_1 (mho/m)</u>	<u>σ_2 (mho/m)</u>	<u>τ (sec)</u>
200	.08	.4	9.4×10^7
250	.08	.02	3.8×10^6
300	.01	10^{-3}	4.6×10^5
350	7×10^{-3}	4×10^{-4}	3.2×10^5
400	6×10^{-3}	2×10^{-4}	2.7×10^5
450	5×10^{-3}	9×10^{-5}	2.3×10^5
500	4×10^{-3}	8×10^{-5}	1.8×10^5

Figure 2-3. Magnetic prime meridian plane current system. The ionopause shape follows that of Spreiter et al. (1970). Contours are labeled according to the fraction of the current lying outside that contour at the local longitude. The ionosheath contours (dashed lines) are closed loops extending out to the bow shock. The straight dashed lines within the ionosphere (labeled 0.1, 1.0, 10.) are contours of constant magnetic Reynolds number. In the 2-D model, the current distribution is assumed to be uniform over a wide variety of longitudes around the prime meridian plane, and therefore, the contours also represent magnetic field strength contours. The field lines are perpendicular to the plane of the figure and the contour labels also indicate the fraction of total magnetic field strength along each contour.

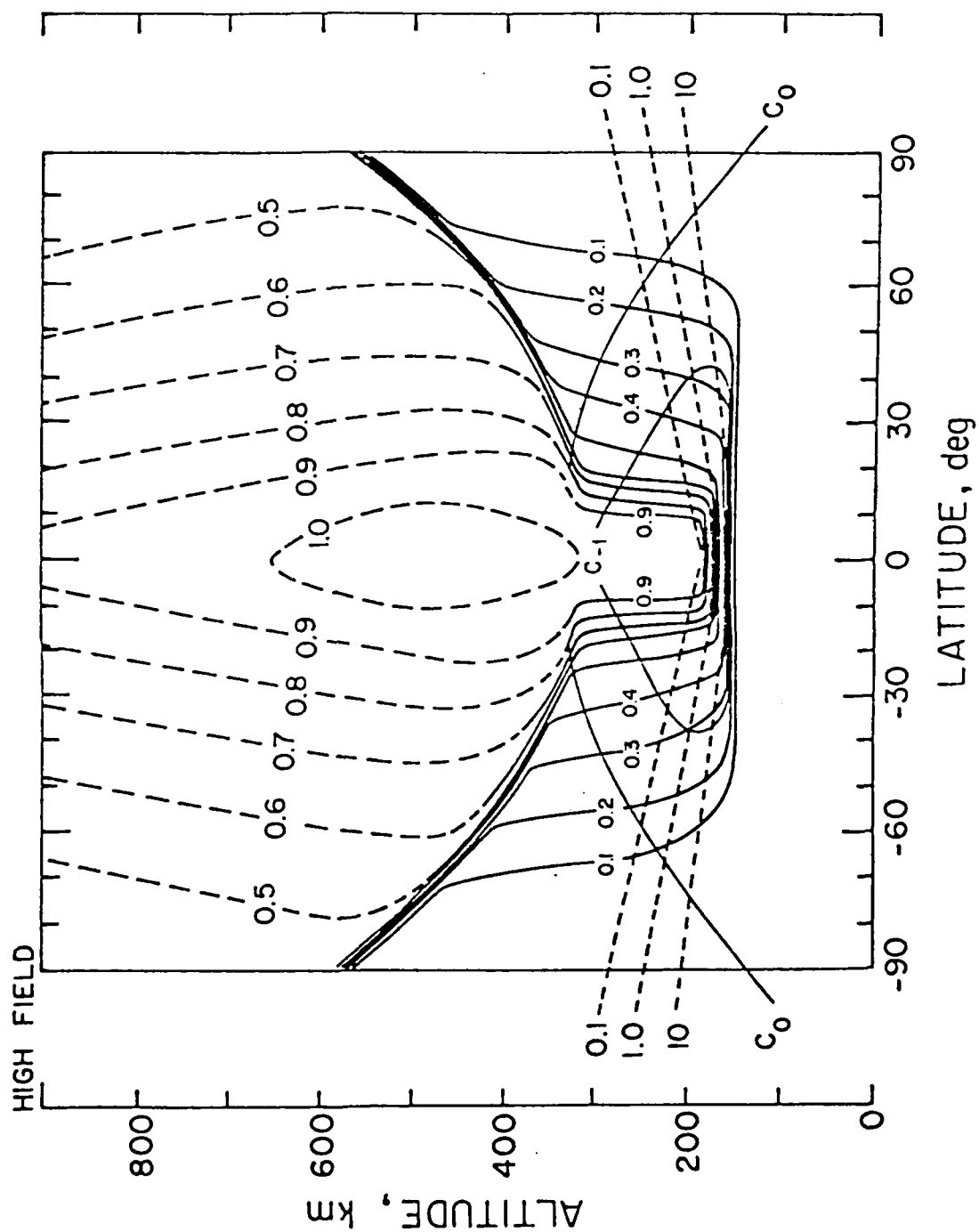


Figure 2-3

where the numerator is the magnetic field strength at height h_2 , and the denominator is evaluated at height h_1 ($h_2 > h_1$); the field strengths are computed at the same longitude. Therefore, the contours of constant magnetic field strength are vertical lines along both the magnetic equator and the magnetic prime meridian.

It is not possible to evaluate the field strength height variability at any other azimuthal angle and therefore, we will make the simplifying assumption that, at high altitudes, the ionospheric field strength contours are vertical everywhere. It follows then that the magnetic field asymmetry factor must remain constant with altitude. Otherwise, the high altitude field lines would be carried towards the terminator faster than the low altitude field lines and, under these conditions, the field strength will not remain constant with altitude. The exact field asymmetry factor will depend on the physical conditions of the ionosphere. From day to day, changes in the solar wind dynamic pressure and IMF orientation will cause changes in both the ionospheric flow and field configurations. These changes will in turn effect the ionospheric conductivity which, ultimately, determines the amount of field asymmetry. Further, it's impossible to predict a priori the field asymmetry factor for a given day. In practice, the model (Chapter 3) is run for a variety of field asymmetry factors and then the best match is found for a specific set of observations.

2.5. Instability Criterion.

The presence of a large ionospheric plasma velocity shear (see Figure 2-2) makes the Venus ionosphere susceptible to magnetohydrodynamic instabilities, such as the Kelvin-Helmholtz instability. This instability occurs (Hesagawa, 1975) whenever

$$\rho (\mathbf{k} \cdot \mathbf{V}_0)^2 > \left(\frac{\mathbf{k} \cdot \mathbf{B}}{\mu_0} \right)^2 \quad (2.5.1)$$

where ρ is the plasma mass density which is flowing at a relative velocity \mathbf{V}_0 with respect to adjacent plasma of the same density, and \mathbf{B} is a uniform magnetic field extending throughout both plasma regions. Both \mathbf{B} and \mathbf{V}_0 are parallel to the plane across which the velocity shear is supported. Maximum stability occurs for all wave modes when \mathbf{V}_0 is parallel to \mathbf{k} and \mathbf{B} , and the instability is most likely to occur when \mathbf{V}_0 is parallel to \mathbf{k} and perpendicular to \mathbf{B} . Equation (2.5.1) can be simplified by assuming that all unstable wave modes always occur parallel to the flow direction and therefore,

$$\rho V_0^2 > \frac{B^2 \cos^2 \theta}{\mu_0} \quad (2.5.2)$$

where θ is the angle between \mathbf{V}_0 and \mathbf{B} . As seen from (2.5.1) and (2.5.2), the Kelvin-Helmholtz instability is driven by the kinetic energy of the flowing plasma and is stabilized by

the magnetic tension. Generalization of (2.5.1), for a finite thickness boundary with continuous velocity shear and vertical density gradients, results in an instability criterion similar to (2.5.1) with the additional constraint that the finite thickness boundary is stable for short wavelengths (Ong and Roderick, 1972). In the flow/field model, the simple expression (2.5.2) is used to identify regions of instability, subject to the wavelength constraints of Ong and Roderick.

In an earlier paper (Cloutier et al., 1981), it was shown that the Kelvin-Helmholtz instability is responsible " for regions of twisted bundles of magnetic fields, called 'flux-ropes,' which are observed (Russell et al., 1979a, 1979b; Russell and Elphic, 1979; Elphic et al., 1980) in the Venus ionosphere. A qualitative picture of the sequence of events leading to the formation of flux-ropes is shown in Figure 2-4 (panels a-c). That is, a perturbation at the shear boundary produces a wave which pushes the boundary region into an area of increasing plasma flow velocity. The velocity shear causes the wave crest to advance faster than the wave trough, resulting in the wrapping up of the field lines into discrete bundles spaced at intervals of $2\pi/k$. In the above example, V_0 is perpendicular to B which is the most unstable case. The bottom panel (d) of Figure 2-4 shows a schematic view of the interior of a flux rope (Russell et al., 1979b) which is representative of the case

KELVIN-HELMHOLTZ INSTABILITY

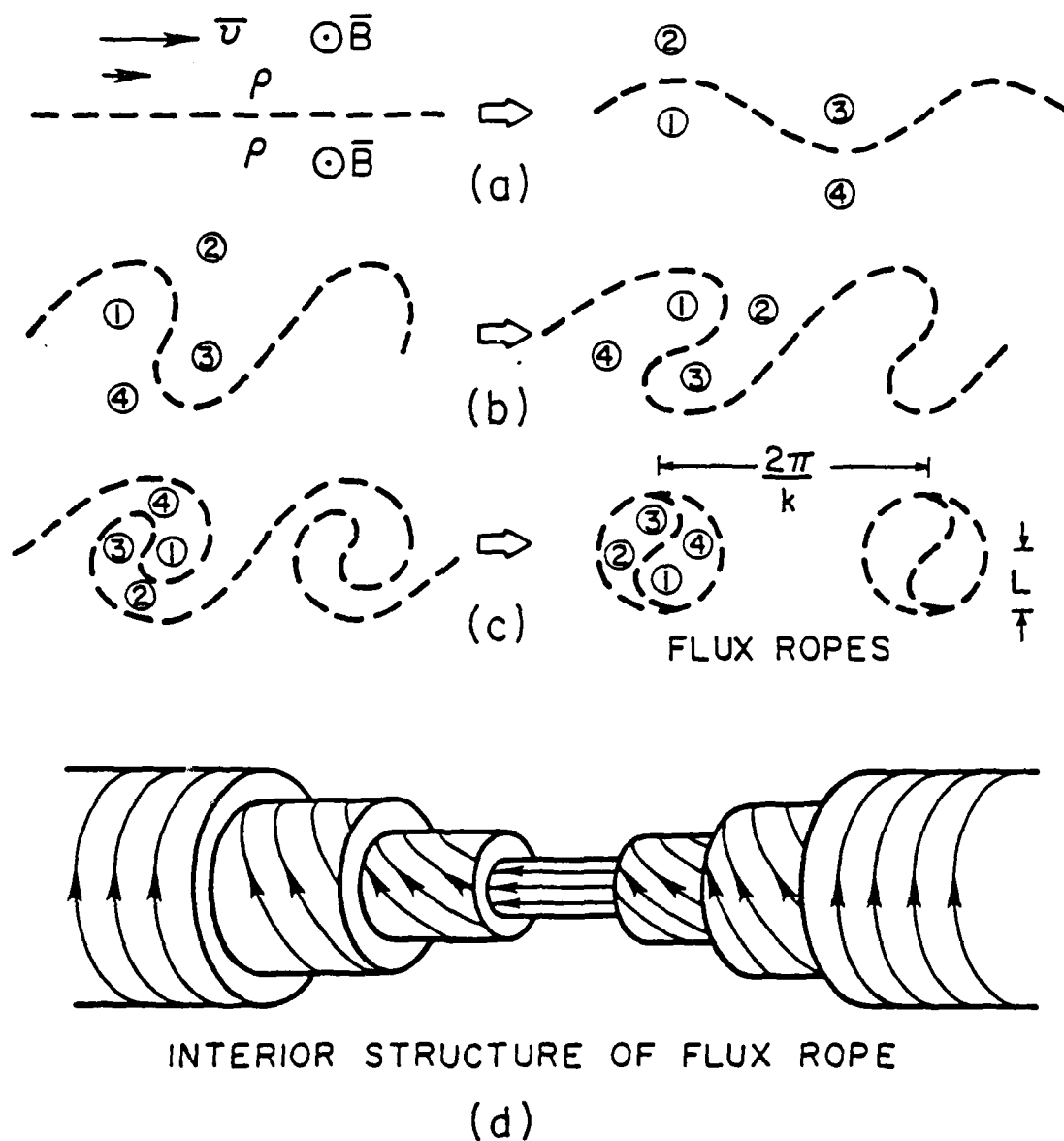


Figure 2-4. Sequence a-c schematically shows the formation of flux ropes by the Kelvin-Helmholtz instability. Sample field lines are labeled by the number 1 to 4. Panel d shows the interior structure of a flux-rope (from Russell *et al.*, 1979b).

where \mathbf{V}_0 and \mathbf{B} are not perpendicular. Since the total magnetic flux within a large volume containing the flux-rope must be conserved, the average field between the flux-rope must be very small when the field within the flux-rope is relatively large.

The actual amount of magnetic flux within the flux-rope is a function of the azimuthal angle, ϕ . The flux-rope contains significant magnetic flux whenever \mathbf{V}_0 is perpendicular to \mathbf{B} since a large number of field lines are bundled up in each flux rope. However, when \mathbf{V}_0 is parallel to \mathbf{B} , the magnetic flux within the flux-rope is zero because, instead of gathering up field lines, the parallel flow just rolls up the field along the direction of \mathbf{B} . In general, the PV orbit passes through regions which vary between these two extremes so that the measured flux-rope field strength will often change dramatically along the orbit.

Cloutier et al. (1981) also showed that the flux-rope diameter is a function of height. That is, the finite conductivity of the Venus ionosphere is an additional complication to the formation of flux-rope. In order to maintain flux-rope formation, the convection velocity of the plasma wrapping up the field must exceed the diffusion rate of the field through the plasma. The ratio of the plasma convection velocity, V , to the magnetic diffusion rate is called the magnetic Reynolds number (Jackson, 1975). Along the

magnetic prime meridian,

$$R_{m\perp} = \frac{V_{\perp}}{(L/\tau)} = \mu_0 \sigma_3 V_{\perp} L \quad (2.5.3)$$

where σ_3 is Cowling conductivity (see Section 2.4) and L is the scale length of the magnetic perturbation (radius of the flux-rope). The straight dashed lines in Figure 2-3 are contours of constant magnetic Reynolds number for the prime magnetic meridian plane; these contours are labelled with the value of R_m . Since σ_3 and V_{\perp} are known at each altitude, the contours of R_m define the scale size of the flux-ropes formed at a given altitude. Further, since least-action favors formation of the smallest possible flux-ropes, subject to the short wavelength constraints of Ong and Roderick (1972), the computations show that within the unstable regions the flux-rope size distribution should vary from large flux-ropes at high altitudes to small flux-ropes at low altitudes.

A similar analysis can be done along the magnetic equator where the magnetic Reynolds number now becomes

$$R_{m\parallel} = \mu_0 \sigma_0 V_{\parallel} L \quad (2.5.4)$$

where the scalar conductivity is

$$\sigma_0 = \frac{n_e e^2}{m_e v_{ei} + \left(\frac{1}{m_e v_{en}} + \frac{1}{m_i v_{in}} \right)^{-1}} \quad (2.5.5)$$

Hanson (1965) gives the following empirical expressions for the ion and electron collision frequencies used in equation (2.5.5)

$$\nu_{en} = 5.4 \times 10^{-10} n_n T_e^{1/2} \quad (2.5.6)$$

$$\nu_{ei} = [34 + 4.18 \log \left(\frac{T_e^3}{n_e} \right)] n_e T_e^{-3/2} \quad (2.5.7)$$

$$\nu_{in} = 2.6 \times 10^{-9} (n_n + n_i) M^{-1/2} \quad (2.5.8)$$

where n_n is the neutral density, T_e is the electron temperature, n_e is the electron density, n_i is the ion density, and M is the molecular weight of the ions and neutral particles (assumed to have the same mass). Using the neutral densities of Niemann et al. (1980) and von Zahn et al. (1979, 1980), and the electron density and temperature data of Theis et al. (1980), one finds that in the dayside ionosphere, the electron-ion collision frequency (ν_{ei}) is more than two orders of magnitude larger than either the electron-neutral (ν_{en}) or ion-neutral collision (ν_{in}) frequencies. Therefore, substituting (2.5.7) into (2.5.5)

$$\sigma_o = \frac{e^2 T_e^{3/2}}{[34 + 4.18 \log \left(\frac{T_e^3}{n_e} \right)]} \quad (2.5.9)$$

Again, using the average electron density and temperature data of Theis et al. (1980), one finds that σ_0 varies slowly with altitude. Considering the uncertainties of the data, we will assume that the parallel conductivity is constant with altitude. Since the parallel velocity increases with altitude, the largest magnetic Reynolds numbers will occur at high altitudes for large flux-rope sizes. As discussed earlier, flux-ropes along the magnetic equator are characterized by nearly zero flux and therefore, observationally, their size is poorly defined.

In conclusion, the model would predict that within unstable regions, flux-ropes vary in size from large at high altitudes to small at low altitudes. This prediction is consistent with the flux-rope distribution statistics reported by Russell et al. (1979a, 1979b).

2.6 Summary

The following summary of equations form the basis of the computer model described in Chapter 3. The equation numbers are from the section in which the equations were derived.

The equations describing the horizontal plasma flow are:

$$\underline{v} = v \hat{m} \quad (2.1.5)$$

where

$$v = \frac{v_{\perp} v_{\parallel}}{(v_{\parallel}^2 \cos^2 \psi + v_{\perp}^2 \sin^2 \psi)^{1/2}} \quad (2.3.7)$$

and

$$v_{\parallel} = \frac{(Q-L) + [(Q-L)^2 + \frac{4}{r^2} \frac{\partial P}{\partial m} (\frac{\partial \rho}{\partial m})_{\parallel}]^{1/2}}{(\frac{2}{r} \frac{\partial \rho}{\partial m})_{\parallel}} \quad (2.2.7)$$

$$v_{\perp} = \frac{(Q-L) + [(Q-L)^2 + \frac{4}{r^2} \frac{\partial P}{\partial m} (\frac{\partial \rho}{\partial m})_{\perp}]^{1/2}}{(\frac{2}{r} \frac{\partial \rho}{\partial m})_{\perp}} \quad (2.2.8)$$

$$\frac{v_{\perp}}{v_{\parallel}} > 1 \quad (\text{see Figure 2-2})$$

$$\rho = n_e m_i \quad (2.2.5)$$

$$P = n_e k (T_e + T_i) \quad (2.2.9)$$

Q is the ion production rate, L is the ion loss rate, and O^+ is the predominant ion at high altitudes. As shown in Figure 2-2, the velocity asymmetry (v_{\perp}/v_{\parallel}) increases with altitude.

The horizontal magnetic fields are described by the following equations:

$$\vec{B} = B_m \hat{m} + B_{\psi} \hat{\psi} \quad (2.1.6)$$

where

$$\frac{B_m}{B_0} = \frac{a_0 (\psi - \sin\psi)}{\sin m} + \frac{(a_2 - a_1 \cos m) \sin\psi}{\sin^2 m} \quad (2.3.1)$$

$$\frac{B_{\psi}}{B_0} = \frac{(a_1 - a_2 \cos m)}{\sin^2 m} \cos\psi \quad (2.3.2)$$

where B_0 is the maximum field strength at the stagnation point. The constant a_0 parameterizes the azimuthal density gradient and the constants a_1 and a_2 determine the amount of magnetic field asymmetry. The magnetic asymmetry is constant with altitude.

Regions of instability occur whenever

$$\rho v^2 > \frac{B^2 \cos^2 \theta}{\mu_0} \quad (2.5.2)$$

where θ is the angle between γ and \underline{B} , and μ_0 is the magnetic permeability of free space.

The above equations were based on the following assumptions:

- 1) steady state conditions;
- 2) horizontal plasma flow and magnetic fields;
- 3) tangential IMF;
- 4) plasma flows radially away from flow origin;
- 5) flow speed is constant for all SZA;
- 6) unstable wave modes occur parallel to v .

Taken together, assumptions 1, 2 and 4 simplified the MHD equations enough so that analytic solutions were possible. Assumption 3 simplifies the ionosheath, plasma depletion and ionospheric current analyses. The lack of detailed density and pressure gradient information led to assumption 5. Finally, assumption 6 greatly simplifies the instability analysis.

3. NUMERICAL MODEL

3.1 Model Components

The computer model consists of three distinct regions. The largest region extends from m (polar angle) greater than 40° to the terminator, and is called the horizontal region. The other two regions are the "sub-flow" region ($0 < m < 10$) and the transition region ($10 < m < 40$). These regions are shown in Figure 3-1 along with the plasma flow streamlines.

The horizontal region is characterized by both horizontal plasma flows and horizontal magnetic fields. The equations describing the physics of this region are discussed in Section 2.5. In this region, the flow streamlines are radial lines centered at the plasma flow origin.

The "sub-flow" region describes the area where the ionosheath plasma enters the ionosphere. The word "sub-flow" is put in quotations because this region may or may not be aligned with the nose of the bow shock where the solar wind "flows" into the planetary obstacle (Russell et al., 1981). If the tangential IMF is orthogonal to the solar wind flow direction, then the nose of the bow shock and ionospheric "sub-flow" region are aligned (they also coincide with the subsolar point). However, the ideal case is rarely (if ever) attained. Generally, the IMF and radial solar wind flow are separated by some angle, ϕ (spiral angle or garden-hose angle). At Venus, the idealized spiral angle is about 35° (see Figure 3-2). At realistic spiral angles,

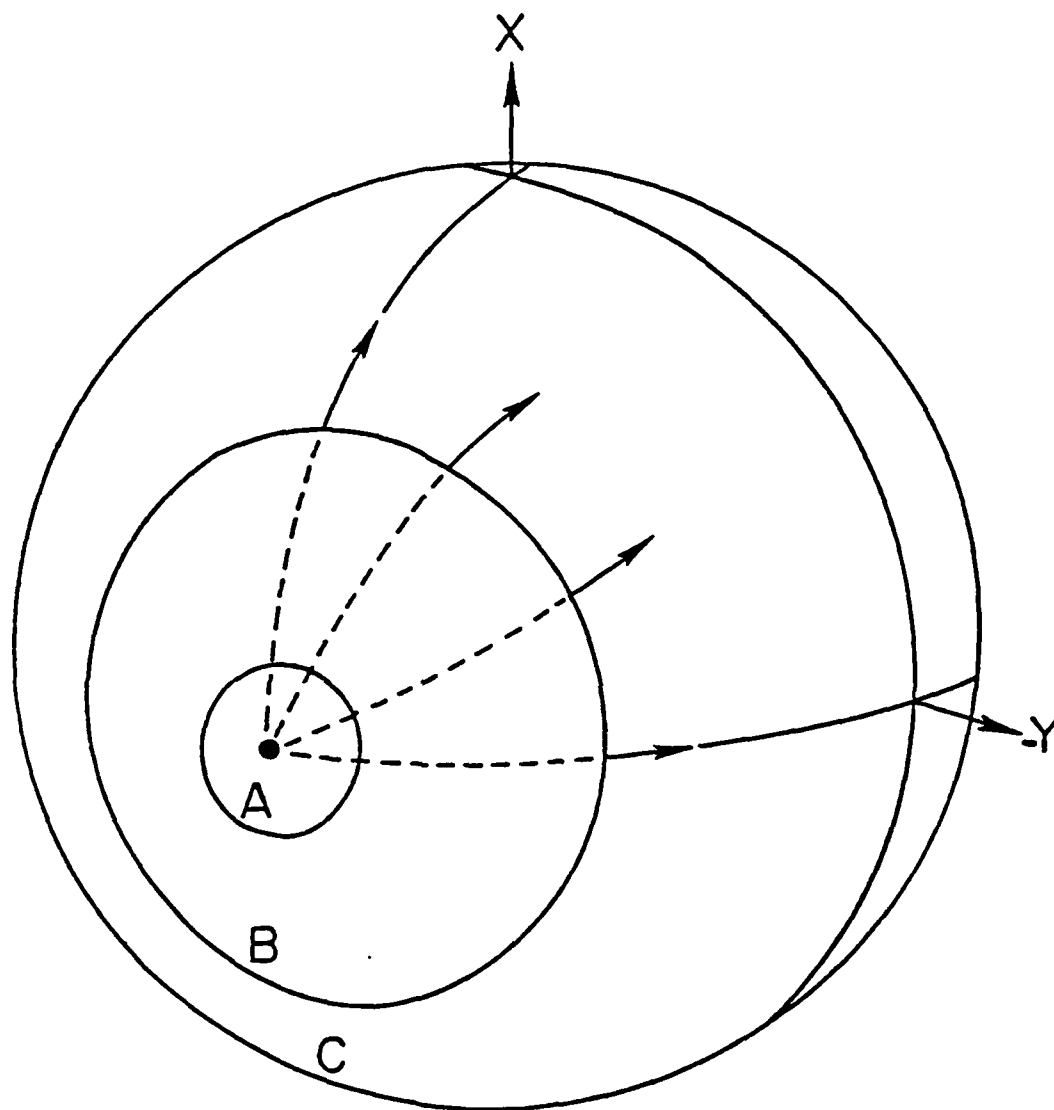


Figure 3-1. Model regions and radial flowlines. Region A is the sub-flow region ($0 < m < 10^0$), region B is the transition region ($10 < m < 40^0$) and region C is the horizontal region ($40 > m$). Also shown are the radial flow lines which are centered about the sub-flow point; the flow lines are parallel to the planet's surface in region C.

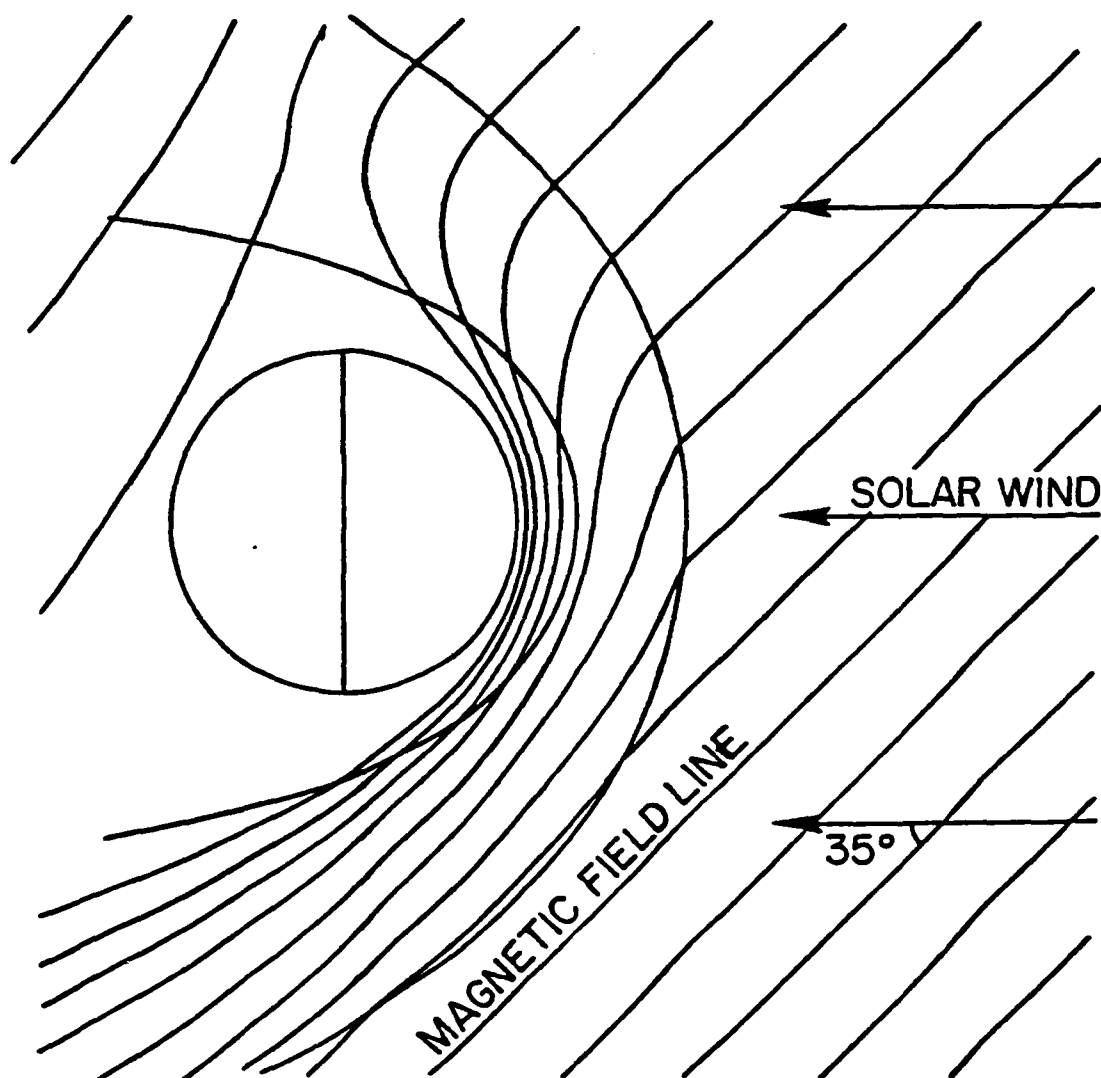


Figure 3-2. Distortion of the IMF resulting from interaction with the planetary ionosphere. The spiral angle is 35° (from Daniell 1976).

the shocked solar wind plasma has a component of velocity along the ionosheath magnetic field lines which diverts the sheath plasma flow from its initial radial (outward from the Sun) direction. The amount of flow diversion or "aberration" depends on the solar wind flow speed and the spiral angle, both of which are highly variable from day to day (King, 1981). Therefore, the sub-flow point will not usually be found at the same fixed planetary location from one day to the next. In the three dimensional model, we do not determine the exact location of the sub-flow point. Instead, the model computes the center of symmetry of the ionospheric magnetic fields (and the flow pattern), and one would expect that this symmetry center corresponds closely to the physical sub-flow point. A detailed calculation of the sub-flow location would require not only a sophisticated ionosheath model, but would also require data which is not available from PV observations.

In Figure 3-3, the idealized plasma flow streamlines are shown for three different areas: 1) outside the bow shock (straight lines); 2) within the ionosheath (curved solid lines); and 3) within the ionosphere (dashed lines). The shaded area corresponds to the "sub-flow" region and, in this region, the flow is nearly vertical. The weak horizontal flow of the sub-flow region is probably incapable of supporting the Kelvin-Helmholtz type instability, and thus the model assumes that the "sub-flow" region is always

stable. The magnetic field strength of the "sub-flow" region is determined from the two-dimensional electrodynamic model (Cloutier et al., 1981) and is maintained at 90% of the maximum field strength (stagnation point) across the entire "sub-flow" region.

The transition region describes the area where the vertically in-flowing plasma changes to strictly horizontal flow. Within the transition region, the magnetic field strength is again based on the two-dimensional electrodynamic model and is given by

$$B(m) = B(40^\circ) + \Delta B \times \left(\frac{40 - m}{30}\right)^2 \quad (3.1.1)$$

where ΔB is

$$\frac{\Delta B}{B_0} = 0.9 - B(40^\circ)/B_0 \quad (3.1.2)$$

The value of $B(40^\circ)$ is determined from the horizontal field equations (2.3.1) and (2.3.2). Equations (3.1.1) and (3.1.2) are applied at all azimuthal angles.

The instability criterion (2.5.2) depends on the angle θ between v and B . Within the horizontal flow region (see equation 2.3.8),

$$B_\psi(m, \psi) = B(m, \psi) \sin \theta \quad (3.1.3)$$

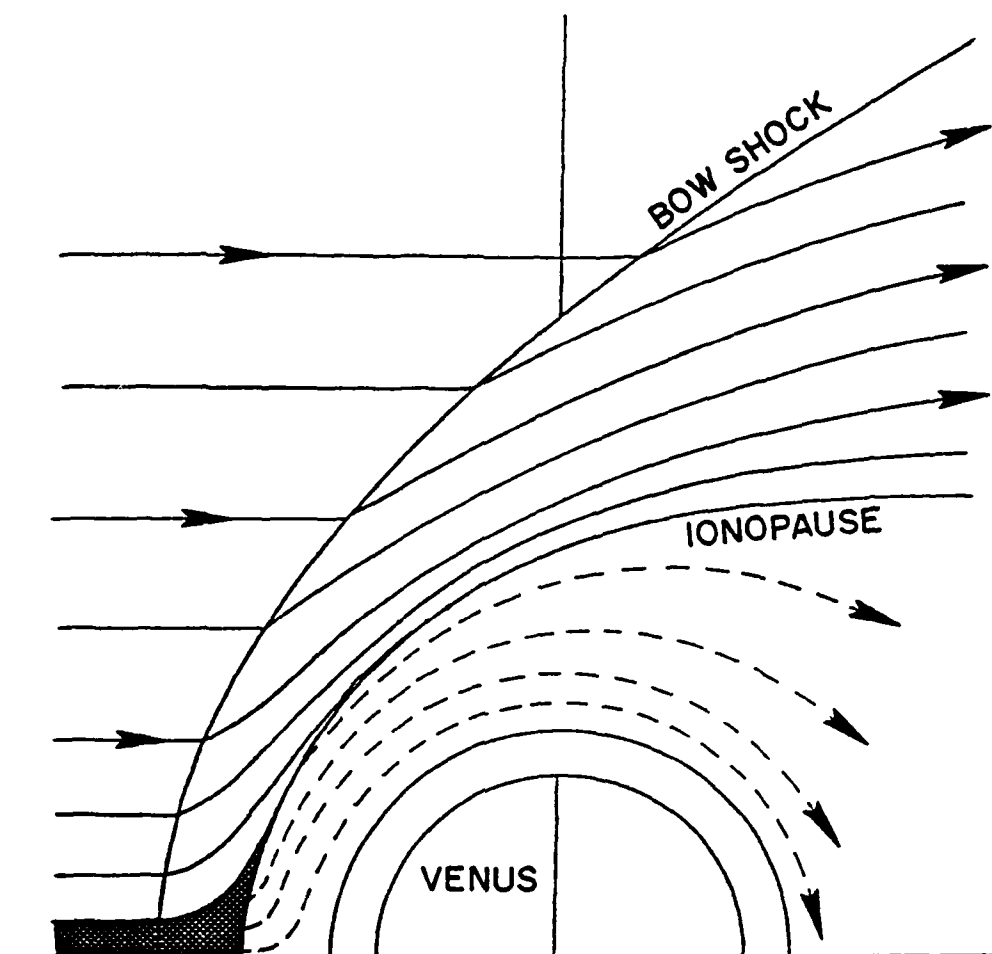


Figure 3-3. Ionosphere and ionosheath flowlines. The ionospheric entry region is shown by the shaded area.

$$B_m(m, \psi) = B(m, \psi) \cos \theta \quad (3.1.4)$$

and, therefore,

$$\theta = \tan^{-1} \left(\frac{B_\psi}{B_m} \right) \quad (3.1.5)$$

That is, the plasma flows along radial streamlines ($\chi = \hat{v}m$) and on a streamline, the local value of B is given by equations (3.1.3) and (3.1.4). As stated earlier, the "sub-flow" region is assumed to be stable and, therefore, θ is not computed for this region. In the transition region, θ is approximately given by

$$\theta(m) = \theta(40^\circ) + \left(\frac{40 - m}{10} \right) \quad (3.1.6)$$

Equation (3.1.6) is an empirical result which provides the necessary continuity with the results computed in the horizontal flow region.

One last point about the model concerns the shape and definition of the ionopause surface. There have been numerous attempts (Wolff et al., 1979; Vaisberg et al., 1980a,b; Brace et al., 1980; Elphic et al., 1980a,b; Theis et al., 1981) to understand the daily variability of the dayside ionopause location in terms of solar wind pressure dynamics. These studies have been moderately successful in describing

the average ionopause position, but lack the ability to describe daily ionopause variations in detail. Therefore, the model uses the in-situ measurements by the Orbiter Ion Mass Spectrometer (Taylor et al., 1979a,b, 1980) to determine the ionopause for each orbit analyzed. Physically, these measurements are the best way to identify the thermal ion boundary (i.e., ionopause). The OIMS measurements provide two measurements of the ionopause location for each orbit. The remainder of the ionopause boundary is from a "best fit" of the aerodynamic ionopause shape of Spreiter and Stahara (1980) to the two OIMS observations. For some orbits, the magnetic field gradients and ion gradients coincide at the ionopause, while in others they do not. As will be shown later, strong magnetic field gradients are not reliable ionopause indicators.

3.2 Model Application--General Characteristics

In this section we identify symbols and parameters which are common to each set of figures (3 per set) used to analyze the PV observations. The first figure of the set (e.g., Figure 3-5) shows the projection of the model magnetic field lines and stability contours on the surface of the planet. The second figure (e.g., Figure 3-6) is an ionospheric cross-section within the plane of the orbit, and finally, the third figure (e.g., Figure 3-7) contains a comparison of the model results with observations.

In the first figure, the magnetic field lines are represented by solid curved lines and the field line spacing is not a measure of magnetic field strength. The region of stability is outlined by a set of dashed lines; the lowest altitude contour is distinguished by shading. The height of each contour is listed on the bottom right hand corner of the figure.

The typical shape of a region of stability is shown in Figure 3-4. As expected, the main region of stability surrounds the magnetic equator. Centered about 50 degrees off the magnetic equator are "finger-like" extensions of the main stable region. The shape and extent of the stable extension regions depends on the relative strength of the various terms making up equation (2.5.2). During periods of enhanced plasma depletion, both the magnetic field strength and magnetic asymmetry factor increase. The change in the

asymmetry factor reduces the angle θ between B and v . Together these two stabilizing effects outweigh the destabilizing effect of the increased plasma flow speed produced by the enhanced plasma depletion mechanism. Therefore, periods of enhanced plasma depletion are characterized by enlarged regions of stability.

Another important feature of the stable region topology is the rapid expansion of its horizontal dimensions with increasing altitudes. Once again two competing factors are at work: the stabilizing effect of decreasing ion density with altitude overcomes the destabilizing effect of increasing plasma flow speed with altitude. The vertical ion density gradient is based on the observations of Brace et al. (1979b), Taylor et al. (1980), and Theis et al. (1980). The vertical plasma velocity gradient is taken from both the ion flow velocity observations of Knudsen et al. (1980) and the model velocity profile computed in Section 2.2. The model treats the mass density as a constant for each horizontal level below the strong ionopause gradients because the statistical results of Theis et al. (1980) show that, on average, the electron density is nearly uniform over a large portion of the dayside ionosphere (SZA: 0 to 60°). Theis et al. (1980) also report little variation of the electron temperature over the same SZA range. Miller et al. (1980) report a similar behavior for the ion densities and temperatures above 200 km. Therefore, it seems reasonable to assume

Figure 3-4. Idealized stable reigon. The ionopause is at 350 km and the levels are separated by 50 km. The stable region widens rapidly with height and is aligned along the magnetic equator with its center about the plasma flow origin. An important feature is the "notch-like" unstable area between the main stable region and the off-axis stable extension region.

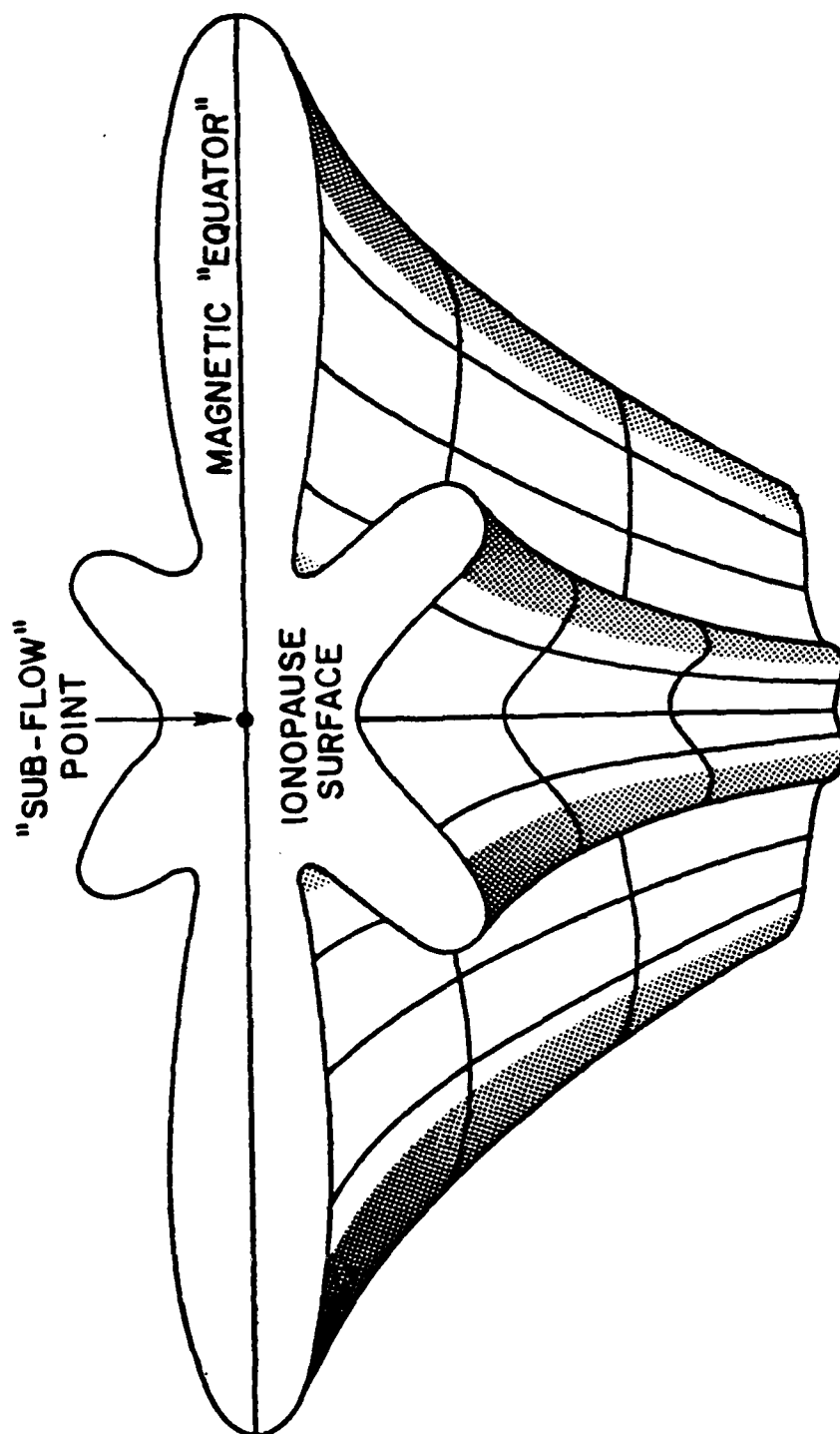


Figure 3-4

that, at high altitudes, there is also little change in the ion flow velocity with SZA because of the weak dayside pressure gradients.

In the first figure of the set (e.g. Figure 3-5), the center of symmetry for the convection pattern is indicated by the small solid circle and the sub-solar point is denoted by the large cross. The PV orbit is shown by the diagonal line; the orbit direction is from the top to the bottom of the figure. The varying thickness of the orbit line is used to distinguish the time spent in the ionosheath (heavy line) from the time the orbiter is within the ionosphere. Once inside the ionosphere, orbital altitudes (in kilometers) are shown by the sidebar, and the ionopause crossings are indicated by the arrows at the edges of the sidebar. The sidebar may conceal a portion of the field lines and/or stability contours.

Within the ionosphere, stable areas encountered by the orbiter are enclosed by a "box." If the boxed region is shaded, it means that the stable area was encountered at (or below) the level of the lower (shaded) stability contour. For example, in Figure 3-5 the first stable area is encountered shortly after the inbound ionopause crossing (~ 350 km). A large unstable region extends from about 250 km inbound to about 250 km outbound; another stable area is encountered just before the outbound ionopause crossing. Figure 3-5 also shows horizontal projections of the observed

magnetic field vectors which are plotted as arrows along the orbit line. The vector projections are shown only for stable ionospheric regions, and for the entire ionosheath region. It is important to remember that the model is only applicable within the ionosphere and therefore, at times, the observed ionosheath magnetic field vectors may not align very well with the model generated ionospheric magnetic field lines.

The second figure in the set (e.g. Figure 3-6) contains contours of constant magnetic field strength within an ionospheric cross-section, taken along the orbital plane. The vertical axis gives the ionospheric height (in kilometers) while the horizontal axis shows the distance from the magnetic equator (in degrees). The horizontal scale is centered at the intersection of the orbital plane with the magnetic equator; positive distance corresponds to distance "above" the magnetic equator and negative distance is "below" the equator. The ionospheric field strength contours (solid lines) are relative to the peak field strength measured at the stagnation point. Ionosheath contours (dashed lines) are modifications of the aerodynamic model of Spreiter et al. (1970) and Spreiter and Stahara (1980). The crossmarks along the orbit show one minute time intervals relative to periapsis; the orbit direction is shown by the solid arrows. The sawtooth pattern outlines the regions of stability within the cross-section plane. For example, in

Figure 3-6, the orbit intersects the region of stability twice. The first intersection is with the stable extension region (see Figure 3-5) which appears as an unattached sawtooth pattern near 30 degrees; the orbit enters this region on its side and exits through the bottom. The second intersection occurs as the orbit crosses the magnetic equator just above 250 km. This central stable region is shaded below 250 km in order to coincide with stability contour shading used in Figure 3-5.

As discussed in Section 3.1, the ionopause altitude is determined from in-situ measurements of the Pioneer-Venus Orbiter Ion Mass Spectrometer (OIMS). The ion data is represented by the asterisks (*) in the top panel of the third figure (e.g. Figure 3-7). Only the atomic oxygen ion data is plotted because it predominates above 200 km (Taylor et al., 1980, 1981). The loss of ion data near periapsis indicates that the orbiter has passed beneath the region of measurable atomic oxygen ion concentration. The arrows below the time axis mark the ionopause locations. The top panel also plots the total observed magnetic field strength versus time; the solid line represents measurements and the dashed line represents the model. The bottom panel shows how the magnetic field direction changes with time. The spike-like field strength features occur within unstable ionospheric regions; they are twisted, narrow magnetic field filaments or "flux ropes" (Russell et al., 1979a,b; Russell

and Elphic, 1979). The field structure within flux-ropes (Elphic et al., 1980a; Wolff et al., 1980) produces the rapid changes of field directions shown in the bottom panel. Notice that the model calculations (dashed line) are shown only for the stable region; model results are omitted for the unstable regions because adding dashed "spikes" would only make the figure more confusing. For example, in Figure 3-7, the model predicts that a large region of instability extends from about -2.5 minutes (end of dashed line) to about 2.1 minutes (start of dashed line).

One final note about terminology: the phrases "convection center," "field pattern center," "current system center," and "sub-flow point" are all synonymous with the phrase "center of symmetry for the convection pattern."

In the following sections, PV orbits 170, 175, 176, 177, 188, and 189 will be analyzed. These orbits were selected because both the ion data (H. A. Taylor, private communication, 1980) and full magnetic vector data (C. T. Russell, private communication, 1980) were available. For all of these orbits, the magnetic field deviation from horizontal is small (R. E. Daniell, private communication, 1980). Orbit 175 will be discussed last because it requires more detailed analysis.

3.3 Analysis of Orbit 170 (Figures 3-5, 3-6, and 3-7)

The IMF direction is east-southeast and the maximum magnetic field strength is 160 gamma. The inbound ionopause crossing is at 370 km (-3.75 minutes) and the outbound crossing is at 350 km (3.6 minutes). Periapsis (186 km) is approximately 35° east of the convection pattern center; the convection pattern center is 15° northwest of the subsolar point. The magnetic field asymmetry factor is 2.0.

Figure 3-5 shows the horizontal projections of the magnetic field and stability contours on the surface of the planet. The stability contours (dashed lines) are: smaller contour (shaded region) outlines the 250 km level, and the larger contour delineates the 350 km level. The orbiter enters an unstable area immediately after the inbound ionopause crossing. A stable region is encountered at about 350 km and it extends down to approximately 275 km where the ionosphere again becomes unstable. The orbiter remains within an unstable ionosphere until it re-enters the stable region at about 270 km (outbound).

Figure 3-6 is a cross-sectional view of how the orbital path intersects the region of stability. The skew in the field strength contours is due to a combination of geometrical effects, the most important being the shape of the horizontal contours of constant magnetic field strength near the magnetic equator (see Figure 4-1). These horizontal contours are nearly parallel to the magnetic equator at large

solar zenith angles. Therefore, the angle at which the orbit intersects the magnetic equator is very important; at small intersection angles the orbital path will nearly parallel these contours, while for large intersection angles the orbit makes nearly a transverse cut across many of the contours. Orbit 170 is somewhere between these two extremes.

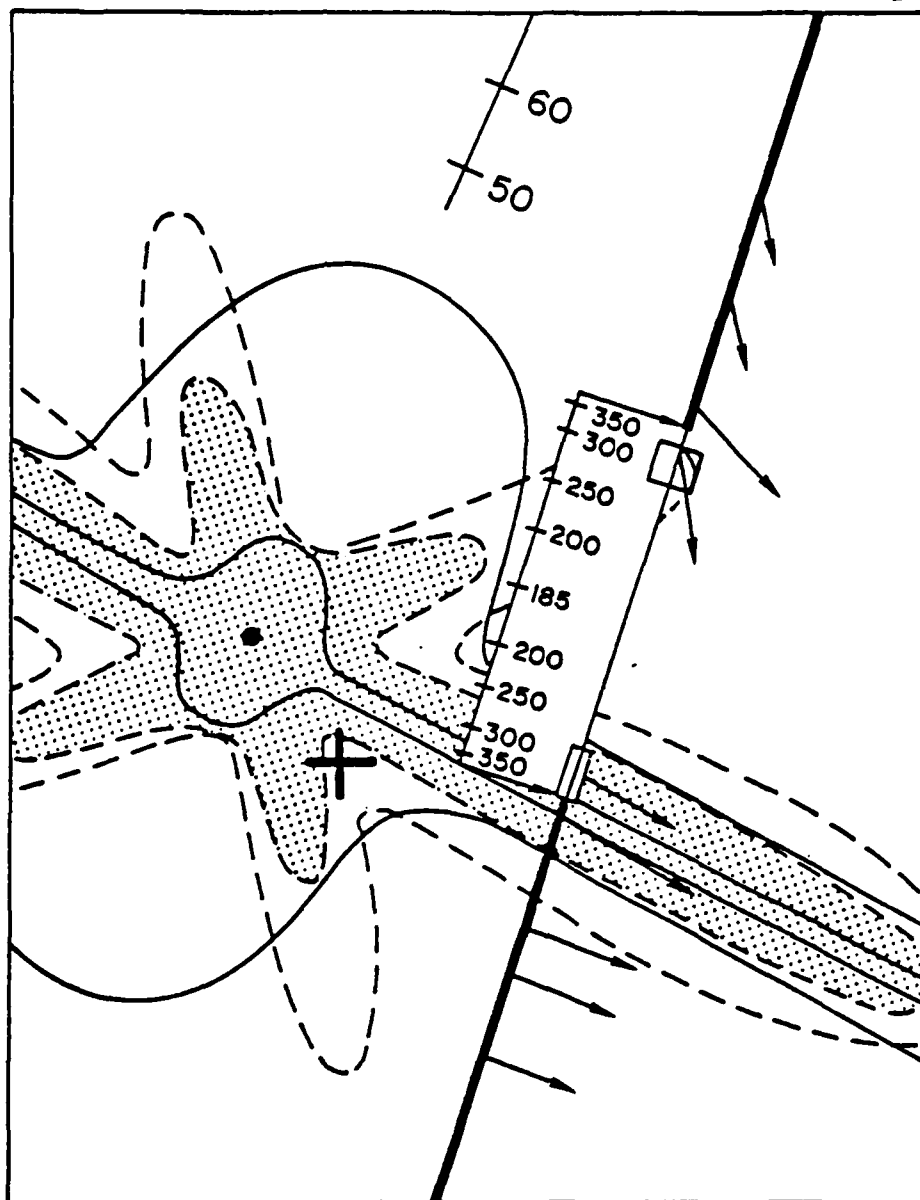
In Figure 3-7, the total magnetic field strength is plotted versus time. As discussed in Section 3.2, the ion data is used to locate the ionopause crossings which are marked by the arrows beneath the time axis. The model field strength (dashed line) agrees well with observations. There is some discrepancy near -3 minutes, but disagreement in this area is not unexpected because the stable region occurs near the point where the field lines have a significant amount of curvature. The field line curvature rate is determined by the local ion gradients which are model inputs. The field lines shown in Figure 3-5 were not finely tuned for Orbit 170. Instead for this orbit--and for all other orbits to follow--we used the closest match from a precomputed library which spans a wide variety of ionospheric conditions. Therefore, a better match for Orbit 170 could be found by appropriate adjustments to the ion gradients. Since our purpose is to show the general applicability of the model, it is not worthwhile to fine tune each orbit. As we will see later, Orbit 170 is one of the poorer

Figure 3-5. Orbit 170--horizontal projection of the magnetic field parameters. The magnetic field lines are represented by the solid curved lines. The dashed lines represent the width of the stable region at two altitudes: the inner contour (shaded) is at 250 km and the outer contour is at 350 km (legend is at bottom of figure). The orbital path is shown by the solid diagonal line; the heavy line indicates that the orbit is outside the ionosphere. The sidebar is used to show the orbital altitude scale within the ionosphere, and the sidebar arrows mark the ionopause crossings. The arrows along the orbit are horizontal projections of the observed magnetic field vectors. Within the ionosphere, the arrows are shown only for the stable regions (outlined by the "boxes"). The solid circle denotes the plasma flow origin and the large cross represents the subsolar point. The scale, at the top of the figure, shows the radial distance, in degrees, from the plasma flow origin. The asymmetry factor is 2.0 and the maximum magnetic field strength is 160 gamma.

ORBIT 170

64

100 GAMMA



SOLID 250 km
DASH 350 km

Figure 3-5

Figure 3-6. Orbit 170--orbital plane cross-section. The ionospheric contours of constant magnetic field strength are shown by the solid lines; the ionosheath contours are given by the dashed lines. The magnitude of each contour is relative to the maximum field strength at the stagnation point (i.e., 0.5 is 50% of the maximum). The ionospheric contours are from the three-dimensional model and the ionosheath contours are modifications of Spreiter's (1970, 1980) aerodynamic model. The sawtooth pattern outlines the stable regions within the cross-section plane; the portion of the stable region below 250 km is shaded. The cross-marks on the orbit are one minute intervals relative to periapsis. The horizontal scale is centered at the intersection of the orbital plane with the magnetic equator; positive distance (in degrees) is above the magnetic equator while negative distance is below the equator

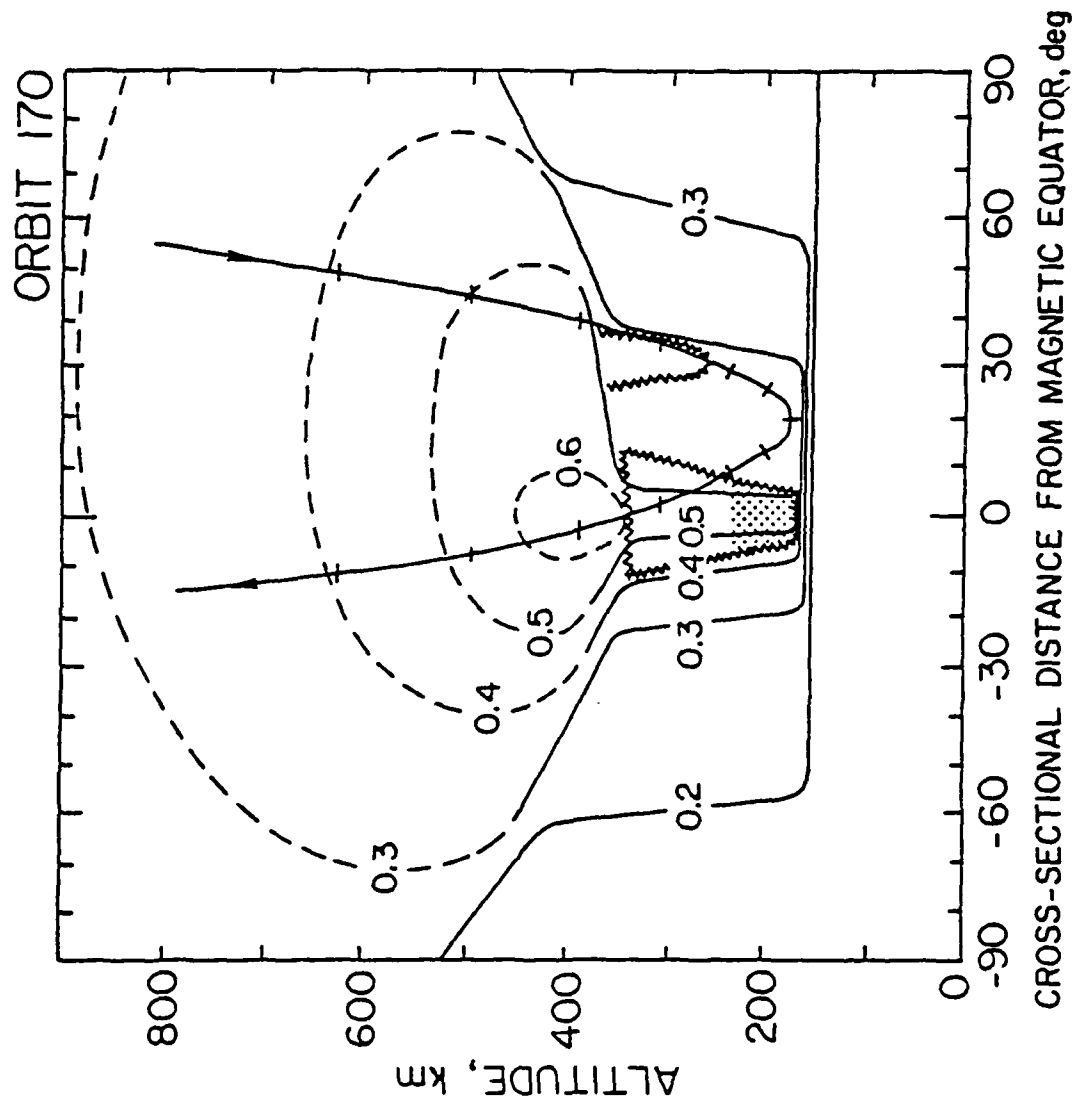


Figure 3-6

Figure 3-7. Orbit 170--comparison of the model with observations. The top panel shows the model field strength (dash line) versus observations; model results are shown only for the stable regions. A break in the dash line designates a region of instability predicted by the model. The field strength scale is in gammas. The "spike-like" field strength features occur whenever the orbiter passes through twisted magnetic filaments ("flux-ropes") which form within the unstable regions. The asterisks (*) are the OIMS measurements of the atomic oxygen ion densities; the density scale is on the far right hand side of the figure. The arrows beneath the time scale mark the ionopause crossings. The time scale is relative to periapsis. The bottom figure shows how the magnetic field direction changes with time; areas of rapid direction changes are characteristic of the turbulence found in the unstable regions. Model results are shown by dash line.

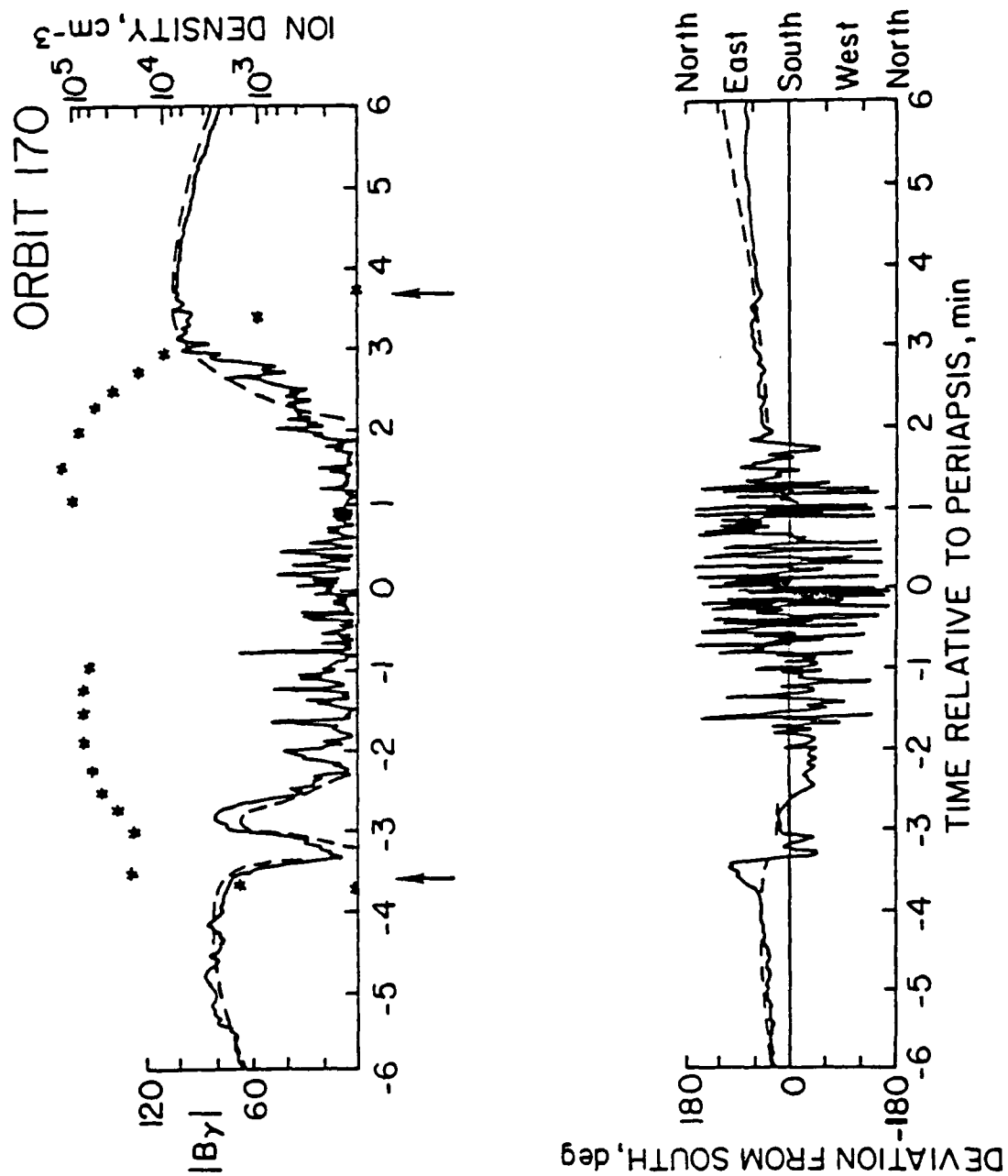


Figure 3-7

matches. Figure 3-7 also shows the deviation from south (direction) for the horizontal component of the magnetic field. As expected, the match is poorest in the ionosheath region since the model field lines are valid only for the ionosphere.

The outbound ionopause crossing for Orbit 170 is not clearly defined. Hartle et al. (1980) report that a superthermal layer of O^+ ions was encountered just above 300 km during the outbound portion of the orbit. These superthermal ions are thought to be due to a non-equilibrium plasma region just above the relatively unperturbed ambient thermal ionosphere (Taylor et al., 1981). Since the ionopause is defined to be the boundary of the thermal ion envelope, the outbound ionopause altitude could be lowered by about 40 km. However, lowering the outbound ionopause would not change the analysis because the only effect would be a reduction in the size of the large stable region just below the outbound ionopause. That is, the model would still predict the existence of stable magnetic fields near 350 km because the ionosheath stagnation region is always assumed to be stable. The ionopause crossing time would change from 3.6 minutes to 3.3 minutes (see Figure 3-7).

3.4 Analysis for Orbit 176 (Figures 3-8, 3-9, and 3-10)

The IMF direction is nearly eastward and the magnetic field maximum is approximately 190 gamma. The inbound ionopause crossing is at 280 km (-3.25 minutes) and the outbound crossing is at 300 km (3.5 minutes). Periapsis (145 km) is approximately 5° west of the convection center; the convection is about 20° northeast of the subsolar point. The magnetic field asymmetry factor is 2.5.

In Figure 3-8 the stability contours are: inner contour is for the 250 km level, and the outer contour outlines the 300 km level. Orbit 176 remains within the stable region for the entire ionospheric transit. A cross-sectional view of the orbital trajectory through the region of stability is shown in Figure 3-9.

The observed field strength, plotted in Figure 3-10, has two areas of data drop out: between 1 and 2 minutes, and then again between 3 and 4 minutes. The PV fluxgate magnetometer has an effective range of ± 128 gamma (Russell, 1980a). The model field strength (dashed line) matches the observations very well. The ion data is again used to identify the ionopause crossings, which are marked by the arrows beneath the time axis. Figure 3-10 also shows a good match between the model field direction and observations.

Figure 3-8. Orbit 176--horizontal projection of the magnetic field parameters. The magnetic field lines are shown by the solid curved lines. The dashed lines represent the width of the stable region at two altitudes: the inner contour (shaded) is at 250 km and the outer contour is at 300 km (legend is at bottom of figure). Within the ionosphere, the stable region is enclosed by a "box"; the shaded portion of the box indicates that this area is at, or below, the 250 km level. The arrows along the orbit are horizontal projections of the observed magnetic field vectors. The scale in the upper right hand corner of the figure is the radial distance, in degrees, from the plasma flow (solid circle). The cross identifies the subsolar point. The asymmetry factor is 2.5 and the maximum field strength is 190 gamma.

ORBIT 176

72

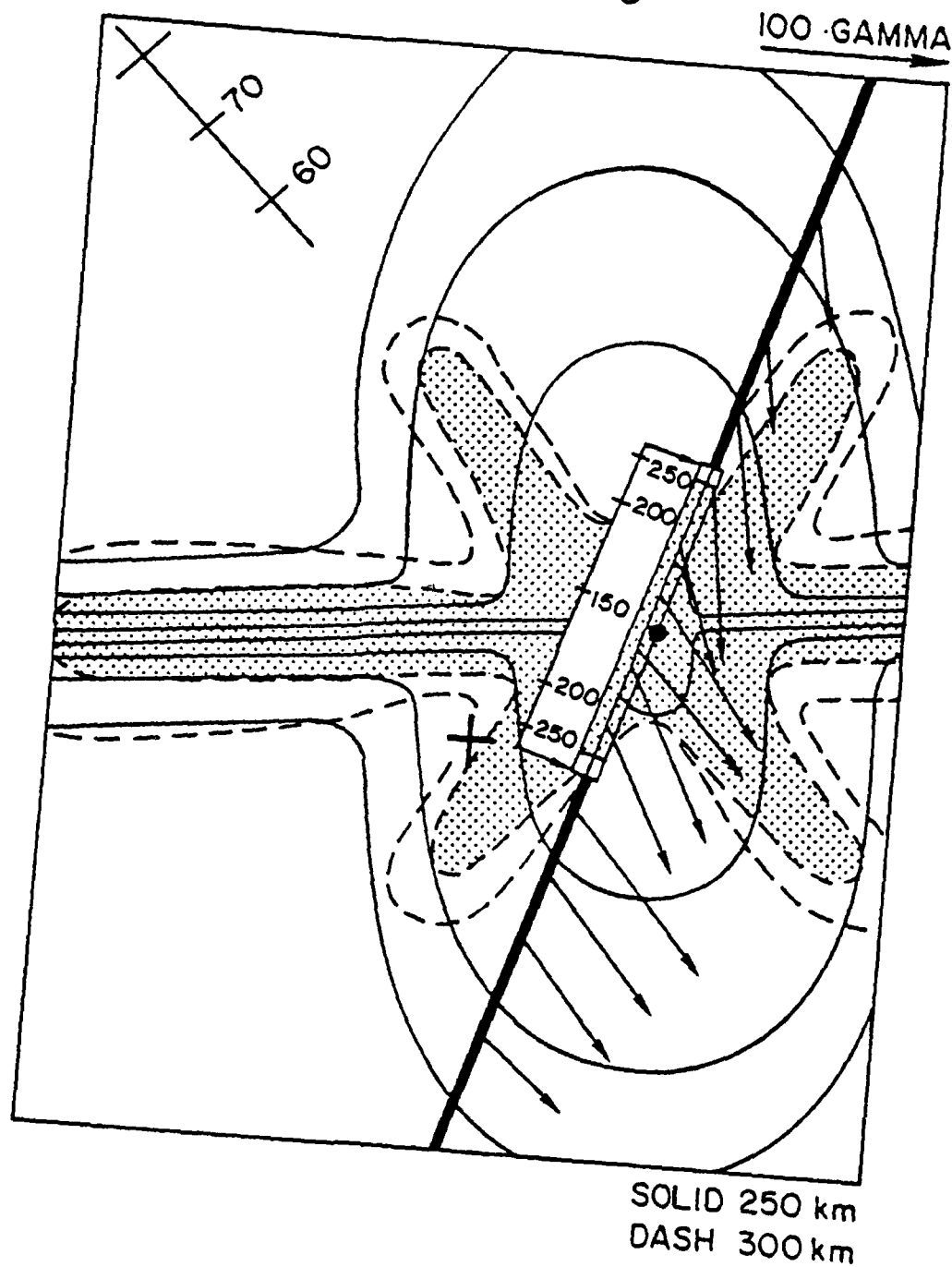


Figure 3-8

Figure 3-9. Orbit 176--orbital plane cross-section. The ionospheric contours of constant magnetic field strength (solid lines) are from the three-dimensional model and the ionosheath contours (dash lines) are modifications of Spreiter's aerodynamic model. The field strength magnitudes are relative to the stagnation point maximum. The sawtooth pattern outlines the stable region within the orbital plane; the portion of the stable region below 250 km is shaded. The cross-marks on the orbit are one minute intervals relative to periapsis. The horizontal scale is centered at the intersection of the orbital plane with the magnetic equator; positive distance (in degrees) is above the magnetic equator and negative distance is below the equator.

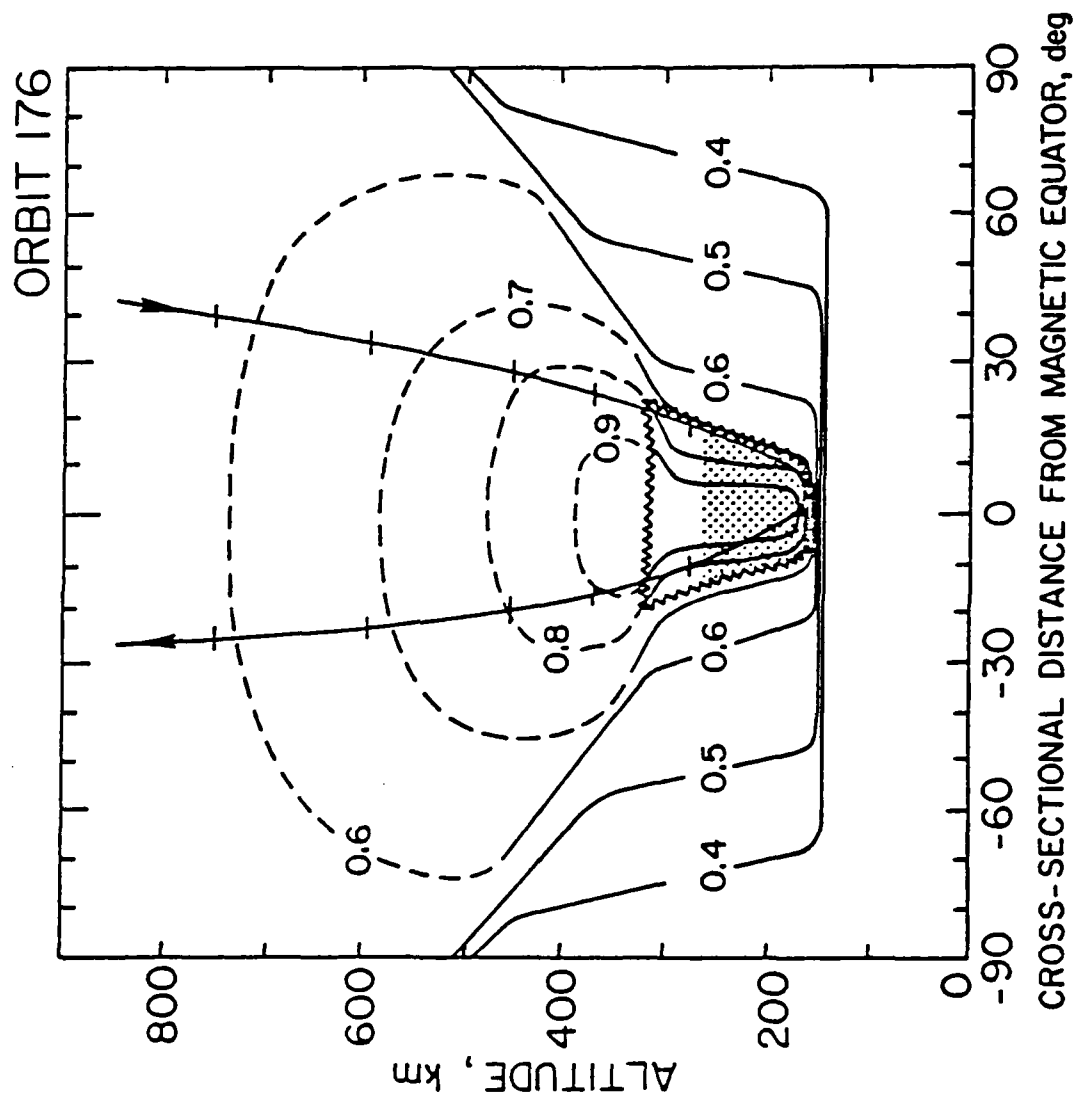


Figure 3-9

Figure 3-10. Orbit 176--comparison of model with observations. The top figure compares model field strength (dash line) with observations; the field strength scale is in gammas. The asterisks (*) are the OIMS measurements of the atomic oxygen ion densities; the density scale is on the far right hand side of the figure. The arrows beneath the time scale mark the ionopause crossings. Time is relative to periapsis: negative time is pre-periapsis and positive time is post-periapsis. The bottom figure shows the magnetic field direction changes with time; model results are given by dash line.

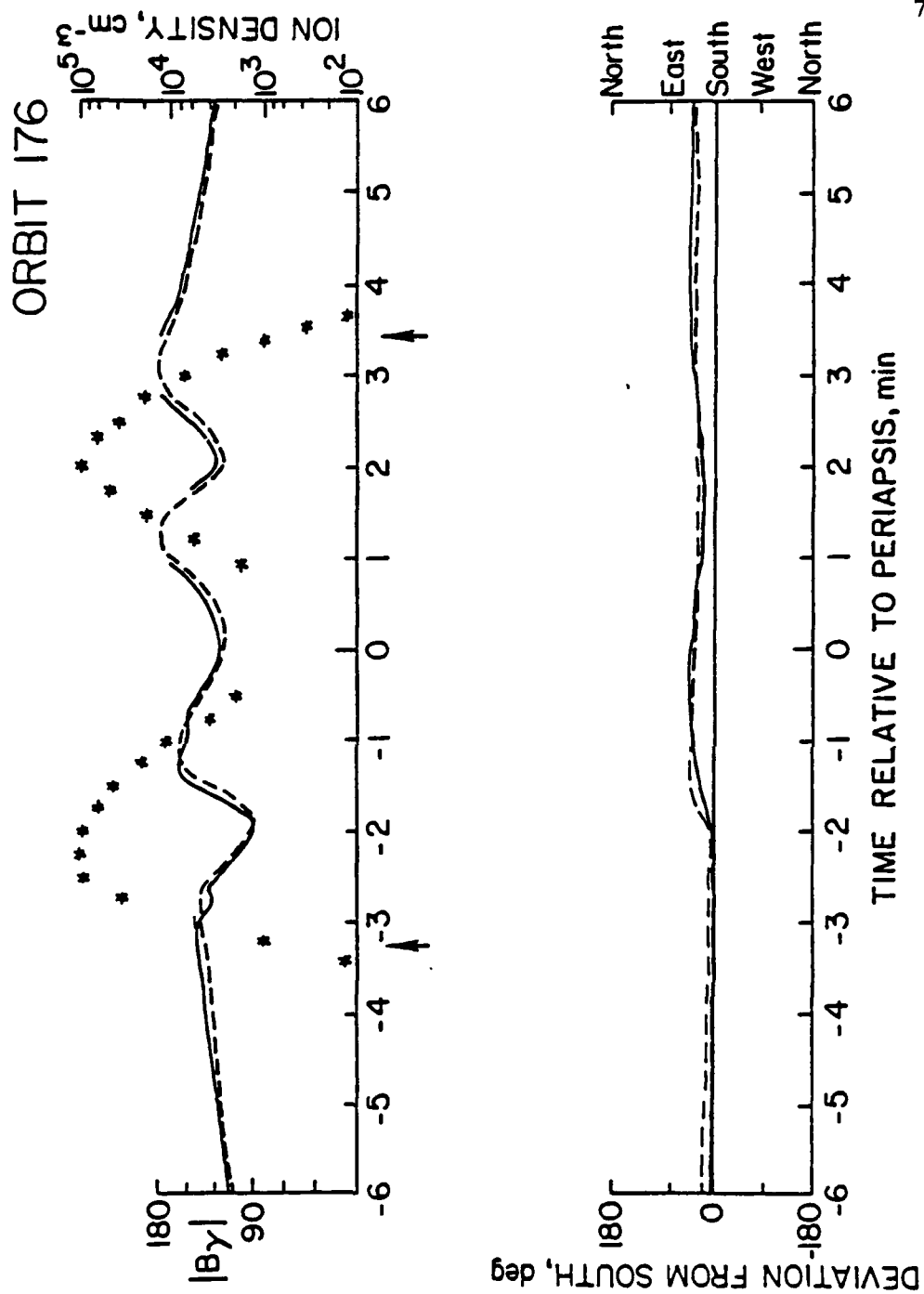


Figure 3-10

3.5 Analysis of Orbit 177 (Figures 3-11, 3-12, and 3-13)

The IMF direction is northeast and the maximum magnetic field strength is 110 gamma. The inbound ionopause crossing is at 350 km (-4 minutes) and the outbound crossing is also at 350 km (4 minutes). Periapsis (150 km) is about 5° west of the convection pattern center and the convection center is approximately 20° northeast of the subsolar point. The magnetic field asymmetry factor is 1.5.

As seen in Figure 3-11, the orbiter enters the stable region immediately after the inbound ionopause crossing; the stable region extends for about 100 km (~ 1 minute). The orbiter then enters an unstable area which extends down to about an altitude of 200 km, where again the orbiter enters the region of stability. This pattern is closely duplicated during the outbound portion of the orbit.

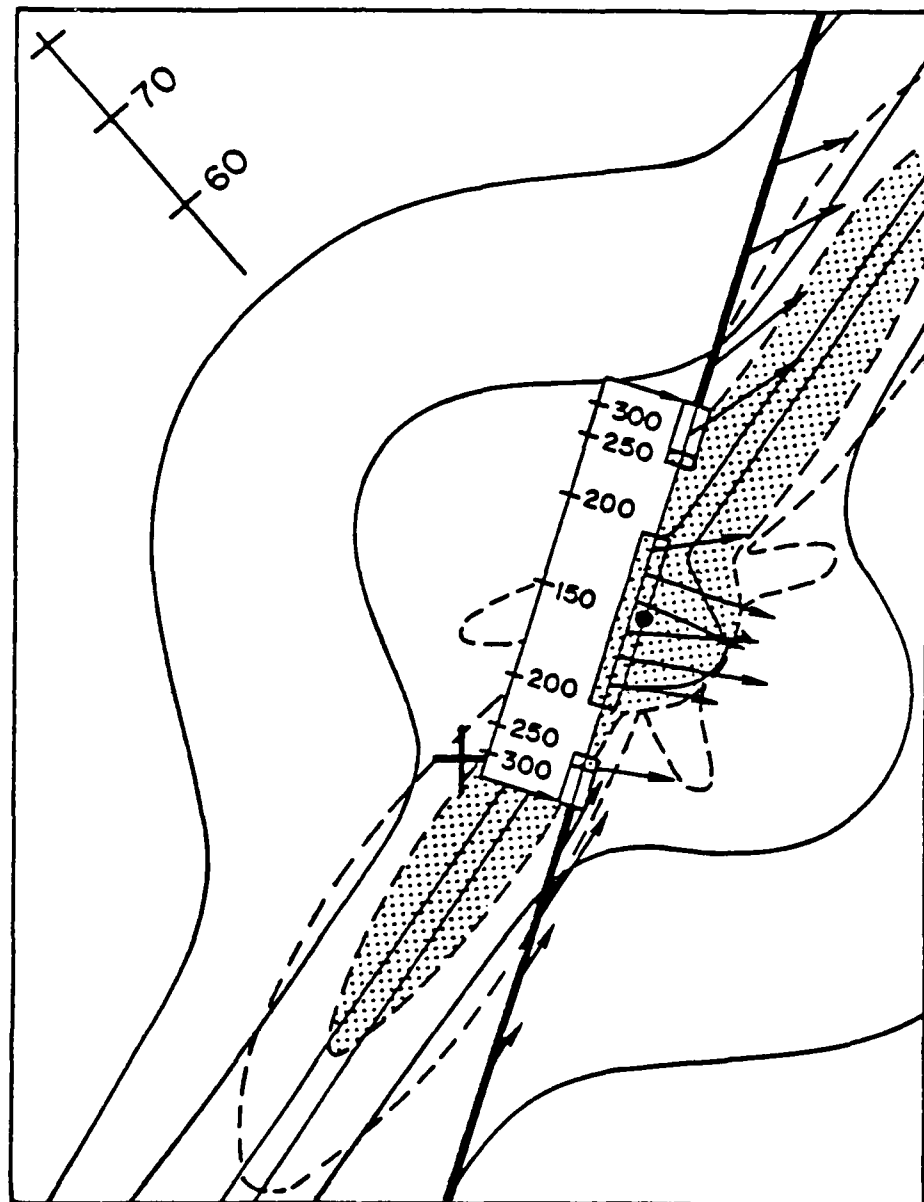
The topology of the stable region is more apparent in Figure 3-12. As discussed in Section 3.2, the stable region is characterized by rapid broadening at high altitudes and it is this "ledge-like" protrusion that Orbit 177 encounters at both ionopause crossings. Once again, Figure 3-13 shows that the model agrees well with both the measurements of field magnitude and direction within the ionosphere. The ionopause crossings are indicated by the arrows beneath the time axis.

Figure 3-11. Orbit 177--horizontal projection of magnetic field parameters. The magnetic field lines are shown by the solid curved lines. The dash lines represent the width of the stable region at two altitudes: the inner contour (shaded) is at 250 km and the outer contour is at 350 km (legend at bottom of figure). The sidebar shows the orbital altitude within the ionosphere; the sidebar arrows mark the ionopause crossings. Within the ionosphere, stable regions are enclosed by a "box"; the shaded portion of the box indicates that this area is at or below the 250 km level. The arrows along the orbit line are the observed magnetic field vector. Within the ionosphere, the vectors only appear in the stable regions. The scale in the upper right hand corner of the figure is the radial distance, in degrees, from the plasma flow origin (solid circles). The cross designates the subsolar point. The asymmetry factor is 1.5, and the maximum field strength is 110 gamma.

ORBIT 177

79

100 GAMMA →



SOLID 250 km
DASH 300 km

Figure 3-11

Figure 3-12. Orbit 177--orbital plane cross-section. The ionospheric contour of constant magnetic field strength (solid lines) are from the three-dimensional model and the ionosheath contours (dash line) are modifications of Spreiter's aerodynamic model. The field strength magnitudes are relative to the stagnation point maximum. The sawtooth pattern outlines the stable region within the orbital plane; the shaded portion is below 250 km. The horizontal scale is centered at the intersection of the orbital plane with the magnetic equator. Positive distance (in degrees) is above the magnetic equator, and negative distance is below the equator.

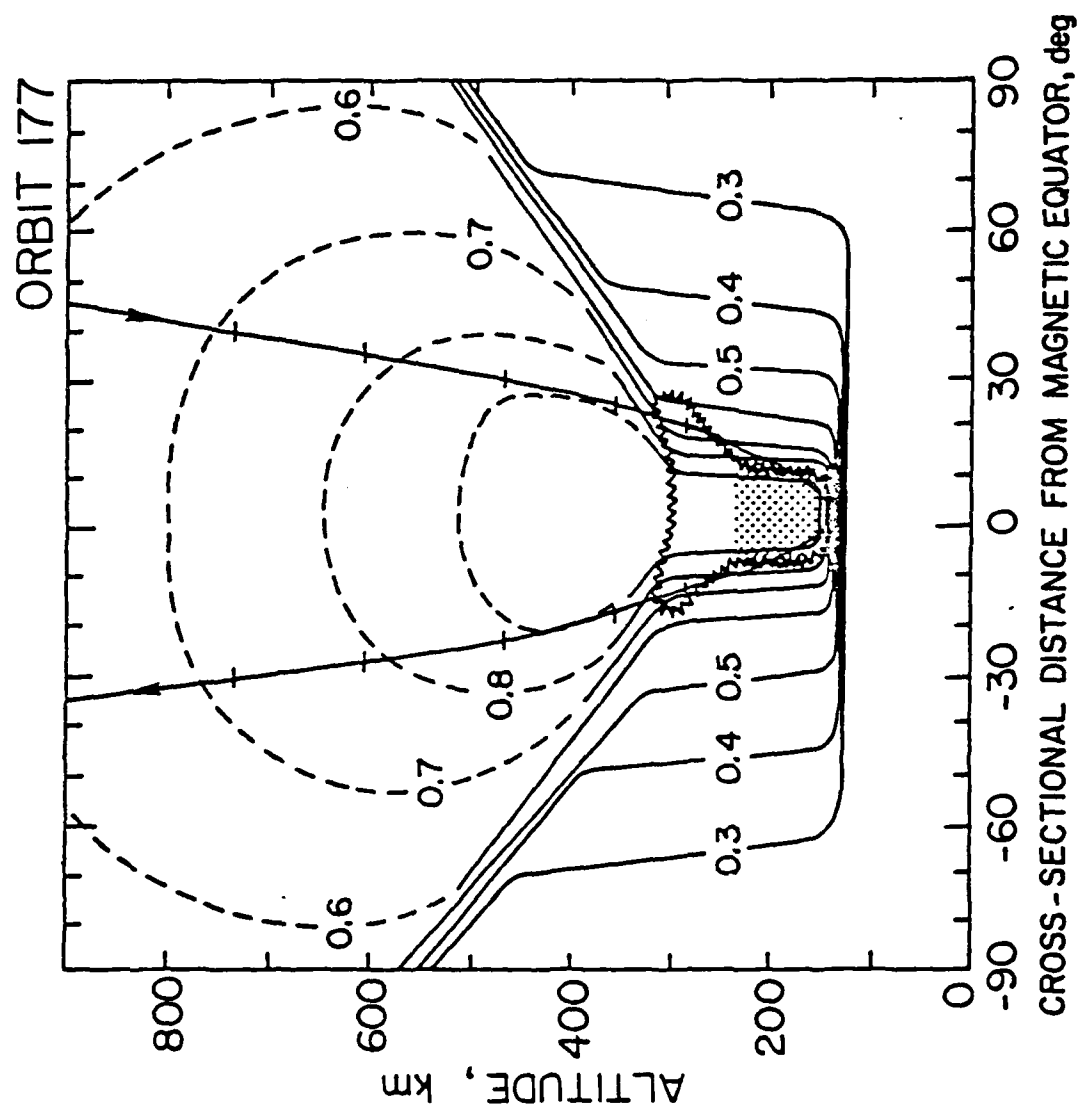


Figure 3-12

Figure 3-13. Orbit 177--comparison of model with observation. The top figure shows the model field strength (dash line) versus observations; model results are shown only for the stable regions. A break in the dash line designates a region of instability predicted by the model. The field strength scale is in gammas. The "spike-like" field strength features occur whenever the orbiter passes through twisted magnetic field filaments ("flux-ropes") which form in the unstable regions. The asterisks (*) are the OIMS measurements of the atomic oxygen ion densities. The arrows beneath the time scale mark the ionopause crossings. The bottom figure shows how the magnetic field direction changes with time; areas of rapid direction changes are characteristic of the turbulence found in the unstable regions. Model results are shown by the dash line.

AD-A116 692

AIR FORCE INST OF TECH WRIGHT-PATTERSON AFB OH
A THREE DIMENSIONAL MODEL OF THE PLASMA FLOW AND MAGNETIC FIELD--ETC(U)
MAR 82 T F TASCIONE

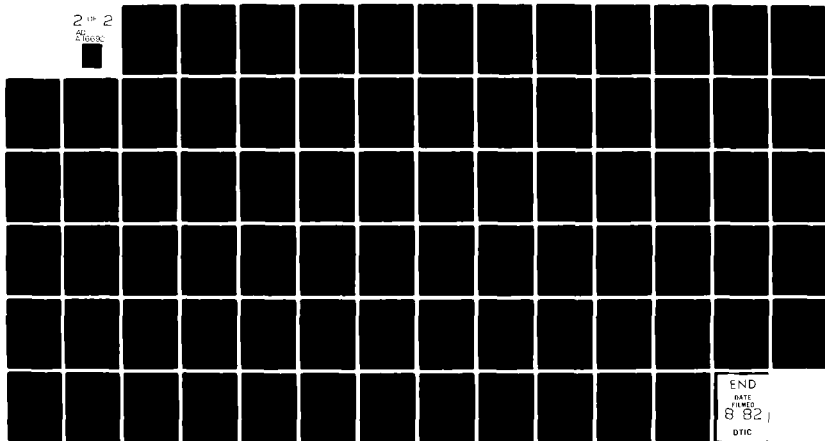
F/G 20/9

UNCLASSIFIED

AFIT/NR/82-16D

NL

2 1/2 2
2 1/2 2



END
DATE
FILMED
8 82
DTIC

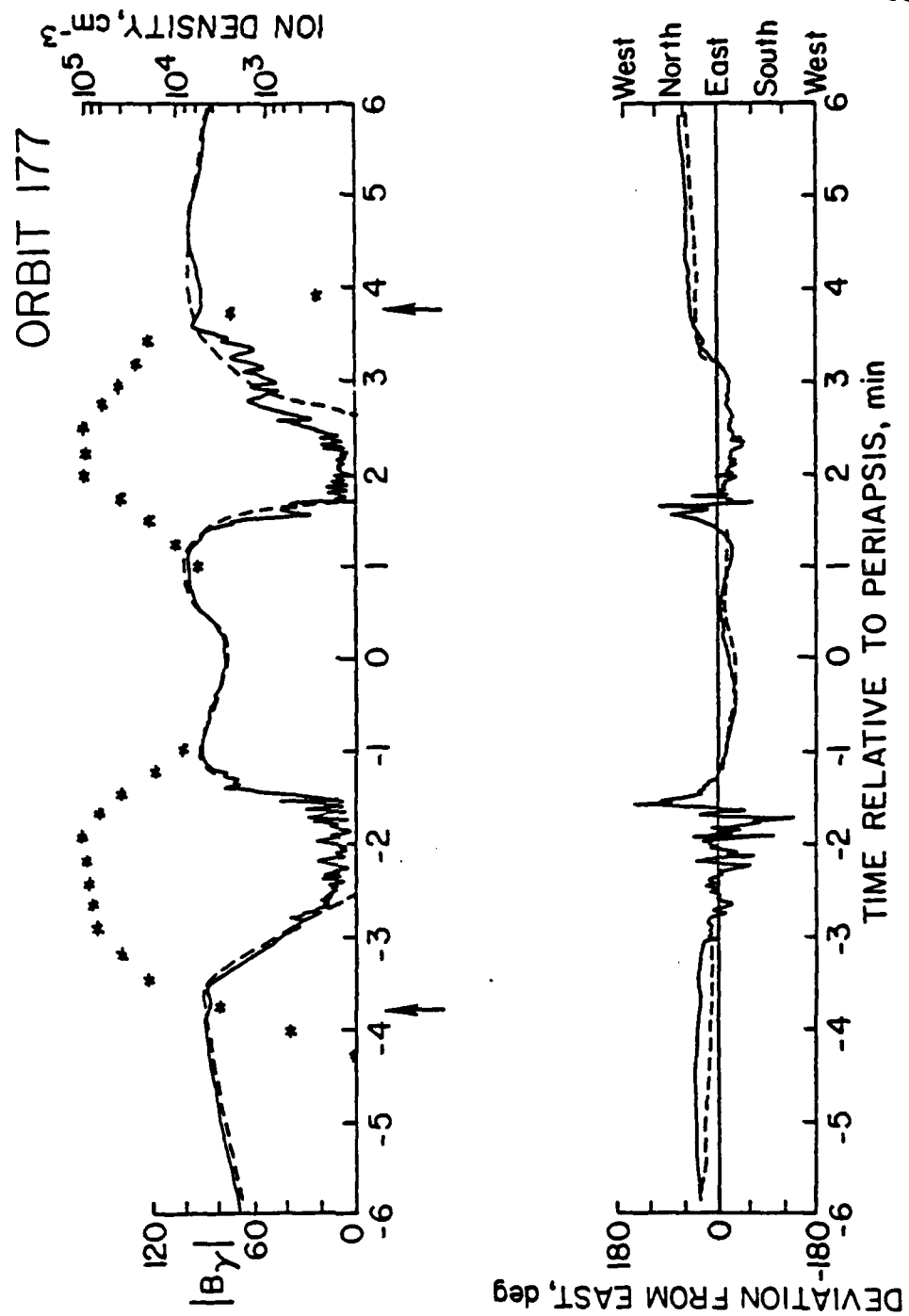


Figure 3-13

3.6 Analysis for Orbit 188 (Figures 3-14, 3-15, and 3-16)

This orbit is particularly interesting because the orbiter encounters an entirely unstable ionosphere. The IMF direction is southeast and the maximum magnetic field strength is 110 gamma. The inbound ionopause crossing is at 370 km (-4 minutes) and the outbound crossing is at 280 km (3 minutes). Periapsis (168 km) is approximately 26° north-east of the convection pattern center and the convection center is about 14° southwest of the subsolar point. The magnetic field asymmetry factor is 1.5.

As seen in Figure 3-14, the orbiter remains in an unstable portion of the ionosphere during the entire ionospheric passage; the outbound ionopause crossing occurs before the orbiter enters the stable region which encircles the convection center. The relative position of the orbital path versus the region of stability is more apparent in Figure 3-15. As in all the previous figures, the OIMS measurements are used to determine the ionopause locations. However, the inbound ionopause crossing for Orbit 188 is not clearly defined and could be higher than the 370 km used in the analysis. The uncertainty is due to a high altitude superthermal component of the O^+ ions.

As seen in Figure 3-16, the model field strength and direction agree very well with observations. The model predicts that the unstable region extends from approximately -3.5 minutes to about 2.5 minutes, which again agrees with

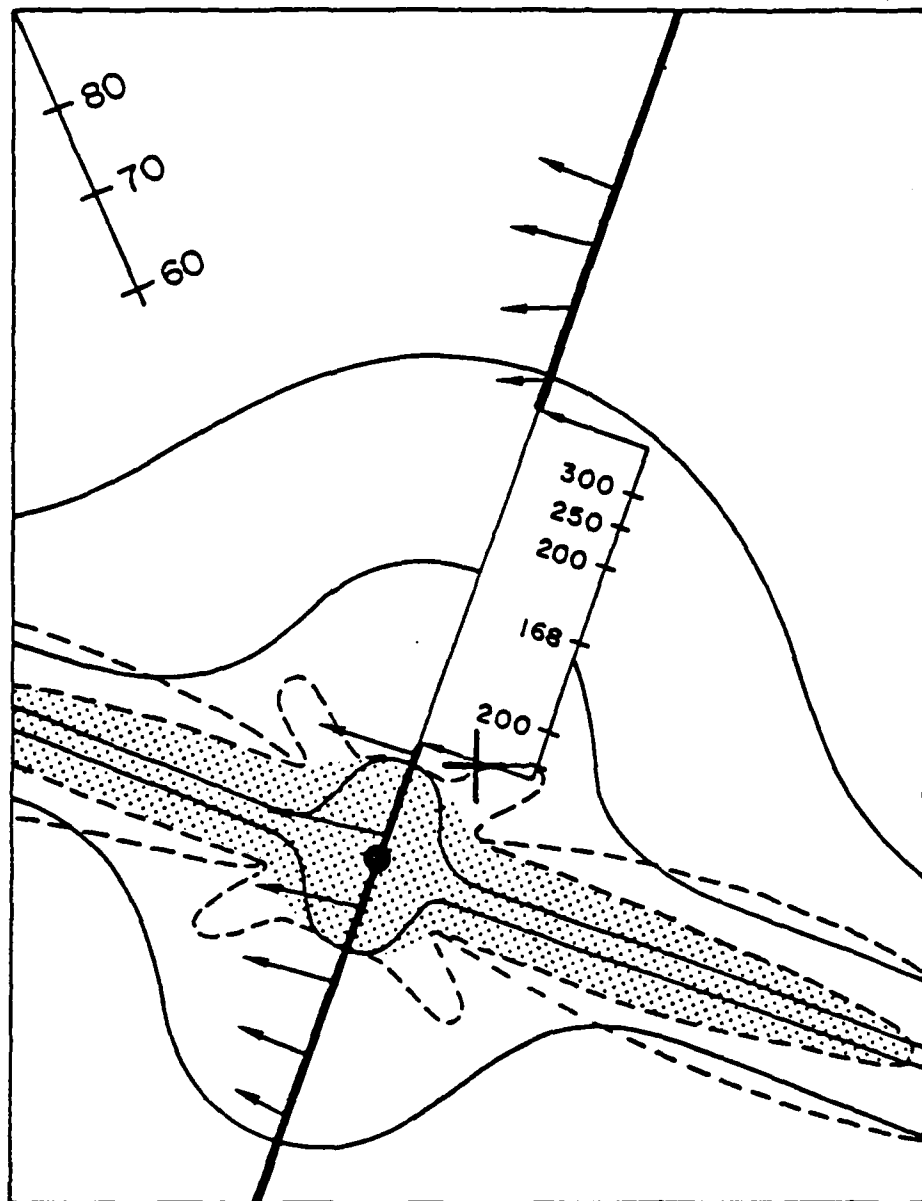
observations. In the lower panel of Figure 3-16 there appears to be a stable region near -2.5 minutes (i.e., steady field direction) which would disagree with the model predictions. However, the field direction information is only part of the available data; the upper panel of Figure 3-16 shows that at -2.5 minutes the field strength signature is characteristic of an unstable region. This supports the model's contention that during this time, the orbit was within a region of instability.

Figure 3-14. Orbit 188--horizontal projection of the magnetic field parameters. The magnetic field lines are shown by the solid curved lines. The dash lines represent the width of the stable region at two altitudes: the inner contour (shaded) is at 250 km and the outer contour is at 300 km (legend is given at bottom of figure). The sidebar shows the orbital altitude within the ionosphere; the sidebar arrows mark the ionopause crossings. The arrows along the orbit line are the observed magnetic field vectors. Since the ionosphere is totally unstable, these vectors are shown only for the ionosheath (heavy line). The scale in the upper right hand corner of the figure is the radial distance, in degrees, from the plasma flow origin (solid circles). The cross designates the subsolar point. The asymmetry factor is 1.5, and the stagnation point field strength is 110 gamma.

ORBIT 188

87

100 GAMMA



SOLID 250 km
DASH 300 km

Figure 3-14

Figure 3-15. Orbit 188--orbital plane cross-section. The ionospheric contours of constant magnetic field strength (solid lines) are from the three-dimensional model and the ionosheath contours (dash line) are modifications of Spreiter's aerodynamic model. The field strength magnitudes are relative to the stagnation point maximum. The sawtooth pattern outlines the stable region within the orbital plane; the shaded portion is below 250 km. The horizontal scale is centered at the intersection of the orbital plane with the magnetic equator.

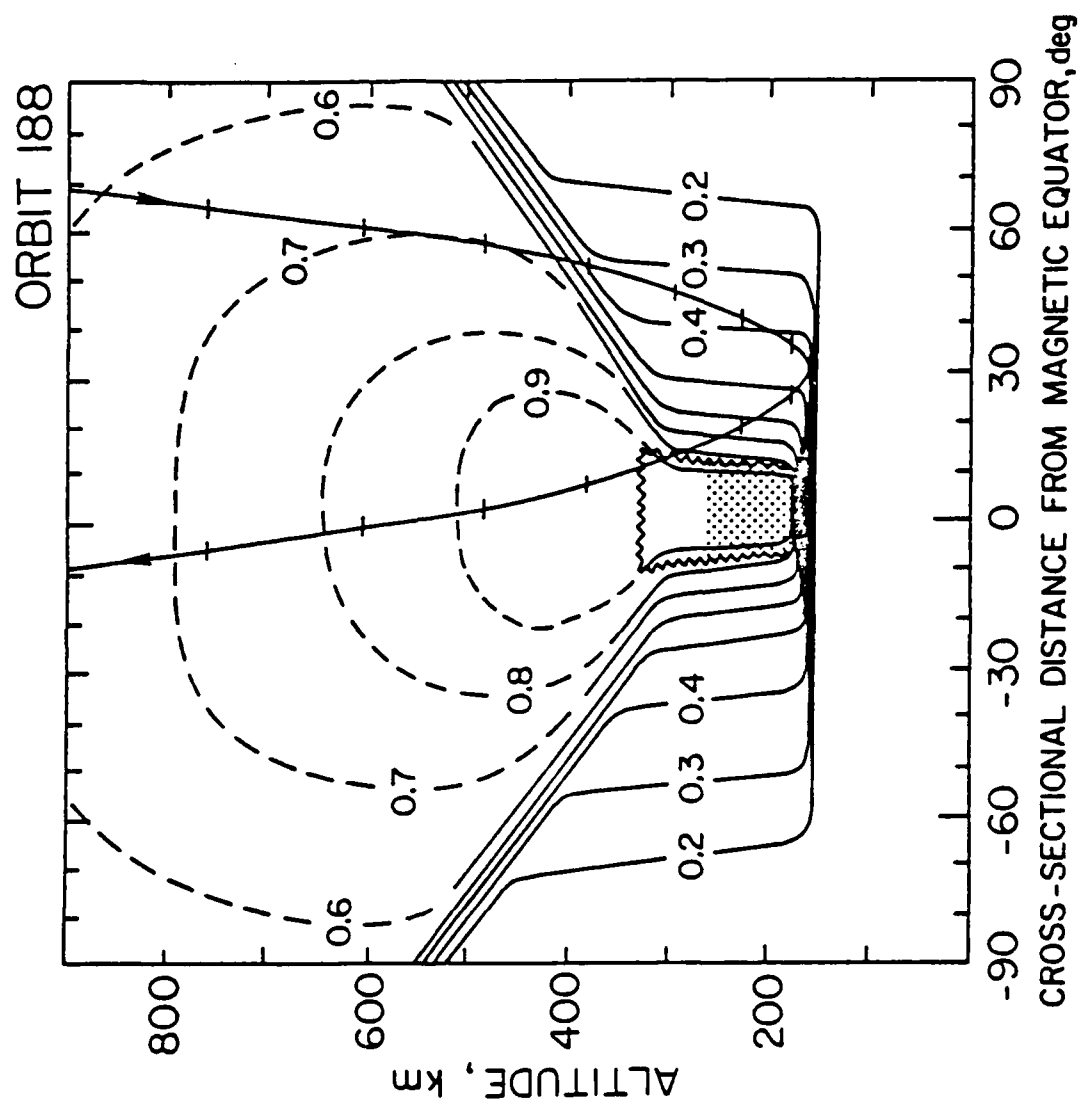


Figure 3-15

Figure 3-16. Orbit 188--comparison of model with observations. The top figure shows the modeled field strength (dash line) versus observations; model results are shown only for the stable regions. A break in the dash line designates a region of instability predicted by the model. The field strength scale is in gammas. The "spike-like" field strength features occur whenever the orbiter passes through twisted magnetic field filaments ("flux-ropes") which form in the unstable regions. The asterisks (*) are the OIMS measurements of the atomic oxygen ion densities. The arrows beneath the time scale mark the ionopause crossings. The bottom figure shows how the magnetic field direction changes with time; rapid direction changes are characteristic of the turbulence found in the unstable regions. The model results are shown by the dash line.

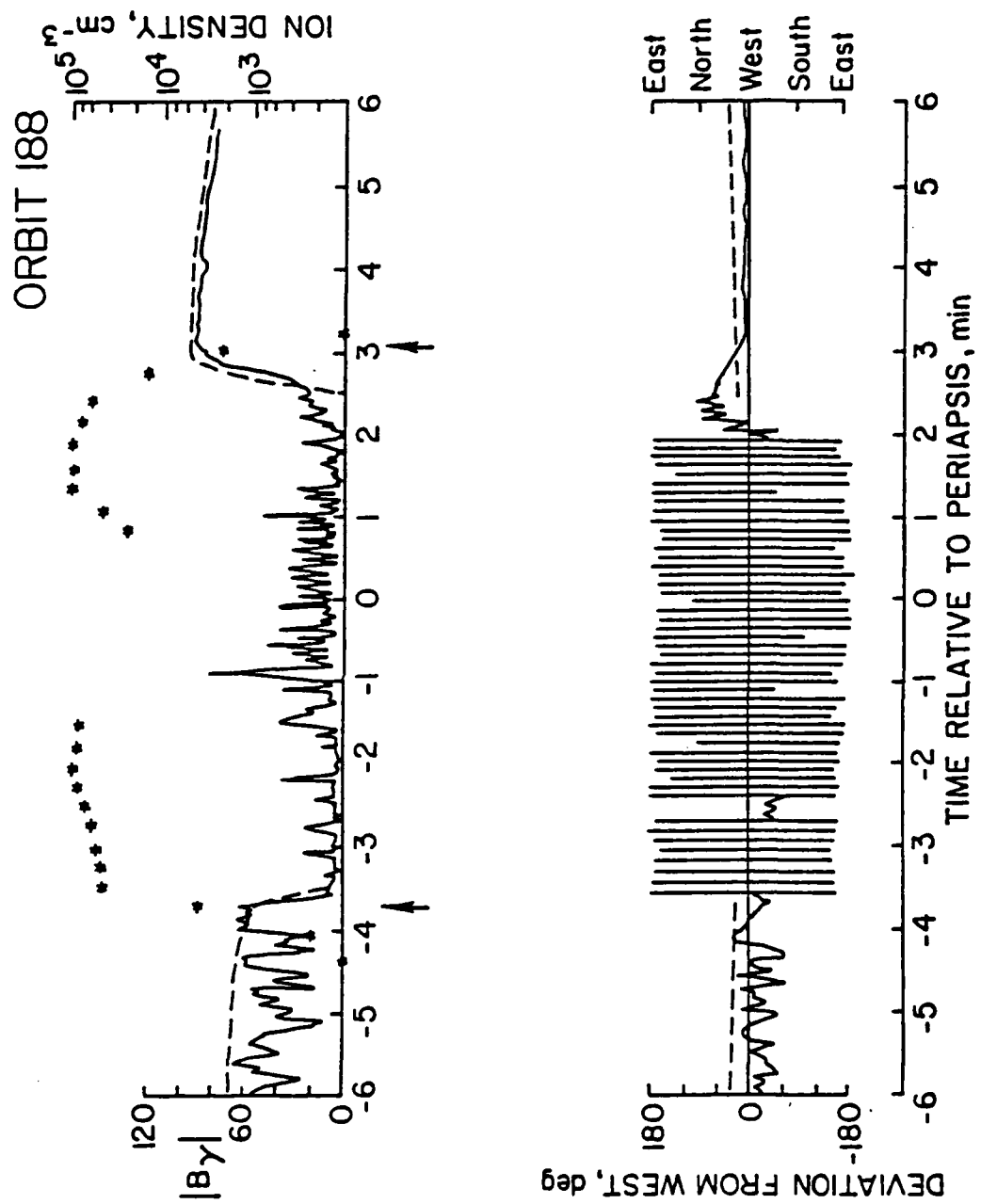


Figure 3-16

3.7 Analysis for Orbit 189 (Figures 3-17, 3-18, and 3-19)

The IMF direction is nearly northward and the maximum field strength is 140 gamma. The inbound ionopause crossing is at 550 km (-5.7 minutes) and the outbound ionopause crossing is at 330 km (3.5 minutes). Periapsis (170 km) is approximately 30° northeast of the convection pattern center and the convection center is 10° southwest of the subsolar point. The asymmetry factor is 2.0.

The relatively high inbound ionopause crossing and the lower outbound ionopause crossing is consistent with the orbiter entering the ionosphere relatively far from the convection center and exiting near the convection pattern center. In the model, the inbound ionopause crossing is about 32° from the convection center, and the outbound ionopause crossing is within 10° of the convection center. The orbiter enters an unstable area almost immediately after the inbound ionopause crossing and remains within the unstable area until it just grazes the edge of the main region of stability at about -4 minutes (370 km). There is some uncertainty about how long the orbiter remains within the stable region because, at high altitudes, the model is very sensitive to small changes in the orbit orientation relative to the stable region geometry. That is, the horizontal width of the stable region changes dramatically with altitude (see Section 3.2) and therefore, for grazing intersection, small shifts in the orbit's position relative to the region of

stability can drastically change the transit time through the region of stability. In Figure 3-17, the field (and stable region) is oriented so as to give the best fit with observations. Within the orbital cross-section plane (see Figure 3-18), this stable region would appear as a thin, irregular ellipsoid bordering the orbit line from approximately -4 minutes to about -3.5 minutes. In the scale of Figure 3-18, this small ellipsoid would be slightly wider than the orbit line and therefore, it is omitted for the sake of clarity.

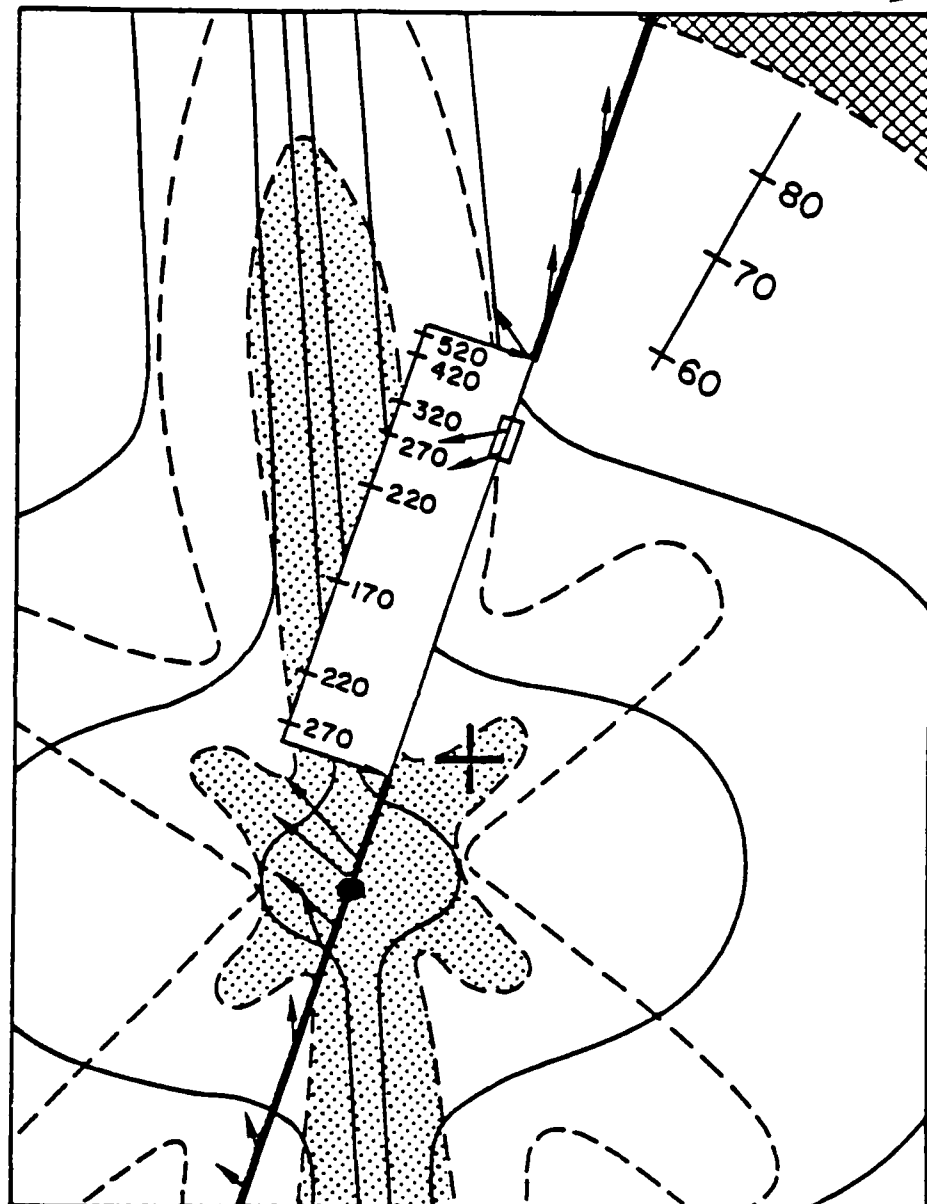
As seen in Figure 3-19, the model overestimates the field strength at the outbound ionopause crossing. Considering that the ionosheath model (Spreiter et al., 1970; Spreiter and Stahara, 1980) was simply grafted onto the ionospheric model, it is not surprising that, occasionally, spurious magnetic field strength magnitudes occur near the ionopause boundary. The biggest field direction discrepancy occurs at -4 minutes where the field lines have a large curvature. As discussed earlier (Section 3.3), "fine-tuning" model inputs could improve the match.

Figure 3-17. Orbit 189--horizontal projection of the magnetic field parameters. The magnetic field lines are shown by the solid curved lines. The dash lines represent the width of the stable regions at two altitudes: the inner contour (shaded) is at 250 km and the outer contour is at 450 km (legend is at bottom of figure). The sidebar shows the orbital altitude within the ionosphere; the sidebar arrows mark the ionopause crossings. The stable region within the ionosphere is enclosed by a "box"; the stable region starts at about 370 km and extends down to about 320 m. The arrows along the orbit line are the observed magnetic field vectors; within the ionosphere, the vectors appear only in the stable region. The scale in the upper right hand corner of the figure is the radial distance, in degrees, from the plasma flow origin (solid circles). The crosshatch area, in the upper right hand corner, designates the boundary of the planetary disk. The cross denotes the subsolar point. The asymmetry factor is 2.0, and the maximum field strength is 140 gamma.

ORBIT 189

95

100 GAMMA



SOLID 250 km
DASH 450 km

Figure 3-17

Figure 3-18. Orbit 189--orbital plane cross-section. The contour of constant magnetic field strength within the ionosphere are shown by the solid lines; ionosheath contours are given by dash lines. The field strength magnitudes are relative to the stagnation point maximum. The sawtooth pattern outlines the stable region surrounding the plasma flow origin. The stable region encountered during inbound is omitted for simplicity (see text). The horizontal scale is centered at the intersection of the orbital plane with the magnetic equator.

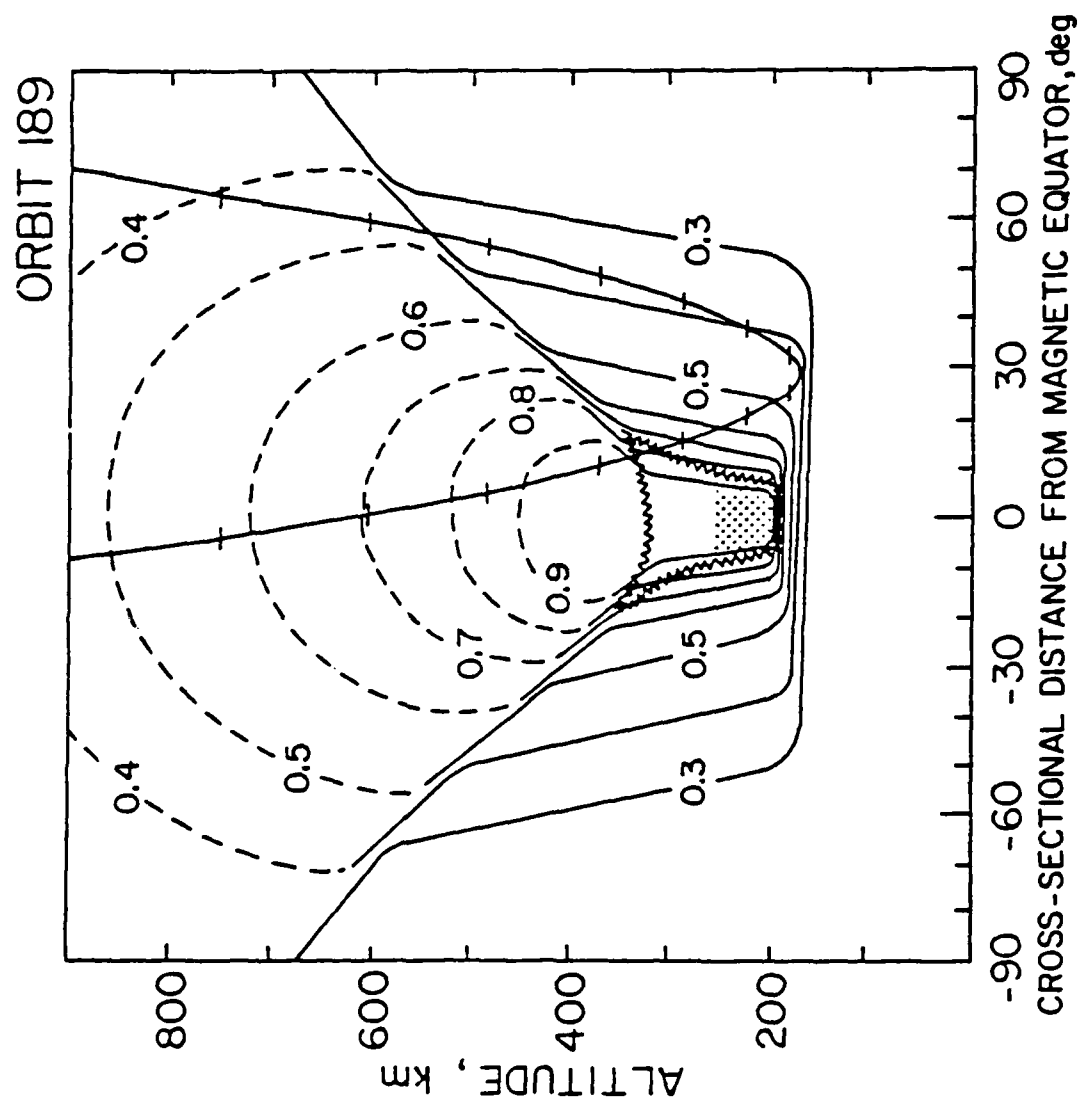


Figure 3-18

Figure 3-19. Orbit 189--comparison of model with observation. Model results (dash line) are shown only for the stable regions. A break in the dash line designates a region of instability predicted by the model. The field strength scale is in gammas. The "spike-like" field strength features occur whenever the orbiter passes through twisted magnetic field filaments ("fluxropes") which form in the unstable regions. The asterisks (*) are the OIMS measurements of the atomic oxygen ion densities. The arrows beneath the time scale mark the ionopause crossings. Regions of rapid direction changes are characteristic of the turbulence found in the unstable regions.

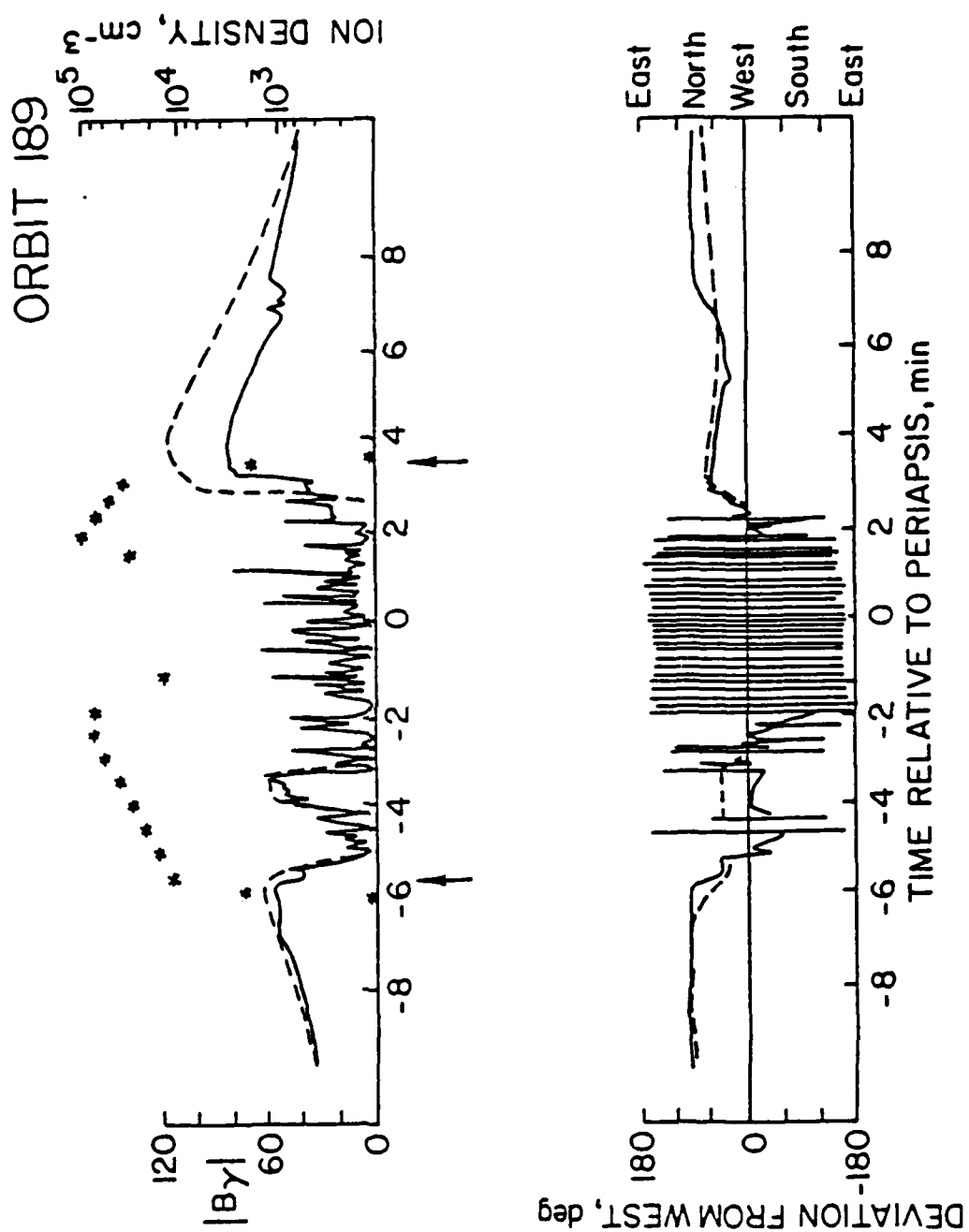


Figure 3-19

3.8 Analysis for Orbit 175 (Figures 3-20, 3-21, 3-22, 3-23, and 3-24)

During this orbit, the IMF appears to be undergoing a slow rotation. This interpretation is based on the following facts. First, Orbit 175 is the only orbit where the IMF direction after the ionospheric exit does not return to the pre-ionospheric transit conditions (compare Figure 3-24 with Figures 3-7, 3-10, 3-13, 3-16, and 3-19). Secondly, the inbound ionopause crossing occurs nearly 2 minutes before the appearance of strong magnetic field gradients. This in itself is not unusual, but taken with the observed field direction and the location of the region of stability, it becomes impossible to match the observations with a single static model representation. An IMF rotation rate of about 2.5° per minute is required for the model to match the observations; this rotation rate is compatible with in-situ observations (Brandt, 1970; Hundhausen, 1972). It may be that the rotation is unnecessary because the model might not be applicable for Orbit 175. However, considering the model's success with all the other orbits, we will pursue the idea that the IMF is rotating.

The model assumes that both the ionospheric magnetic fields and plasma flow are strictly horizontal. Observations indicate that for Orbit 175, the magnetic field remained horizontal during the entire orbiter transit. However, the rotating magnetic field will induce an electric

field which can accelerate ions to speeds comparable to the ambient flow speed, a non-ignorable effect. If "frozen-in" flux conditions exist in the ionosheath region, then this additional plasma acceleration increases the plasma flow speed perpendicular to the local ionosheath magnetic field. The net affect is an increase in both the plasma flow and magnetic field asymmetry factors. The analysis assumes that the plasma depletion mechanism is unaffected by the magnetic field rotation.

The inbound ionopause crossing is at about 450 km (-4.8 min) and the outbound ionopause crossing is at approximately 300 km (3.5 min). Periapsis (148 km) is nearly 25° north of the convection pattern center and the convection center is about 20° east-southeast of the subsolar point. The convection center remains fixed during the rotation. The maximum field strength is 160 gamma and the magnetic field asymmetry factor is 2.0.

Figures 3-20, 3-21, and 3-22 show the model analysis at 6 minute intervals during the rotation. Each figure is an average representation for the altitude range shown in brackets on the right hand side of the figure. For example, Figure 3-20 is an average representation for the altitude range of 450 to 300 km. As usual, a sidebar is used to show the altitude scale within the ionosphere. Figure 3-21 covers the altitude range of 250 to 148 km; no magnetic field vectors are shown because the ionosphere is unstable

over this altitude range. The outbound magnetic field configuration is shown in Figure 3-22. In this figure, the orbit remains within the region of stability except for a short time when it crosses the narrow unstable area between the main stable region and the stable extension region. The ionosheath magnetic field vectors are shown for completeness.

Figure 3-23 is a composite picture of the orbital cross-section plane. The symmetry of the magnetic field strength contours ("above" and "below" the magnetic equator) is an artifact of the averaging process. The stable regions are not shown in this figure because it is impossible to depict the relative separation of these stable regions in a composite format. Once again, the ion data is used to determine the ionopause altitude. As seen in Figure 3-24, the inbound ionopause crossing is not near the observed strong magnetic field gradient. Instead, the strong magnetic field gradient coincides with the boundary between the stable and unstable regions. Of course, if the ionosphere is unstable immediately inside the ionopause, then the ionopause crossing will be characterized by a strong magnetic field gradient. The important point is that strong magnetic field gradients are due to ionospheric dynamics and are not a physical characteristic of the ionopause.

The outbound ionopause crossing is poorly defined because of a superthermal ion region above 270 km (Taylor et al., 1980). As with Orbit 170, a change of the outbound ionopause altitude by about 20 km will not affect the analysis. At most, the ionopause crossing time will be reduced by a few seconds, and the only other change would be a small decrease in the size of the stable region just below the outbound ionopause.

Figure 3-20. Orbit 175--horizontal projection of magnetic parameters. This is the first of three figures showing the average field orientation every 6 minutes as the field rotates at a constant rate of 2.5 degrees per minute. The valid altitude range is shown on the right hand edge of the figure (450-300 km). The field lines are shown by the solid curved lines. The stability contours (dash lines) are: inner contour (shaded is at 350 km and the outer contour is at 450 km). The ionospheric stable region is enclosed by a "box." The ionospheric altitude range is shown by the sidebar; the sidebar arrows mark the inbound ionopause crossing and the end of the valid altitude ranges (300 km). The observed magnetic field vectors (arrows) are shown for the ionosheath and ionopause stable region. The cross denotes the subsolar point. The scale on the upper left hand corner of the figure is the distance, in degrees, from the plasma flow origin (solid circle). The crosshatch area designates the boundary of the planetary disk. The asymmetry factor is 2.0 and the maximum field strength is 160 gamma.

ORBIT 175/1

105

100 GAMMA

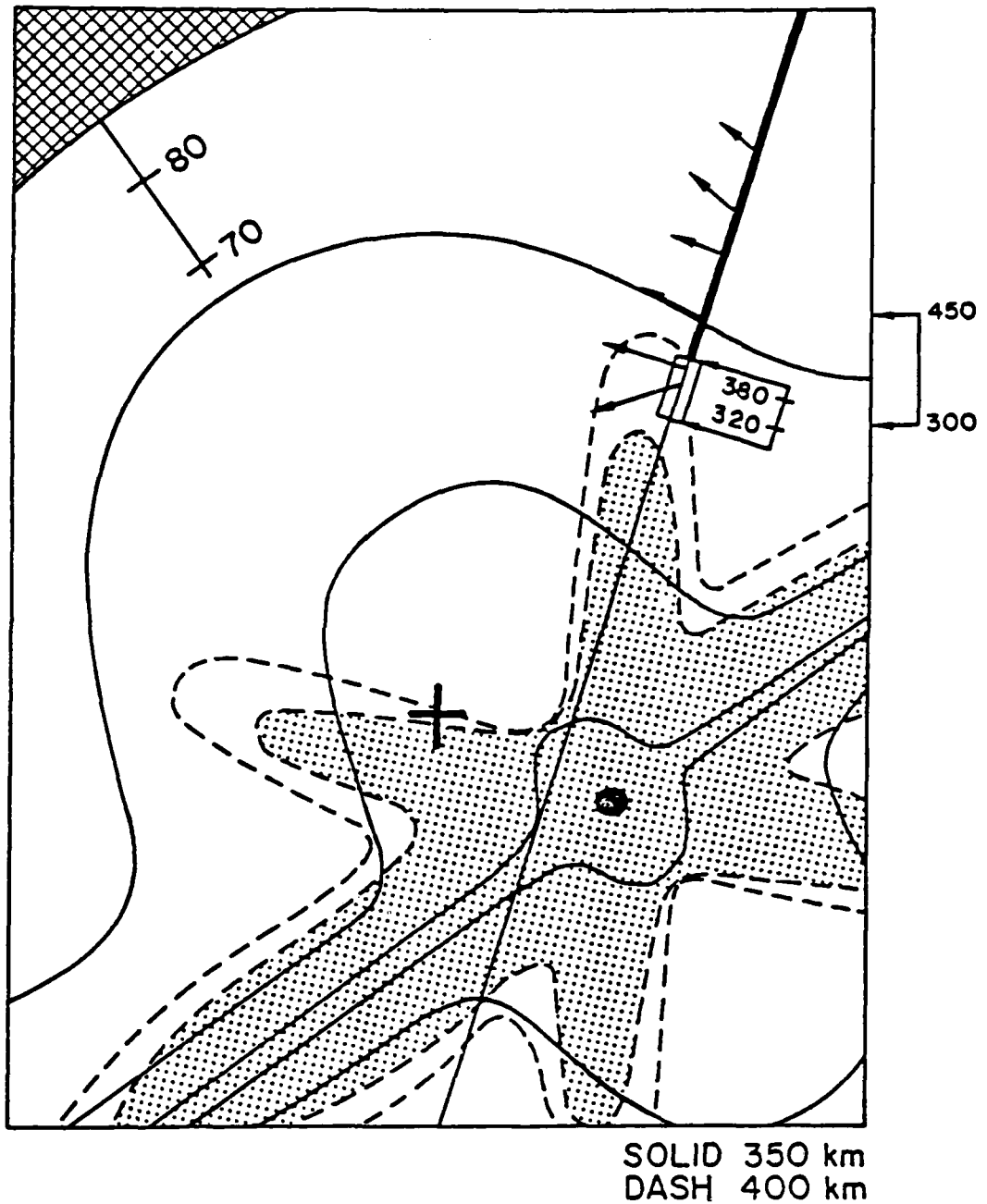


Figure 3-20

Figure 3-21. Orbit 175/2--horizontal projection. This figure shows the average field orientation 6 minutes after Figure 3-20. The valid altitude range is 250 km down to 145 km (periapsis). The stability contours are: inner contour (shaded) is for 250 km and the outer contour is for 300 km. The sidebar is used to indicate altitudes within the ionosphere. No field vectors are shown because this area of the ionosphere is unstable. The plasma flow origin remains fixed. The asymmetry factor is 2.0 and the maximum field strength is 160 gamma.

ORBIT 175/2

107

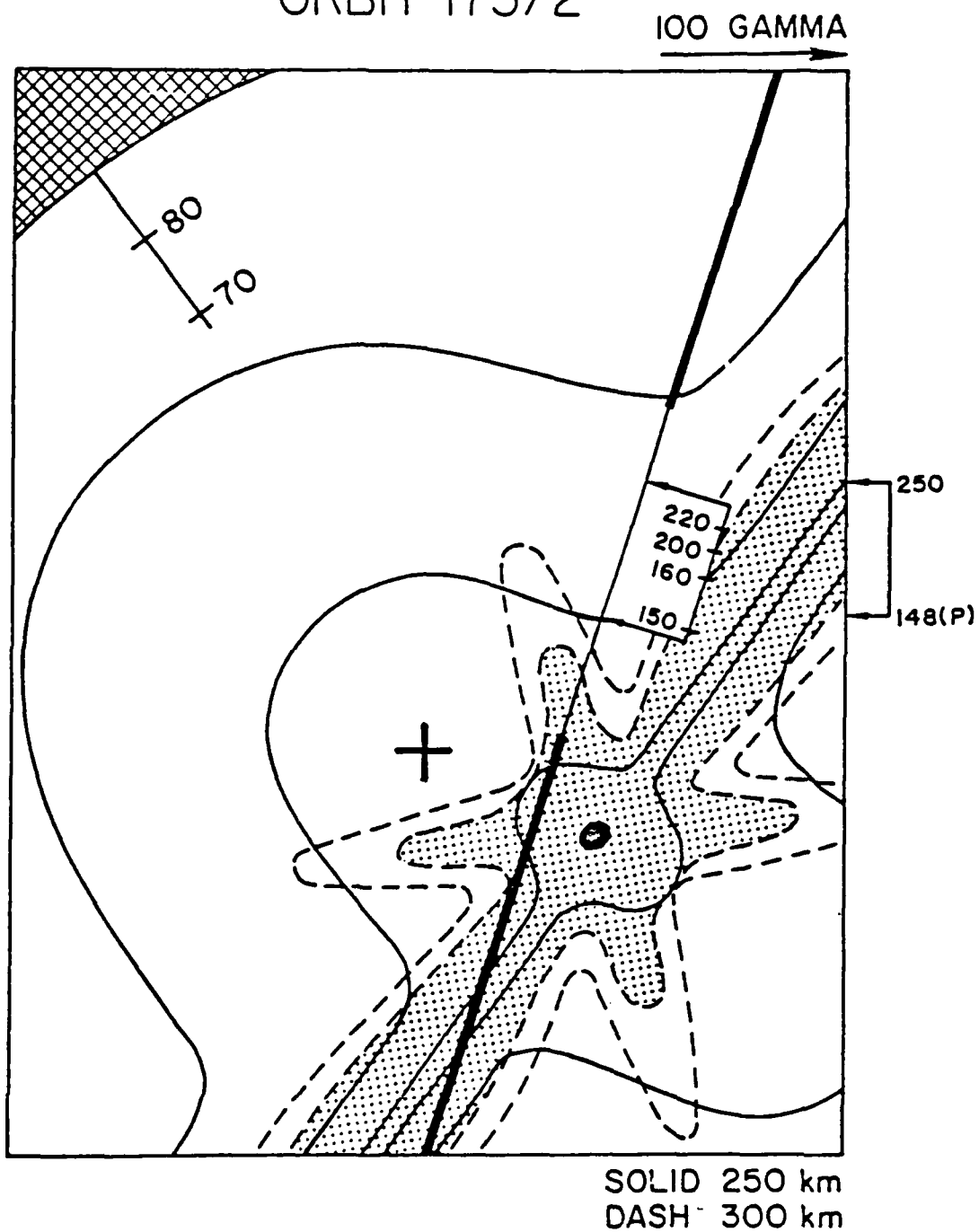


Figure 3-21

Figure 3-22. Orbit 175/3--horizontal projection. This figure shows the average field orientation 6 minutes after Figure 3-21. The valid altitude range is 161 km up to 450 km. The stability contours are: inner contour (shaded) is at 250 km and the outer contour is at 350 km. The ionospheric stable regions are enclosed by the shaded "boxes"; the shading indicates that the stable region is encountered near the 250 km level. The outbound ionopause crossing is at 300 km. The asymmetry factor is 2.0 and the maximum field strength is 160 gamma.

ORBIT 175/3

109

100 GAMMA

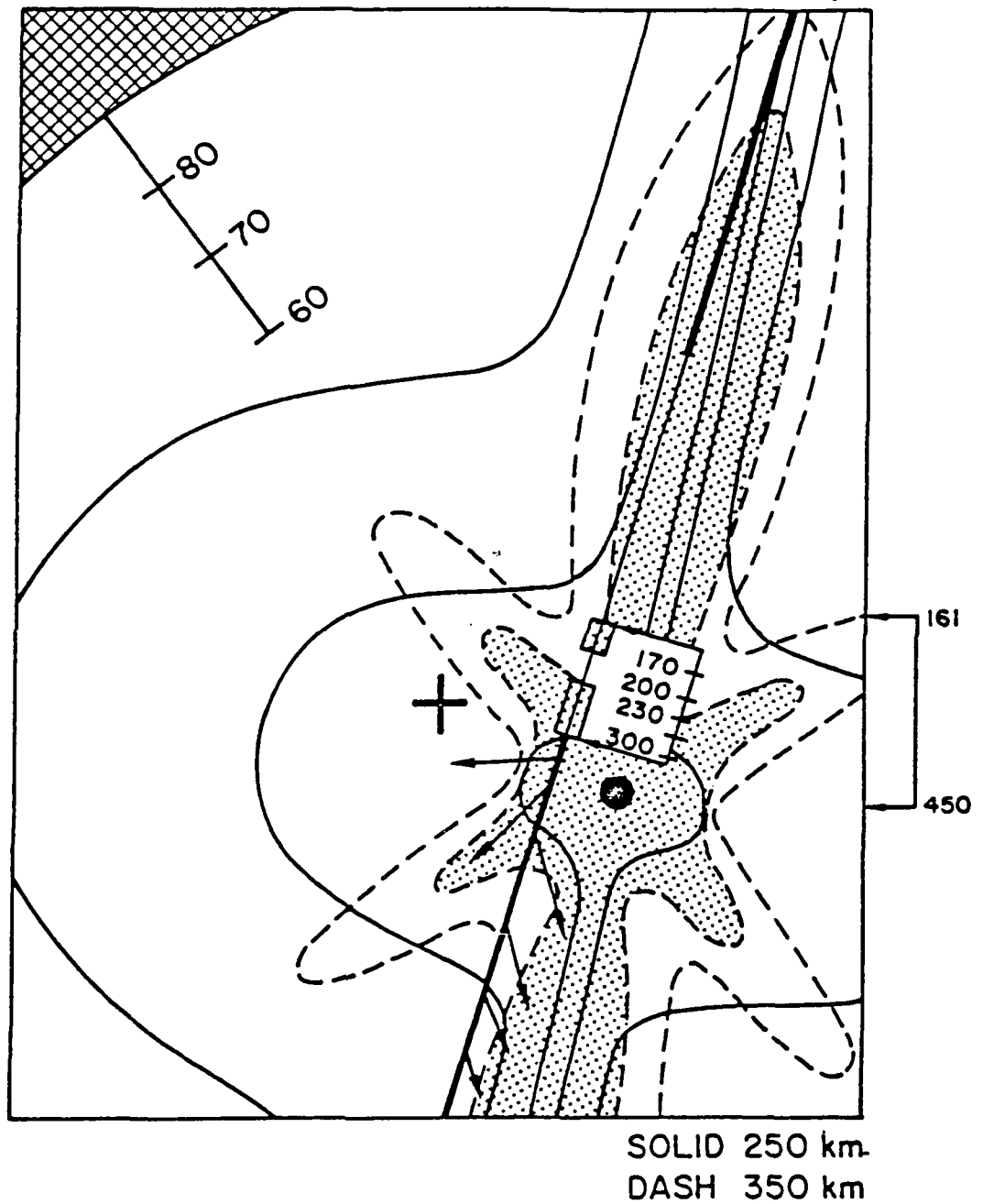


Figure 3-22

Figure 3-23. Orbit 175--orbital plane cross-section. The contours of constant magnetic field strength are solid lines in the ionosphere and dash lines in the ionosheath. Contour magnitudes are relative to the stagnation point maximum. The cross marks on the orbit are separated by one minute intervals relative to periapsis. This figure is a composite of Figures 3-20, 3-21, and 3-22; stable regions are omitted because of projection problems (see text).

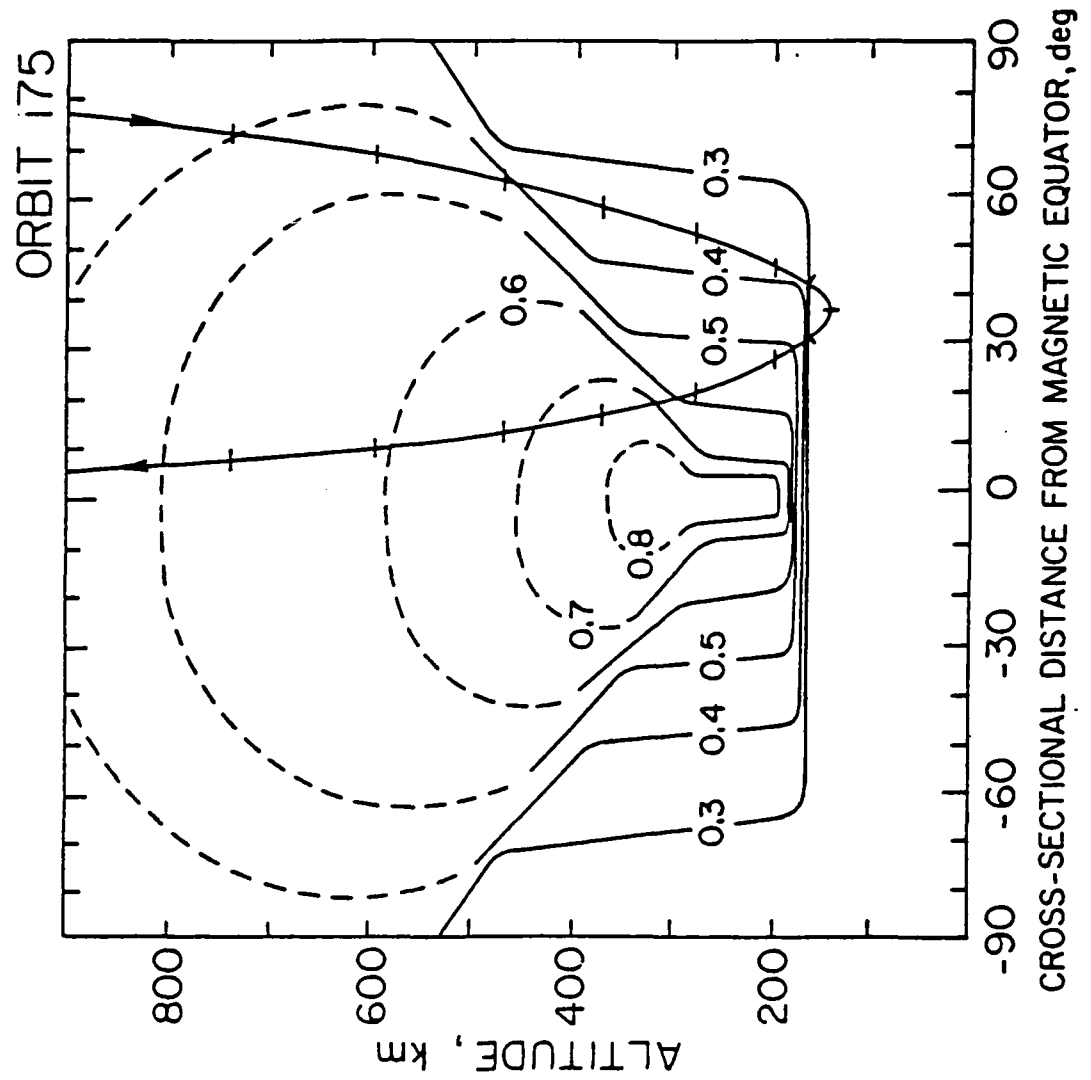


Figure 3-23

Figure 3-24. Orbit 175--comparison of model with observations. Model results (dash lines) are shown only for the stable regions. A break in the dash line designates a region of instability predicted by the model. The field strength scale (upper figure) is in gammas. The asterisks (*) are the OIMS measurements of atomic oxygen ion densities. The arrows beneath the time scale mark the ionopause crossings. The bottom figure shows how the magnetic field direction changes with time.

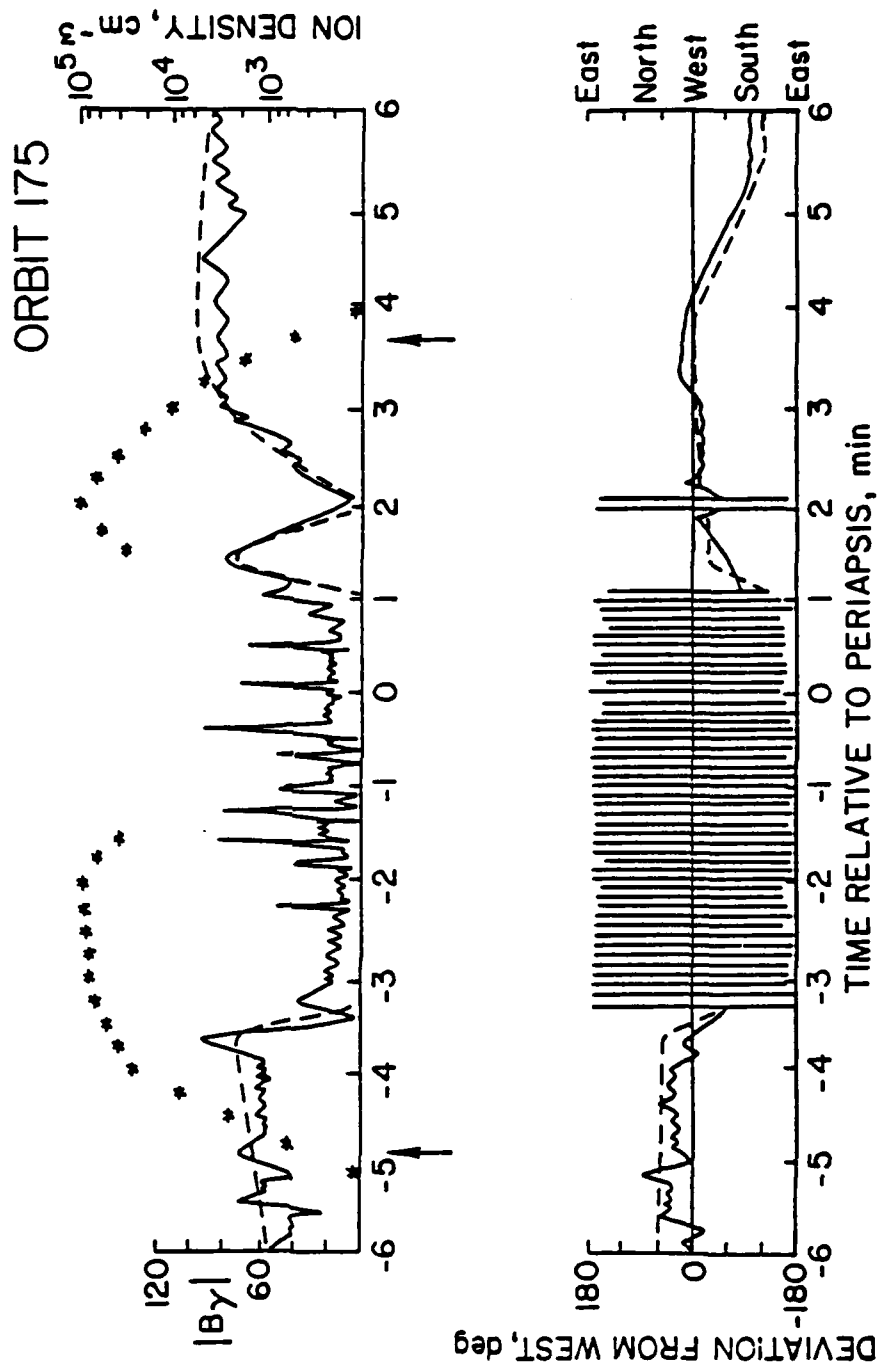


Figure 3-24

4. DISCUSSION

4.1 Comparison of Orbits

Orbits 176 and 177 have nearly the same magnetic field orientation relative to the orbital path, yet there is a significant difference in the PV magnetic field measurements for these two orbits (see Figures 3-10 and 3-13). The difference in the observed magnetic field strength is most likely due to an observed decrease in the solar wind dynamic pressure (Elphic et al., 1980a). Variability in the solar wind dynamic pressure is also responsible for the change in size and shape of the region of stability for Orbit 177 compared to Orbit 176 (see Figures 3-8 and 3-11). That is, increased solar wind dynamic pressure enhances the plasma depletion mechanism which, in turn, increases both the magnetic field strength and the velocity asymmetry. Since the ionospheric magnetic field is closely coupled with the plasma flow, enhanced plasma depletion also produces a larger magnetic field asymmetry. The change in the field asymmetry reduces the angle θ between v and B for intermediate azimuthal angles, and together with the increased field strength, these two stabilizing effects outweigh the destabilizing effect of the enhanced flow velocity. Therefore, the PV orbiter has the best chance of intersecting a stable region during periods of high solar wind dynamic pressure because, on these days, the region of stability is enlarged (i.e., Orbit 176 versus Orbit 177). In fact, this

statistical prediction has been verified by PV observations (Luhmann et al. 1980, 1981b).

The magnetic field observations are also sensitive to changes of the field orientation relative to the orbital path. For example, if the field pattern were rotated 10° counterclockwise in Figure 3-11 (Orbit 177), then the orbiter would remain within the stable region throughout the ionospheric transit. However, a 10° clockwise rotation would put most of the orbital path into an unstable area. Therefore, small field rotations can have a dramatic effect on the magnetic field measurements. Unfortunately, similar "looking" magnetic field measurements may result from entirely different field geometries, and this may mislead an observer into thinking that similar "looking" field measurements represent the same physical ionospheric conditions. For example, the field strength measurements for Orbit 170 (Figure 3-7) and Orbit 189 (Figure 3-19) appear very similar, but comparing Figures 3-5 and 3-17 shows that the ionospheric conditions for these orbits were very different.

Orbits 177 (Figure 3-11) and 188 (Figure 3-14) provide another useful example. The field geometry for these two orbits is similar but the measured field strengths are very different (see Figures 3-13 and 3-16). Certainly one difference is that the field geometry for Orbit 188 is rotated slightly relative to Orbit 177. However, the most important feature is that periapsis for Orbit 188 is relatively far

from the field pattern center and therefore, Orbit 188 exits the ionosphere before it can enter the region of stability.

4.2 Comparison with the 2-D Electrodynamic Model

The modified two-dimensional electrodynamic model (Cloutier et al, 1981) assumed that the ionospheric magnetic field lines were nearly straight lines lying across the dayside planetary disk. The two-dimensional model horizontal contours of constant magnetic field strength are shown by the solid lines in Figure 4-1 and the straight dashed lines are the plasma flow streamlines. The curved lines are the horizontal field strength contours from the three-dimensional flow/field model: only the 0.6 and 0.2 contours are shown. Even though there is a significant difference between the two models, the two-dimensional model gives excellent field strength results for Orbits 175, 176 and 177. For example, the two-dimensional model analysis for Orbit 177 is shown in Figure 4-2. Returning to the flow/field analysis of Orbit 177 (see Figures 3-11, 3-12 and 3-13), notice that the orbital path is nearly parallel to the magnetic equator. For this range of azimuthal angles, the flow/field model's magnetic field strength contours are nearly straight lines. Therefore, although not completely physically correct, the two-dimensional model gives quantitatively correct results because the straight line contour assumption was, in fact, a good approximation for Orbit 177. A similar argument is true for Orbits 176 and 175.

Another feature of the two-dimensional model was that the instability criterion was written as:

$$\frac{\rho v^2}{\frac{B^2 \cos^2 \theta}{\mu_0}} > C \quad (4.2.1)$$

where C was an empirical factor which ranged in value from .01 to 1.0. The C parameter was needed to explain the daily variability of the Pioneer-Venus magnetic field strength observations. It turns out that the C parameter is nothing more than a scaling factor which is needed to properly project the three dimensional stable region geometry onto the two-dimensional analysis plane. Therefore, with the more complete three-dimensional flow/field model, the C parameter becomes unnecessary, and the stability ratio is simply given by equation (2.5.2).

Figure 4-1. Comparison of horizontal magnetic field strength contours. The solid lines are the two-dimensional (electrodynamic) model contours; the contours are labeled relative to the maximum field strength at the stagnation point (i.e. 0.5 = 50% of B_{\max}). The straight dash lines are the plasma flowlines, and the circle represents the "sub-flow" region. The curved lines are field strength contours from the three dimensional model (only the 0.6 and 0.2 contours are shown).

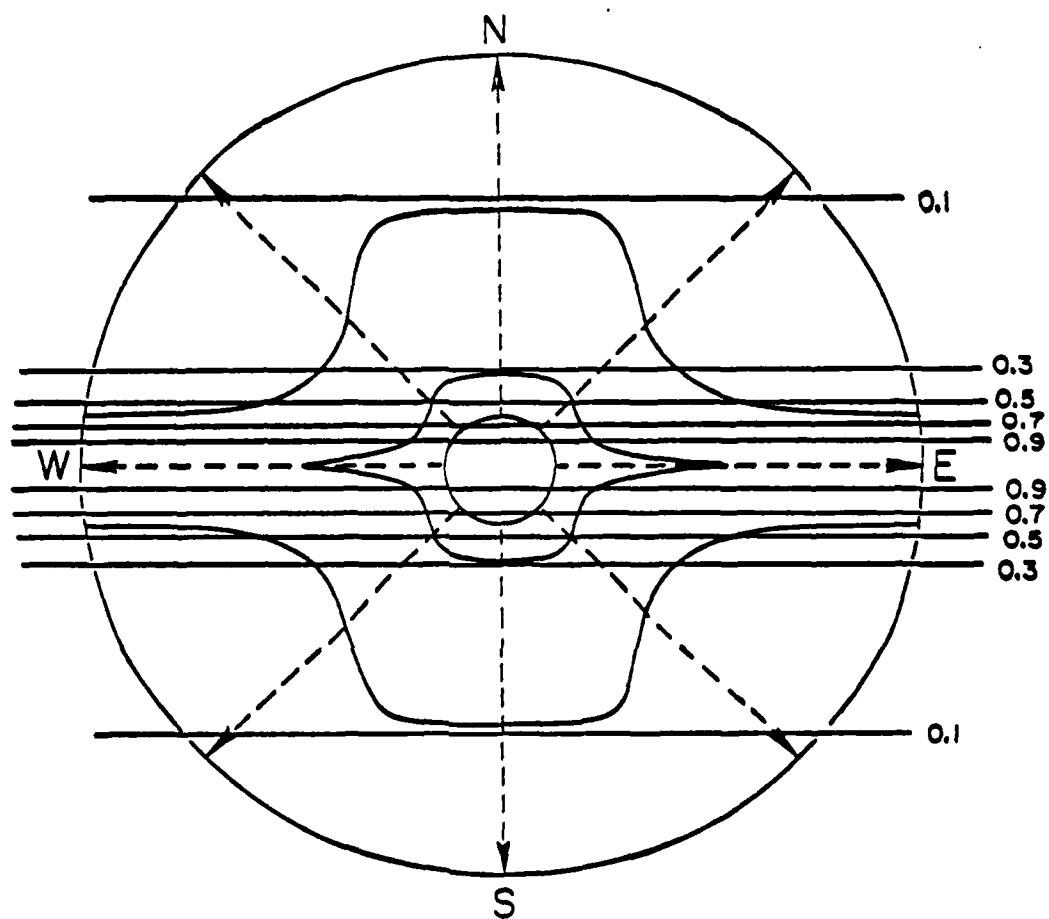


Figure 4-1

Figure 4-2. Comparison of Pioneer Venus observations with the two dimensional electrodynamic model. The upper panel contains the observations and the lower panel shows the model results. The horizontal scales are universal time (UT) and time relative to periapsis (RT). The bracket beneath the time axis indicates the extent of the stable magnetic field region computed by the model (from Cloutier et al., 1981).

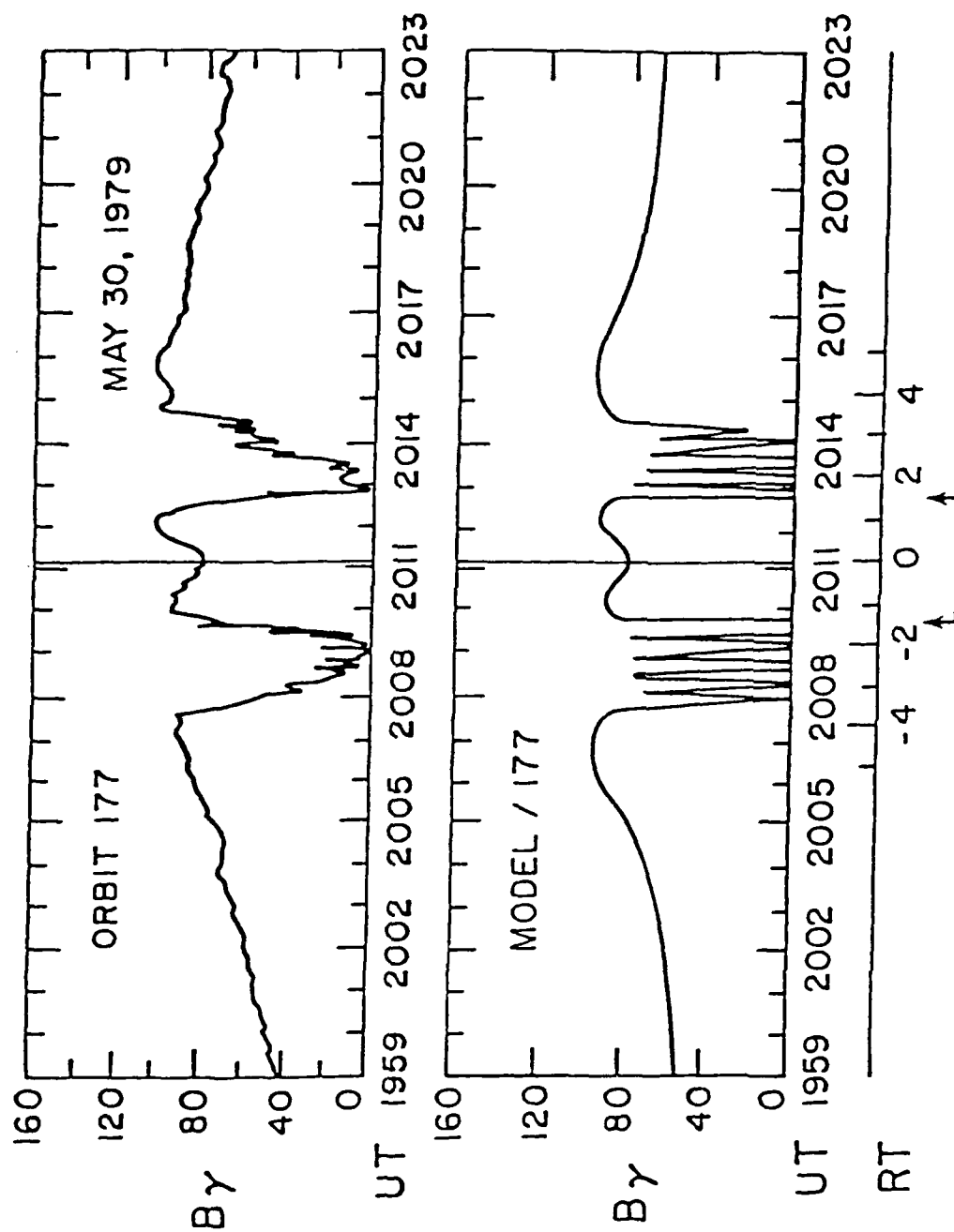


Figure 4-2

4.3 Problem Areas

One of the major computational problems was to maintain a reasonable decrease in the magnetic field strength near the magnetic equatorial terminator. This problem was overcome by introducing a weak radial magnetic field which was confined to a small region about the magnetic equator at large solar zenith angles. This weak radial field component satisfies all the MHD equations, including Gauss's Law, and it contributes, at most, 5% of the total field strength. Therefore, the horizontal assumption is still valid. A more complete discussion is given in Appendix 2.

Another problem is that the model assumes that the ionization is symmetric about the sub-flow point rather than the subsolar point. In the dayside ionosphere, this assumption introduces only a small error because the ionization rate is not very sensitive to small changes in the solar zenith angle near the subsolar point (Chamberlain, 1978). Moving the ionization center to the subsolar point would require a major revision of the flow/field model because improved chemistry algorithms would be needed to handle the asymmetry in the ion production and loss process. Such a modification might be done at a later date.

5. CONCLUSION

The assumption that, far from Venus sub-flow point, the ionospheric plasma flow and magnetic fields are strictly horizontal made it possible to find analytic solutions to the three dimensional MHD equations. It was also shown that an asymmetry exists in plasma flow distribution: the plasma flows faster perpendicular to the magnetic fields than parallel to these fields. This velocity asymmetry was largest near the ionopause and became less pronounced at low altitudes because of frequent collisions with ambient thermal ions. High altitude plasma flow velocities are on the order of 1 to 2 km/sec and the velocity asymmetry (v_{\perp}/v_{\parallel}) can be as high as 3 to 1. Since the ionosphere is a good conductor, the magnetic diffusion time is very long, and the close coupling of the magnetic field with the plasma flow produced an asymmetry in the magnetic field geometry. Unlike the plasma, the magnetic field asymmetry is nearly constant with altitude. It was also shown that a velocity shear within the plasma flow makes the ionosphere susceptible to the Kelvin-Helmholtz instability. This instability occurs whenever the plasma flow energy exceeds the restraining energy supplied by the magnetic field tension. Calculations showed that the flow energy and field tension were both strong functions of azimuth and the resulting region of stability has a rather unusual topology. This topology

played a key role in understanding the daily magnetic observations of Pioneer-Venus.

Some important results of this study are:

1) the same model can explain the total spectrum of ionospheric conditions ranging from total instability to complete stability with only small changes in input parameters;

2) solar wind characteristics (IMF direction and ram pressure) are important factors in describing the observed magnetic field observations;

3) magnetic field strength measurements which appear similar may represent very different physical conditions;

4) conversely, similar magnetic field geometries may produce very different magnetic field observations because of small orbital alignment differences;

5) the model predicts that during periods of high solar wind dynamic pressure, the orbiter has a better chance of encountering stable magnetic fields within the ionosphere; and

6) strong magnetic field gradients are due to ionospheric dynamics and are not a unique physical characteristic of the ionopause. That is, the definition of the ionopause most consistent with the physical mechanisms controlling the ionosphere of Venus is the sharp gradient in thermal plasma marking the transition from planetary ionization to post-shock solar wind plasma.

APPENDIX: ANALYTIC EQUATIONS FOR THE THREE DIMENSIONAL
FLOW/FIELD MODEL

A.1. Magnetic Field Equations

This section contains the derivation of the magnetic field equations discussed in Section 2.3 (equations 2.3.1a, 2.3.1b and 2.3.2). As stated earlier, the third equation of motion (2.1.11) together with Gauss's Law (2.1.12) completely describes the magnetic field geometry. The method of solution is complicated because these coupled differential equations do not separate easily. As a matter of convenience, the third equation of motion and Gauss's Law are repeated below

$$B_m \left(\frac{1}{\sin m} \frac{\partial B_m}{\partial \phi} - \frac{\partial B_\psi}{\partial m} - \frac{B_\psi}{\tan m} \right) = - \frac{\mu_0}{\sin m} \frac{\partial p}{\partial \phi} \quad (A.1.1)$$

$$\frac{\partial B_m}{\partial m} + \frac{B_m}{\tan m} + \frac{1}{\sin m} \frac{\partial B_\psi}{\partial \phi} = 0 \quad (A.1.2)$$

where

$$\vec{B} = B_m \hat{m} + B_\psi \hat{\psi} \quad (A.1.3)$$

The angles m and ψ , and the unit vectors \hat{m} and $\hat{\psi}$ are shown in Figure 2-1.

The first step is to find the homogeneous solution to the above set of coupled equations. Physically, the

homogeneous solution corresponds to the form of the field equations in the limit of small ψ (azimuthal angle). As discussed in Section 2.3, for small ψ , the magnetic field is nearly parallel to $\hat{\psi}$ and since the plasma is free to move parallel to the field, the azimuthal pressure gradient ($\frac{\partial P}{\partial \psi}$) will be minimized. Combining equations (A.1.1) and (A.1.2), in the limit of no azimuthal pressure gradient, we find that

$$\sin^2 m \frac{\partial^2 B_m}{\partial m^2} + 3 \sin m \left[\cos m \frac{\partial B_m}{\partial m} \right] - B_m [\sin^2 m - \cos^2 m] = \frac{-\partial^2 B_m}{\partial \psi^2} \quad (\text{A.1.4})$$

where equation (A.1.4) is in terms of only one field component, B_m . Next, using the separation of variables

$$B_m(m, \psi) = k(m) I(\psi) \quad (\text{A.1.5})$$

equation (A.1.4) becomes

$$\frac{\sin^2 m}{k} \frac{\partial^2 k}{\partial m^2} + \frac{3 \sin m \cos m}{k} \frac{\partial k}{\partial m} - [\sin^2 m - \cos^2 m] = \frac{-1}{I} \frac{\partial^2 I}{\partial \psi^2} \quad (\text{A.1.6})$$

Since the right hand side is in terms of $I(\psi)$ alone, then

$$-\frac{1}{I} \frac{\partial^2 I}{\partial \psi^2} = a^2 \quad (\text{A.1.7})$$

or

$$I = c e^{\pm i a \phi} \quad (\text{A.1.8})$$

where a and c are constants. Substituting (A.1.8) back into (A.1.6) and rearranging terms we find

$$\frac{\partial^2}{\partial m^2} [\sin^2 m k] - \frac{1}{\tan m} \frac{\partial}{\partial m} (\sin^2 m k) + [1 - a^2] = 0 \quad (\text{A.1.9})$$

Using the following change of variables

$$f = \sin^2 m k(m) \quad (\text{A.1.10a})$$

$$z = \cos m \quad (\text{A.1.10b})$$

equation (A.1.9) becomes

$$(1 - z^2) \frac{\partial^2 f}{\partial z^2} + \frac{f}{(1 - z^2)} (1 - a^2) = 0 \quad (\text{A.1.11})$$

Possible solutions for (A.1.11) are of the form

$$f_1(z) = \sum_{\lambda} \alpha_{\lambda} (1 - z^m)^n + \lambda \quad (\text{A.1.12})$$

and

$$f_2(z) = \sum_{\lambda} \beta_{\lambda} z^{n + \lambda} \quad (A.1.13)$$

We will look at each of these possible solutions separately and combine them later to produce the general homogeneous solution.

Substituting (A.1.12) into (A.1.11) and solving for various values of m , we obtain the following constraints:

$$m = \text{arbitrary}, \quad a = 1, \quad n + \lambda = 0 \quad (A.1.14a)$$

$$m = 1, \quad a = 1, \quad n + \lambda = 1 \quad (A.1.14b)$$

$$m = 2, \quad a = 0, \quad n + \lambda = 1/2 \quad (A.1.14c)$$

Combining (A.1.12) with (A.1.8) and (A.1.5), we find that for constraint (A.1.14a)

$$B_{ma} = \frac{\alpha_1}{\sin^2 m} [c_1 \cos \phi + c_2 \sin \phi] \quad (A.1.15)$$

for constraint (A.1.14b)

$$B_{mb} = \frac{\alpha_2}{\sin^2 m} (1 - \cos m) [c_3 \cos \phi + c_4 \sin \phi] \quad (A.1.16)$$

and finally, for constraint (A.1.14c)

$$B_{mc} = \frac{\alpha_3}{\sin m} (c_5 \phi + c_6) \quad (A.1.17)$$

The general solution for the first case (A.1.12) is simply a linear combination of (A.1.15), (A.1.16) and (A.1.17):

$$B_{m_1} = \frac{b_0}{\sin m} \phi + \sin \phi \left(\frac{b_1 + b_2 \cos m}{\sin^2 m} \right) \quad (\text{A.1.18})$$

where b_0 , b_1 and b_2 represent a collection of the constants from (A.1.15), (A.1.16) and (A.1.17). In the derivation of (A.1.18), we have applied the boundary condition that

$$\lim_{\phi \rightarrow 0} B_{m_1} = 0 \quad (\text{A.1.19})$$

The constraints for the other possible series solution (A.1.13) are found by substituting (A.1.13) into (A.1.12). The resulting constraints are

$$a = 1, n + \lambda = 0 \quad (\text{A.1.20a})$$

$$a = 1, n + \lambda = 1 \quad (\text{A.1.20b})$$

and the solution for B_{m_2} is

$$B_{m_2} = \frac{(b_3 + b_4 \cos m)}{\sin^2 m} \sin \phi \quad (\text{A.1.21})$$

where again we have applied boundary condition (A.1.19). Notice that the solution (A.1.21) is already contained in (A.1.18) and therefore, the general solution for the

component B_m is

$$B_m = \frac{b_0 \psi}{\sin m} + \frac{\sin \psi}{\sin^2 m} (b_1 + b_2 \cos m) \quad (\text{A.1.22})$$

A similar analysis can be done for the B_ψ component and the resulting solution is

$$B_\psi = \frac{a_0(\psi - \pi/2)}{\sin m} + \frac{\cos \psi}{\sin^2 m} (a_1 + a_2 \cos m) \quad (\text{A.1.23})$$

where we have applied the boundary condition

$$\lim_{\psi \rightarrow \pi/2} B_\psi = 0 \quad (\text{A.1.24})$$

Equations (A.1.22) and (A.1.23) can be simplified further by remembering that these equations must satisfy both the third equation of motion and Gauss's Law. This additional constraint requires that the constants in (A.1.22) and (A.1.23) must be related such that

$$B_{mH} = \frac{\sin \psi}{\sin^2 m} (a_2 - a_1 \cos m) \quad (\text{A.1.25})$$

$$B_{\psi H} = \frac{\cos \psi}{\sin^2 m} (a_1 - a_2 \cos m) \quad (\text{A.1.26})$$

The subscript H is used to identify these as the homogeneous solutions which are valid for small ψ . In order to extend

the solutions for all ϕ , we must return to the inhomogeneous coupled equations (A.1.1) and (A.1.2).

In order to simplify the analysis, we will assume that the azimuthal pressure gradient effects can be completely contained within the B_m component. Justification for this assumption is both mathematical and physical. First, mathematically the assumption allows one to find an analytic solution to this coupled set of inhomogeneous differential equations. This certainly isn't reason enough to use the above assumption. However, the assumption produces analytic solutions whose form fits the behavior one would physically expect. That is, the field lines are elliptically shaped for small ϕ , and then as ϕ increases, the field lines turn and become parallel to the external IMF direction. Therefore, we will assume that

$$B_m = B_{m_0} + B_{m_H} \quad (\text{A.1.27})$$

$$B_\phi = B_{\phi_H} \quad (\text{A.1.28})$$

where B_{m_0} is the term which parameterizes the effects of the azimuthal pressure gradient. Using equations (A.1.27) and (A.1.28), the third equation of motion (A.1.1) becomes

$$B_m \left(\frac{1}{\sin m} \frac{\partial B_{m_0}}{\partial \phi} \right) = - \frac{1}{\sin m} \frac{\partial P}{\partial \phi} \quad (\text{A.1.29})$$

and Gauss's Law becomes

$$\frac{\partial B_{m_0}}{\partial m} + \frac{B_{m_0}}{\tan m} = 0 \quad (\text{A.1.30})$$

We will further assume that B_{m_0} is separable and of the form

$$B_{m_0}(m, \phi) = x(m) y(\phi) \quad (\text{A.1.31})$$

Substituting (A.1.31) into (A.1.30) and integrating, one finds

$$x(m) = \frac{a_0}{\sin m} \quad (\text{A.1.32})$$

where a_0 is an integration constant. The form of $y(\phi)$ is more difficult to determine. First we need to examine the behavior of the pressure gradient term. As stated earlier, the pressure gradient goes to zero in the limit of small ϕ because the pressure is nearly uniform for small ϕ . From equation (A.1.29) we can see that B_{m_0} itself must go to zero for small ϕ . A form of $y(\phi)$ which satisfies these constraints is

$$y(\phi) = \sum_{\gamma=1}^{\infty} c_{\gamma} (\phi - \sin \phi)^{\gamma} \quad (\text{A.1.33})$$

We will only use the first term of this series because, even with only the first term, the strength of the pressure grad-

ient is occasionally overestimated. Therefore, combining (A.1.33) and (A.1.32) with (A.1.31), B_{m_0} becomes

$$B_{m_0} = \frac{a_0}{\sin m} (\psi - \sin \psi) \quad (\text{A.1.34})$$

$$B_m = \frac{a_0}{\sin m} (\psi - \sin \psi) + \frac{\sin \psi}{\sin^2 m} (a_2 - a_1 \cos m) \quad (\text{A.1.35})$$

$$B_\psi = \frac{\cos \psi}{\sin^2 m} (a_1 - a_2 \cos m) \quad (\text{A.1.36})$$

where the constants a_0 , a_1 and a_2 are evaluated in Appendix A.2. This evaluation process is quite involved because all the necessary boundary conditions are not known and therefore, we must rely on geometric and physical arguments to evaluate the constants.

In practice, the field line geometry produced by equations (A.1.35) and (A.1.36) is correct. Unfortunately, the field strength falls off too slowly along the magnetic equator. That is, we would expect that the field strength should decrease near the terminator at a rate required by the external solar wind dynamic pressure. This was verified by Vaisberg et al. (1980a, 1980b) who found that the observed field strength variation was proportional to $\cos^2 \chi$, where χ is the expected angle between the normal to the ionopause and the solar wind direction. As explained in Section 2.3, eventhough Vaisberg et al. based their conclusion on unnormalized data, their proportionally relation

is probably quite reasonable. The model's field strength calculations approximate the $\cos^2\chi$ behavior with the introduction of a very weak radial magnetic field component. This radial component is confined to the vicinity of the magnetic equator and rarely contributes more than 5% of the total field strength. Therefore, the horizontal field approximation is still valid. The form of the radial component is

$$B_r = \frac{a_{01}}{2\epsilon \tan m} (\psi - \sin\psi) P_m P_\psi(n) \quad (\text{A.1.37})$$

where

$$P_m = (1 + 3\sin^2 m) e^{-1/(2\sin^2 m)} \quad (\text{A.1.38})$$

$$P_\psi(n) = \sin^n \psi e^{-1/(\sin\psi)^n} \quad (\text{A.1.39})$$

The introduction of this weak radial component requires a modification of the B_m component so that Gauss's Law is still obeyed. The final form of the field equations (including A.1.37) becomes

$$B_m = \frac{a_0(\psi - \sin\psi)}{\sin m} - a_{01} \sin^2 m e^{-1/(2\sin^2 m)} P_\psi(n) (\psi - \sin\psi) \\ + (a_2 - a_1 \cos m) \frac{\sin\psi}{\sin^2 m} \quad (\text{A.1.40})$$

and

$$B_{\psi} = \frac{\cos \psi}{\sin^2 m} (a_1 - a_2 \cos m) \quad (\text{A.1.41})$$

A.2 Determination of Constants

The first step is to determine an equation which relates the total field strength, B , to the angle θ , where θ is the angle between \underline{y} and \underline{B} . As shown in Section 2.3, the magnetic field can be written as

$$\underline{B} = B_m \hat{m} + B_\psi \hat{\psi} \quad (\text{A.2.1})$$

where

$$B_m = B \cos\theta \quad (\text{A.2.2})$$

$$B_\psi = B \sin\theta \quad (\text{A.2.3})$$

Substituting (A.2.2) and (A.2.3) into the third equation of motion (A.1.1) yields

$$\begin{aligned} \frac{\cos\theta}{\mu_0} \left[\frac{\cos\theta}{\sin m} \frac{\partial B}{\partial \psi} - \frac{B \sin\theta}{\sin m} \frac{\partial \theta}{\partial \psi} - \sin\theta \frac{\partial B}{\partial m} - \cos\theta B \frac{\partial \theta}{\partial m} - \frac{B \sin\theta}{\tan m} \right] \\ = - \frac{1}{\sin m} \frac{\partial P}{\partial \psi} \end{aligned} \quad (\text{A.2.4})$$

and Gauss's law becomes

$$\cos\theta \frac{\partial B}{\partial m} - B \sin\theta \frac{\partial \theta}{\partial m} + \frac{\sin\theta}{\sin m} \frac{\partial B}{\partial \psi} + \frac{\cos\theta}{\sin m} B \frac{\partial \theta}{\partial \psi} + B \frac{\cos\theta}{\tan m} = 0 \quad (\text{A.2.5})$$

Combining (A.2.4) with (A.2.5) gives

$$\frac{1}{\sin m} \frac{\partial}{\partial \psi} \frac{B^2}{2} - B \frac{\partial \theta}{\partial m} = - \frac{\mu_0}{\sin m} \frac{\partial P}{\partial \psi} \quad (\text{A.2.6})$$

and

$$\frac{\partial}{\partial m} \frac{B^2}{2} + \frac{B^2}{\tan m} + \frac{B^2}{\sin m} \frac{\partial \theta}{\partial \psi} = \frac{\mu_0 \tan \theta}{\sin m} \frac{\partial P}{\partial \psi} \quad (\text{A.2.7})$$

Equations (A.2.6) and (A.2.7) relate the magnetic field strength (B) to the field line geometry specified by the angle θ . A useful integratable equation is obtained in the limit of small ψ , where

$$\lim_{\psi \rightarrow 0} \frac{\partial P}{\partial \psi} = 0 \quad (\text{A.2.8})$$

Therefore, equations (A.2.6) and (A.2.7) become

$$\frac{1}{\sin m} \frac{\partial}{\partial \psi} \ln B = \frac{\partial \theta}{\partial m} \quad (\text{A.2.9})$$

and

$$\frac{\partial}{\partial m} \ln B + \frac{1}{\tan m} = - \frac{1}{\sin m} \frac{\partial \theta}{\partial \psi} \quad (\text{A.2.10})$$

In the limit of small ψ , the field line shape can be approximated by an ellipse (see Figure A-1). One can show that for the spherical triangle formed by the tangent line,

the arc length d_0 and the arc length m ,

$$\tan\theta = \left(\tan\phi \cos m - \frac{\tan((d_0 - d)/R)}{\sin\phi \sin m} \right)^{-1} \quad (\text{A.2.11})$$

where the arc length d is shown in Figure A-1, and R is the radial distance (from center of planet). Equation (A.2.11) is only valid in the limit of small ϕ . The second term on the right hand side of equation (A.2.11) needs further evaluation because, in the limit of small ϕ , d approaches d_0 . It's easiest to continue this analysis in the projection plane.

In the projection plane

$$\frac{D_0 - D}{r} = \frac{a^2}{b^2} \frac{\sin^2\phi}{\cos\phi} \quad (\text{A.2.12})$$

where r is the radial distance (in the plane), a is the semi-major axis and b is the semi-minor axis of the ellipse in the projection plane, D_0 is the projection of d_0 , and D is the projection of d . The angle ϕ does not change in the projection. Equation (A.2.12) is derived for the point where the tangent line touches the ellipse. Figure A-2 shows the relationship between the projection and surface parameters for small ϕ . One can show that

$$\sin\left(\frac{d_0 - d}{R}\right) = \frac{(D_0 - D)}{R} \cos m \quad (\text{A.2.13})$$

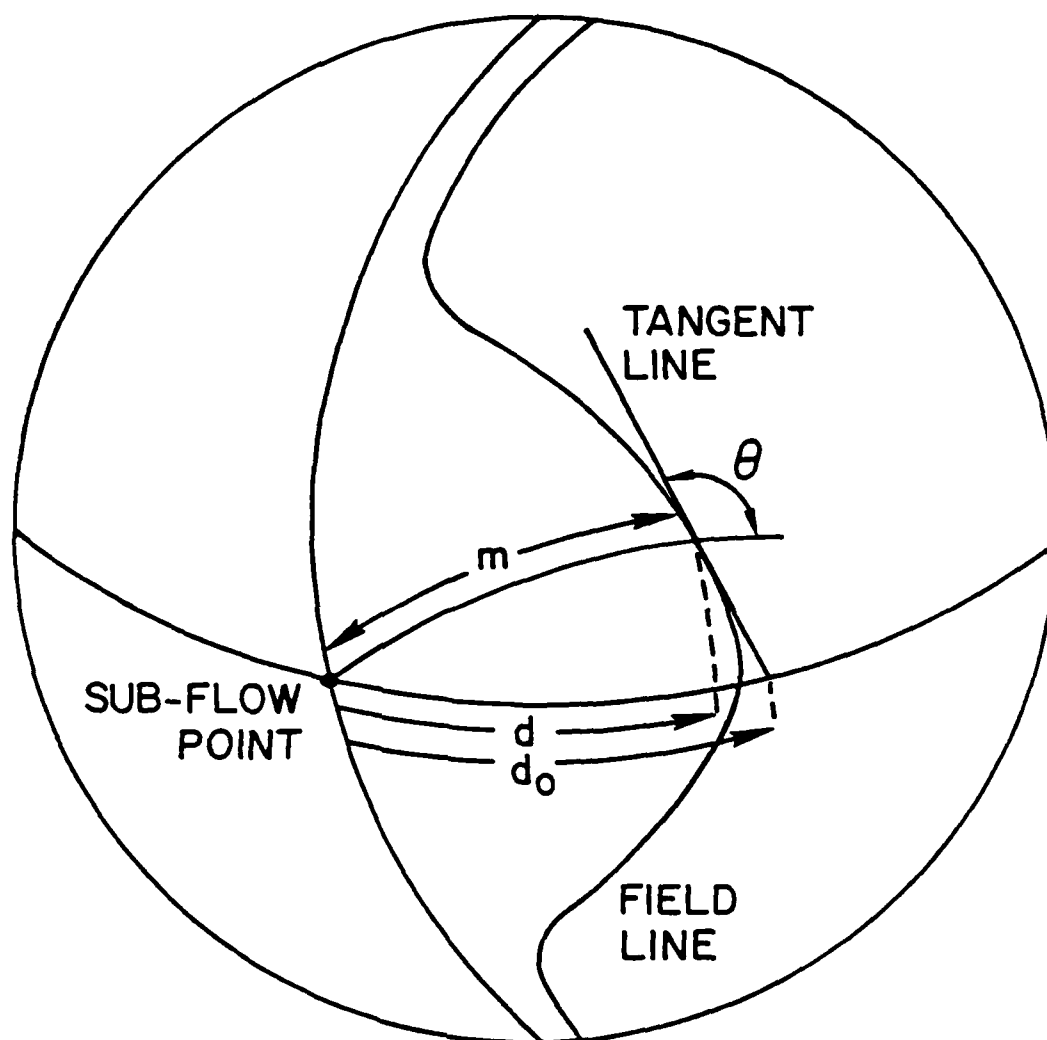


Figure A-1. Surface coordinates for field line geometry calculations.

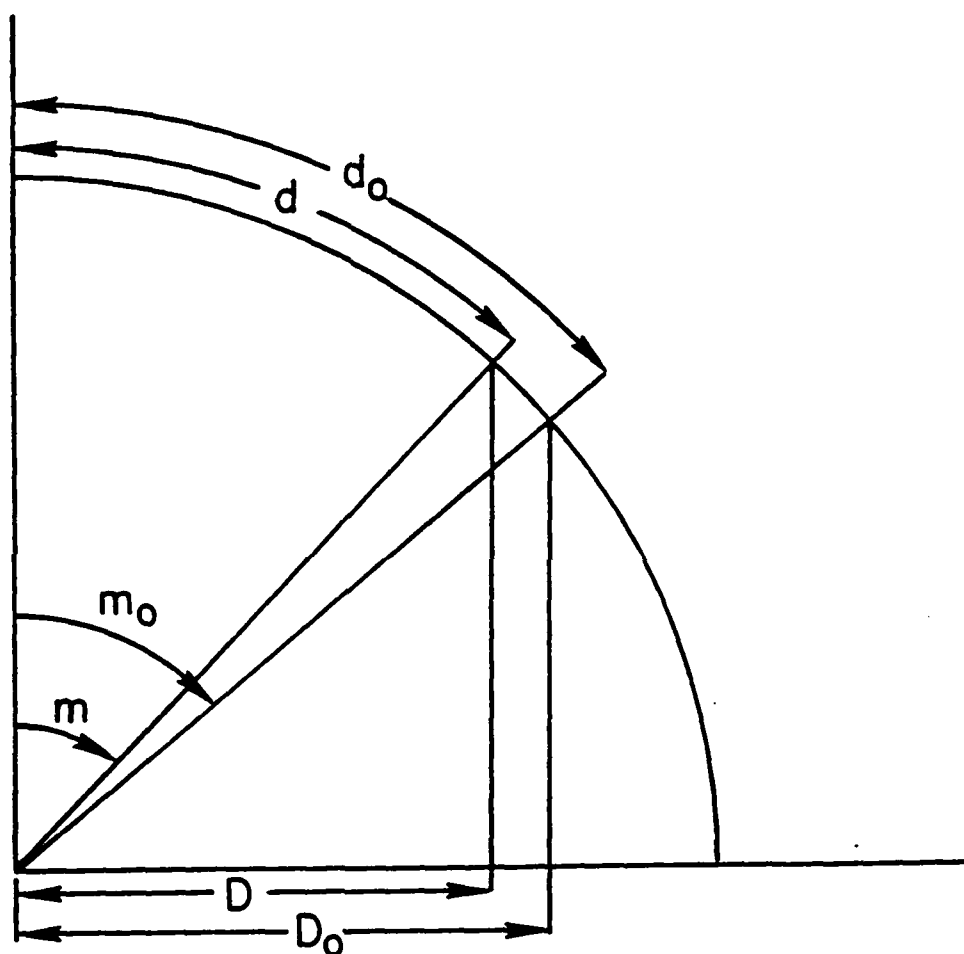


Figure A-2. Cross-section near the magnetic equator showing the relation between the surface variables and the projection plane variables.

and since d approaches d_0 as ψ goes to zero, then (A.2.13) becomes

$$d_0 - d = (D_0 - D) \cos m \quad (\text{A.2.14})$$

Substituting (A.2.14) into (A.2.12) yields

$$d_0 - d = \frac{a^2}{b^2} r \frac{\sin^2 \psi}{\cos \psi} \cos m \quad (\text{A.2.15})$$

where

$$r = R \sin m \quad (\text{A.2.16})$$

In the limit of small ψ ,

$$\tan \left(\frac{d_0 - d}{R} \right) \approx \frac{d_0 - d}{R} \quad (\text{A.2.17})$$

Therefore using (A.2.17), (A.2.16) and (A.2.15), equation (A.2.11) becomes

$$\tan \theta = \frac{1}{\tan \psi \cos m \left(1 - \frac{a^2}{b^2} \right)} \quad (\text{A.2.18})$$

and

$$\frac{\partial \theta}{\partial \psi} = - \cos m \left(1 - \frac{a^2}{b^2} \right) \quad (\text{A.2.19})$$

Equation (A.2.18) and (A.2.19) are only valid for small ϕ . Finally substituting (A.2.19) into (A.2.10), we find

$$\frac{\partial}{\partial m} \ln B = - \frac{a^2}{b^2} \frac{1}{\tan m} \quad (\text{A.2.20})$$

In terms of surface arc lengths

$$a = R \sin \left(\frac{v_1 t}{R} \right) = R \sin(m_a) \quad (\text{A.2.21})$$

$$b = R \sin \left(\frac{v_2 t}{R} \right) = R \sin(m_b) \quad (\text{A.2.22})$$

and

$$f = a/b \quad (\text{A.2.23})$$

where f is the surface asymmetry factor. If we assume that for small ϕ , that $m \approx m_a$, then (A.2.20) becomes

$$\ln \left(\frac{B}{B_i} \right) = - \frac{1}{2} \int_{m_i}^m \frac{\sin 2m}{\sin^2 \left(\frac{m}{f} \right)} dm \quad (\text{A.2.24})$$

Equation (A.2.24) can be solved analytically for a variety of field asymmetry factors. Furthermore, along the perpendicular direction ($\phi \approx 0$), equation (A.1.41) gives

$$\ln \left(\frac{B}{B_i} \right) = \ln \left[\frac{(a_1 - a_2 \cos m)}{(a_1 - a_2 \cos m_i)} \frac{\sin^2 m_i}{\sin^2 m} \right] \quad (\text{A.2.25})$$

Using (A.2.25) with (A.2.24), the constants a_1 and a_2 can be solved for relative to some initial value of B (the 2-D model of Cloutier et al. is a useful guide in selecting B_i). Therefore the two unknowns, a_1 and a_2 have been replaced by a single unknown B_i , which is a model input. Table A-1 contains a list of the constants a_1 and a_2 computed for various asymmetry factors and initial values of B .

In order to solve for the constants a_0 and a_{0_1} , one needs to determine how the field strength varies with solar zenith angle along the parallel direction ($\psi = \pi/2$). Vaisberg et al. (1980a, 1980b) report that the best fit to the SZA variation of the observed ionopause field strength is

$$\frac{B(\text{SZA})}{B_0} = \cos^2 \chi \quad (\text{A.2.26})$$

where B_0 is the nose value for the field strength and χ is the angle between the ionopause and the solar wind direction at a given SZA. However, (A.2.26) cannot be used directly because the PV observations were taken over a period of weeks. During this time, the PV orbit precessed toward the terminator, and there is no way to determine the location of the subflow point and the orientation of the IMF. Therefore, (A.2.26) is of limited value. The Vaisberg et al. study does show one important fact: the field strength near the terminator can be very high. Equation (A.2.26) will

prove to be a useful guide in evaluating the constants a_0 and a_{0_1} .

Unlike the constants a_1 and a_2 , there is no analytic expression available to evaluate a_0 and a_{0_1} directly. Instead, an iterative technique is used; it begins by picking a value for the field strength near the terminator and at $m = 40^\circ$. This is not a totally arbitrary procedure. That is, we know the value of B at the point $(\psi = 0, m = 40)$ and we require that

$$\frac{B(\psi = 90, m = 40)}{B(\psi = 0, m = 40)} > 1 \quad (\text{A.2.27})$$

Physically, equation (A.2.27) requires that the flow carries the field along faster in the perpendicular direction than in the parallel direction. As a first guess, the above ratio is set equal to the asymmetry ratio and the constant a_{0_1} is set to zero. Next the field strength is computed at the terminator and is then compared to the Vaisberg et al. results. If there is a substantial difference, then a_{0_1} is used to correct the field values. The procedure is repeated for different ratio values for (A.2.27). The correctness of each iteration is based on the computed field line shape. As discussed earlier, the constants a_0 and a_{0_1} represent the effects of density gradients on the field line geometry. By

selecting various combinations of a_0 and a_{0_1} , we are effectively changing ionospheric conditions. Table A-1 also contains a set of values for a_0 and a_{0_1} .

TABLE A-1. CONSTANT'S

Asymmetry Ratio	$\frac{B(\psi=0, m=40)}{B_0}$	$\frac{B(\phi=0, m=70)}{B_0}$	a_1	a_2	$\frac{B(\psi=90, m=40)}{B_0}$	a_0	a_{01}
1.25	0.4	0.235	0.241	0.1	0.45 0.5	0.74 0.8	1.8 1.8
1.5	0.4	.194	.176	.0142	0.45 0.6 0.8	0.84 1.0 1.2	1.7 1.7 1.8
1.5	0.23	0.1	0.101	.009	0.3 0.45 0.6	0.52 0.69 0.86	0.97 1.0 1.1
2.0	0.4	.116	0.05	-.148	0.6 0.8	1.2 1.4	1.5 1.6
	0.69	0.2	0.09	-.257	0.6 0.8	1.6 1.8	2.3 2.4
	0.8	0.387	0.35	0.0264	0.8	1.6	3.25
2.5	0.4	.0472	-.058	-.2915	0.6 0.9	1.35 1.69	1.3 1.47
3.0	0.4	0.028	-.089	-.33	0.6 0.9	1.39 1.73	1.24 1.4

A.3 Contours of Constant Magnetic Field Strength

The vertical field strength contours in the magnetic prime meridian plane were developed in an earlier series of papers (Daniell and Cloutier, 1977; Cloutier and Daniell, 1979). The average field strength distribution was calculated by a variational technique which required that the ionospheric volume Joule heating be a minimum for the induced current configuration. This calculation showed that the field strength contours were nearly straight vertical lines above 200 km up to the ionopause. The contours remain vertical even with large changes in the external IMF magnetic field strength (Cloutier et al, 1981). Along the magnetic equator, the field strength contour shape is found using the generalized Ohm's Law.

In MKS units, generalized Ohm's Law (Spitzer, 1962, Krall and Trivelpiece, 1973) is:

$$\text{curl}[(\underline{v} \times \underline{B}) - \underline{g}^{-1} \cdot \frac{\text{curl } \underline{B}}{\mu_0} + \frac{1}{q_e n_e} (\nabla P_e + \frac{\underline{B} \times \text{curl } \underline{B}}{\mu_0})] = 0$$

(A.3.1)

where \underline{v} is the plasma velocity, \underline{B} is the magnetic field vector, \underline{g}^{-1} is the resistivity tensor, P_e is the electron pressure, q_e is the electron charge, n_e is the electron density and μ_0 is the magnetic permeability of free space. Applying the condition that \underline{B} and \underline{v} are horizontal requires

that

$$\underline{B} = B_m \hat{m} + B_\psi \hat{\psi} \quad (\text{A.3.2a})$$

$$\underline{v} = v \hat{m} \quad (\text{A.3.2b})$$

where \hat{m} and $\hat{\psi}$ are the surface unit vectors defined in Figure 2-1. If we also restrict the analysis to the magnetic equatorial plane (along parallel axis, $B_\psi = 0$) and substituting (A.3.2) into (A.3.1) we find

$$\begin{aligned} \frac{m_e k}{q_e n_e} (\nabla n_e \times \nabla T_e) &= \frac{\hat{R}}{\mu_0} \left[\frac{1}{R} \frac{\partial}{\partial m} F_\psi + \frac{F_\psi}{R \tan m} - \frac{1}{R \sin m} \frac{\partial F_m}{\partial \psi} \right] \\ &+ \frac{\hat{m}}{\mu_0} \left[- \frac{\partial}{\partial R} F_\psi - \frac{F_\psi}{R} + \frac{1}{R \sin m} \frac{\partial F_R}{\partial \psi} \right] \\ &+ \frac{\hat{\psi}}{\mu_0} \left[- \frac{1}{R} \frac{\partial F_R}{\partial m} \right] \end{aligned} \quad (\text{A.3.3})$$

where

$$\underline{F} = \frac{\underline{B} \times \text{curl } \underline{B}}{\mu_0} \quad (\text{A.3.4})$$

We have also assumed that at high altitudes, the conductivity becomes very large (approaches 'frozen in' conditions) and therefore, the second term in equation (A.3.1) is ignorable. The electron pressure was approximated by the ideal gas law, where k is the Boltzman

constant. The first term in equation (A.3.1) vanishes because along the magnetic equator y is parallel to B . One would also expect that the azimuthal variation of the electron density and temperature near the magnetic equator would be small (i.e., $\frac{\partial n_e}{\partial \phi} \approx \frac{\partial T_e}{\partial \phi} \approx 0$) and therefore, equation (A.3.3) becomes

$$\begin{aligned} \frac{m_e k}{q_e n_e} \left(\frac{\partial n_e}{\partial R} \frac{\partial T_e}{\partial m} - \frac{\partial n_e}{\partial m} \frac{\partial T_e}{\partial R} \right) \hat{\phi} = \\ \frac{\hat{R}}{\mu_0} \left[\frac{1}{R} \frac{\partial}{\partial m} F_\phi + \frac{F_\phi}{R \tan m} - \frac{1}{R \sin m} \frac{\partial F_m}{\partial \phi} \right] \\ + \frac{\hat{m}}{\mu_0} \left[- \frac{\partial}{\partial R} F_\phi - \frac{F_\phi}{R} + \frac{1}{R \sin m} \frac{\partial F_R}{\partial \phi} \right] \\ + \frac{\hat{\phi}}{\mu_0} \left[- \frac{1}{R} \frac{\partial F_R}{\partial m} \right] \end{aligned} \quad (A.3.5)$$

In terms of known solutions for B (A.1.35 and A.1.36), F can be written as

$$\lim_{\phi \rightarrow \frac{\pi}{2}} F = \frac{\hat{R}}{\mu_0} \left(\frac{\partial}{\partial \phi} \left(\frac{B_m^2}{2} \right) + \frac{B_m^2}{R} \right) + \frac{\hat{\phi}}{\mu_0} \frac{B_m a_0}{R \sin^2 m} \quad (A.3.6)$$

Therefore, the \hat{m} component of equation (A.3.5) must be zero,

$$\frac{\partial F_\phi}{\partial R} + \frac{F_\phi}{R} - \frac{1}{R \sin m} \frac{\partial F_R}{\partial \phi} = 0 \quad (A.3.7)$$

and by substituting (A.3.6) into (A.3.7), one can show that

$$\frac{B_m}{B_{m_k}} = \left(\frac{R}{R_k}\right)^2 \quad (\text{A.3.8})$$

where B_{m_k} is the field strength value at the height R_k (measured from center of planet). Since R and R_k can be written as

$$R = R_v + h \quad \text{and} \quad h \ll R$$

$$R_k = R_v + h_k \quad h_k \ll R_k \quad (\text{A.3.9})$$

where R_v is the radius of Venus; then (A.3.8) becomes

$$\frac{B_m}{B_{m_k}} = \left(\frac{1 + h/R_v}{1 + h_k/R_v}\right)^2 \approx 1 \quad (\text{A.3.10})$$

Therefore, the field strength does not change significantly with height and, in the magnetic equatorial plane, the field strength contours are also vertical lines. It is not possible to solve for the field strength contours at any other location without first solving the full three dimensional MHD equations. Since the field strength contours are vertical lines at the two extremes ($\psi = 0$ and $\psi = \pi/2$), we will make the simplifying assumption that the field strength contours are vertical for all azimuthal angles.

REFERENCES

- Bauer, S. J., Donahue, T. M., Hartle, R. E., and Taylor, H. A. (1979). Venus ionosphere: photochemical and thermal diffusion control of ion composition. Science, 205, 109.
- Brace, L. H., Theis, R. F., Krehbiel, J. P., Nagy, A. F., Donahue, T. M., McElroy, M. B., and Pedersen, A. (1979a). Electron temperatures and densities in the Venus ionosphere: Pioneer Venus Orbiter Electron Probe results. Science, 203, 763.
- Brace, L. H., Theis, R. F., Niemann, H. B., Mayr, H. G., Hoegy, W. R., and Nagy, A. F. (1979b). Empirical models of the electron temperature and density in the nightside Venus ionosphere. Science, 205, 102.
- Brace, L. H., Theis, R. F., Hoegy, W. R., Wolfe, J. H., Mihalov, J. D., Russell, C. T., Elphic, R. C., and Nagy, A. F. (1980). The dynamic behavior of the Venus ionosphere in response to solar wind interactions. J. Geophys. Res., 85, 7663.
- Brandt, J. C. (1970). Introduction to the Solar Wind. W. H. Freeman and Co., San Francisco, p. 136.
- Chamberlain, J. W. (1978). Theory of Planetary Atmospheres: An Introduction to their Physics and Chemistry. Academic Press, New York, p. 167.

- Cloutier, P. A. (1976). Solar wind interaction with planetary ionospheres, in NASA Special Report SP-397, p. 111.
- Cloutier, P. A., McElroy, M. B., and Michel, F. C. (1969). Modification of the Martian ionosphere by the solar wind. J. Geophys. Res., 74, 6215.
- Cloutier, P. A., and Daniell, R. E. (1973). Ionospheric currents induced by the solar wind interaction with planetary atmospheres. Planet. Space Sci., 21, 463.
- Cloutier, P. A., Daniell, R. E., and Butler, D. M. (1974). Atmospheric ion wakes of Venus and Mars in the solar wind. Planet. Space Sci., 22, 967.
- Cloutier, P. A., and Daniell, R. E. (1979). An electrodynamic model of the solar wind interaction with the ionospheres of Mars and Venus. Planet. Space Sci., 27, 1111.
- Cloutier, P. A., Tascione, T. F., and Daniell, R. E. (1981). An electrodynamic model of electric currents and magnetic fields in the dayside ionosphere of Venus. Planet. Space Sci., 29, 635.
- Cloutier, P. A., Tascione, T. F., Daniell, R. E., Taylor, H. A., and Wolff, R. S. (1982). Physics of the interaction of the solar wind with the ionosphere of Venus: Flow/field models, in Venus (ed. D. M. Hunten, L. Colin, and T. M. Donahue).

- Coeffy, H. E. (1979). Solar Geophysical Data - Prompt Reports, 413, part 1, NOAA, Boulder, Colorado, pp. 39-40.
- Colin, L. (1979). Encounter with Venus: an update. Science, 205, 44.
- Colin, L. (1980). The Pioneer Venus Program. J. Geophys. Res., 85, 7575.
- Daniell, R. E. (1976). Solar Wind Induced Currents in the Atmospheres of Non-Magnetic Planets. Ph.D. Thesis, Rice University
- Daniell, R. E., and Cloutier, P. A. (1977). Distribution of ionospheric currents induced by the solar wind interactions with Venus. Planet. Space Sci., 25, 621.
- Elphic, R. C., Russell, C. T., Slavin, J. A., and Brace, L. H. (1980a). Observations of the dayside ionopause and ionosphere of Venus. J. Geophys. Res., 85, 7679.
- Elphic, R. C., Russell, C. T., Slavin, J. A., Brace, L. H., and Nagy, A. F. (1980b). The location of the dayside ionopause of Venus: Pioneer Venus Orbiter magnetometer observations. Geophys. Res. Lett., 7, 561.
- Gombosi, T. I., Cravens, T. E., Nagy, A. F., Elphic, R. C., and Russell, C. T. (1980). Solar wind absorption by Venus. J. Geophys. Res., 85, 7747.
- Hanson, W. B. (1965). Structure of the ionosphere, in Satellite Environment Handbook (ed. F. S. Johnson), Stanford, Univ. Press, Stanford California.

- Hartle, R. E., Taylor, H. A., Bauer, S. J., Brace, L. H., Russell, C. T., and Daniell, R. E. (1980). Dynamical response of the dayside ionosphere of Venus to the solar wind. J. Geophys. Res., 85, 7739.
- Hasegawa, A. (1975). Plasma Instabilities and Nonlinear Effects. Springer-Verlag, New York, p. 125.
- Haymes, R. C. (1971). Introduction to Space Science. John Wiley & Sons, New York, p. 287.
- Hundhausen, A. J. (1972). Coronal Expansion and Solar Wind. Springer-Verlag, New York, pp. 20-35.
- Hundhausen, A. J. (1972). Streams, sectors, and solar magnetism, in The New Solar Physics (ed. J. A. Eddy), Westview Press, Boulder, Colorado, pp. 59-134.
- Jackson, J. D. (1975). Classical Electrodynamics. John Wiley and Sons, New York, pp. 472-473.
- King, J. H. (1977). Interplanetary Medium Data Book. National Space Science Data Center, NASA/Goddard Space Flight Center (NSSDC/WDC - A - R & S 79-08).
- King, J. H. (1981). On the enhancement of the IMF magnitude during 1978-1979. J. Geophys. Res., 86, 4828.
- Kliore, A. J., Woo, R., Armstrong, J. W., Patel, I. R., and Croft, T. A. (1979). The polar ionosphere of Venus near the terminator from early Pioneer Venus Orbiter radio oscillations. Science, 203, 765.

- Knudsen, W. C., Spenner, K., Whitten, R. C., Sprieter, J. R., Miller, K. L., and Novak, V. (1979a). Thermal structure and major ion composition of the Venus ionosphere: first RPA results from Venus Orbiter. Science, 203, 757.
- Knudsen, W. C., Spenner, K., Whitten, R. C., Sprieter, J. R., Miller, K. L., and Novak, V. (1979b). Thermal structure and energy influx to the day - and nightside Venus ionosphere. Science, 205, 105.
- Knudsen, W. C., Spenner, K., Miller, K. L., and Novak, V. (1980). Transport of ionospheric O^+ ions across the Venus terminator and implications. J. Geophys. Res., 85, 7803.
- Knudsen, W. C., Spenner, K., and Miller, K. L. (1981). Anti-solar acceleration of ionospheric plasma across the Venus terminator. Geophys. Res. Lett., 8, 241.
- Krall, A. N. and Trevelpice, A. W. (1973). Principles of Plasma Physics. McGraw-Hill Book Co., New York, pp. 90-92.
- Luhmann, J. G., Elphic, R. C., Russell, C. T., Mihalov, J. D., and Wolfe, J. H. (1980). Observations of large scale magnetic fields in the dayside Venus ionosphere. Geophys. Res. Lett., 7, 917.
- Luhmann, J. G., Elphic, R. C., Russell, C. T., Slavin, J. A., and Mihalov, J. D. (1981a). Observations of large

- scale steady magnetic fields in the nightside Venus ionosphere and near wake. Geophys. Res. Lett., 8, 517.
- Luhmann, J. G., Elphic, R. C., Russell, C. T., and Brace, L. H. (1981b). On the role of the magnetic field in the solar wind interaction with Venus: Expectations versus observations. Adv. Space Res., 1, 123.
- Michel, F. C. (1971). Solar wind interactions with planetary atmospheres. Rev. Geophys., 19, 427.
- Mihalov, J. D., Wolfe, J. H., and Intriligator, D. S. (1980). Pioneer Venus plasma observations of the solar wind - Venus interaction. J. Geophys. Res., 85, 7613.
- Miller, K. L., Knudsen, W. C., Spenser, K., Whitten, R. C., and Novak, K. (1980). Solar zenith angle dependence of ionospheric ion and electron temperatures and density on Venus. J. Geophys. Res., 85, 7759.
- Nagy, A. F., Cravens, T. E., Chen, R. H., Taylor, H. A., Brace, L. H., and Brinton, H. C. (1979). Comparison of calculated and measured ion densities on the dayside of Venus. Science, 205, 107.
- Nagy, A. F., Cravens, T. E., Smith, S. G., Taylor, H. A., and Brinton, H. C. (1980). Model calculations of the dayside ionosphere of Venus: Ionic composition. J. Geophys. Res., 85, 7795.
- Ness, W. N. (1965). The interplanetary medium, in Introduction to Space Science (ed. W. N. Ness), Gordon and Breach Science Pub., New York.

- Niemann, H. B., Hartle, R. E., Kasprzak, W. T., Spencer, N. W., Hunten, D. M., and Carign , G. R. (1979a). Venus upper atmospheric neutral composition: Preliminary results from the Pioneer Venus Orbiter. Science, 203, 770.
- Niemann, H. B., Hartle, R. E., Hedin, A. E., Kasprzak, W. T., Spencer, N. W., Hunten, D. M., and Carignan, G. R. (1979b). Venus upper atmosphere neutral gas composition: First observations of the diurnal variations. Science, 205, 54.
- Niemann, H. B., Kasprzak, W. T., Hedin, A. E., Hunten, D. M., and Spencer, N. W. (1980). Mass spectrometric measurements of the neutral gas composition of the thermosphere and exosphere of Venus. J. Geophys. Res., 85, 7817.
- Oates, G. C. (1974). Vector analysis, in Handbook of Applied Mathematics (ed. C. E. Pearson), Van Nostrand Reinhold Co., New York, pp. 129-130.
- Ong, R. S. B., and Roderick, N. (1972). On the Kelvin-Helmholtz instability of the Earth's magnetopause. Planet. Space Sci., 20, 1.
- Russell, C. T., Elphic, R. C., and Slavin, J. A. (1979a). Initial Pioneer Venus magnetic field results: Dayside observations. Science, 203, 745.

- Russell, C. T., Elphic, R. C., and Slavin, J. A. (1979b). The solar wind interaction with Venus, in Proc. of Magnetospheric Boundary Layers Conf., ESA SP-148, 231.
- Russell, C. T., and Elphic, R. C. (1979). Observation of magnetic flux ropes in the Venus ionosphere. Nature, 279, 616.
- Russell, C. T., Snare, R. C., Means, J. D., and Elphic, R. C. (1980a). Pioneer Venus Orbiter Fluxgate Magnetometer. IEEE Trans. Geosci., GE-18, 32.
- Russell, C. T., Zhuang, H.-C., and Walker, R. J. (1981). A note on the location of the stagnation point in the magnetosheath flow. Geophys. Res. Lett., 8, 984.
- Russell, C. T., Elphic, R. C., and Slavin, K. A. (1980b). Limits on the intrinsic magnetic field of Venus. J. Geophys. Res., 85, 8319.
- Slavin, J. A., Elphic, R. C., Russell, C. T., Scarf, F. L., Wolfe, J. H., Mihalov, J. D., Intriligator, D. S., Brace, L. H., Taylor, H. A. and Daniell, R. E. (1980). The solar wind interaction with Venus: Pioneer Venus observations of bow shock location and structure. J. Geophys. Res., 85, 7625.
- Smirnov, V. N., Vaisberg, O. L., and Intriligator, D. S. (1980). An empirical model of the Venusian outer environment. 2. The shape and location of the bow shock. J. Geophys. Res., 85, 7651.

- Spenner, K., Knudsen, W. C., Miller, K. L., Novak, V., Russell, C. T., and Elphic, R. C. (1980). Observations of the Venus mantle, the boundary region between solar wind and ionosphere. J. Geophys. Res., 85, 7655.
- Spitzer, L. (1962). Physics of Fully Ionized Gases. Interscience Publishers, New York, pp. 21-30.
- Spreiter, J. R., Slummers, A. L., and Rizzi, A. W. (1970). Solar wind flow past nonmagnetic planets--Venus and Mars. Planet. Space Sci., 18, 2181.
- Spreiter, J. R., and Stahara, S. S. (1980). Solar wind flow past Venus: Theory and comparison. J. Geophys. Res., 85, 7715.
- Taylor, H. A., Brinton, H. C., Bauer, S. J., Hartle, R. E., Cloutier, P. A., Michel, F. C., Daniell, R. E., and Blackwell, B. H. (1979a). Ionosphere of Venus: First observations of the dayside ion composition near dawn and dusk. Science, 203, 752.
- Taylor, H. A., Brinton, H. C., Bauer, S. J., Hartle, R. E., Cloutier, P. A., Michel, F. C., Daniell, R. E., Donahue, T. M., and Maehl, R. C. (1979b). Ionosphere of Venus: First observations of the effects of dynamics on the dayside ion composition. Science, 203, 755.
- Taylor, H. A., Brinton, H. C., Bauer, S. J., Hartle, R. E., Cloutier, P. A., and Daniell, R. E. (1980). Global observations of the composition and dynamics of the

ionosphere of Venus: Implications for solar wind interactions. J. Geophys. Res., 85, 7765.

Taylor, H. A., Daniell, R. E., Hartle, R. E., Brinton, H. C., Bauer, S. J., and Scarf, F. L. (1981). Dynamic variations observed in thermal and superthermal ion distributions in the dayside ionosphere of Venus. Adv. Space Res., 1, 247.

Theis, R. F., Brace, L. H., and Mayr, H. G. (1980). Empirical models of the electron temperature and density in the Venus ionosphere. J. Geophys. Res., 85, 7787.

Theis, R. F., Brace, L. H., Schatten, K. H., Russell, C. T., Slaven, J. A., and Wolfe, J. A. (1981). The Venus ionosphere as an obstacle to the solar wind. Adv. Space Res., 1, 47.

Vaisberg, O. L., Intriligator, D. S., and Smirnov, V. N. (1980a). Pressure balance and pressure distribution along the dayside ionopause of Venus. Nature, 286, 235.

Vaisberg, O. L., Intriligator, D. S., and Smirnov, V. N. (1980b). An empirical model of the Venusian outer environment, 1. The shape of the dayside solar wind-atmosphere interface. J. Geophys. Res., 85, 7642.

von Zahn, U., Krankowsky, D., Mauersberger, K., Neir, A. O., and Hunten, D. M. (1979). Venus thermosphere: In

situ composition measurements, the temperature profile, and the homopause altitude. Science, 203, 768.

von Zahn, U., Fricke, K. H., Hunten, D. M., Krankowsky, D., Mauersberger, K., and Neir, A. O. (1980). The upper atmosphere of Venus during morning conditions. J. Geophys. Res., 85, 7829.

Wolfe, J., Intriligator, D. S., Mihalov, J., Collard, H., McKibbin, D., Whitten, R., and Barnes, A. (1979). Initial observations of the Pioneer Venus Orbiter solar wind plasma experiment. Science, 203, 750.

Wolff, R. S., Goldstein, B. E., and Kumar, S. (1979). A model of the variability of the Venus ionopause altitude. Geophys. Res. Lett., 6, 353.

Wolff, R. S., Goldstein, B. E., and Yeates, C. M. (1980). The onset and development of Kelvin-Helmholtz instability at the Venus ionopause. J. Geophys. Res., 85, 7697.

Zwan, B. J., and Wolf, R. A. (1976). Depletion of solar wind plasma near a planetary boundary. J. Geophys. Res., 81, 1636.

DATE
ILMEI
—8